

FULLY PRINTED FLEXIBLE AND STRETCHABLE ELECTRONICS

By

Suoming Zhang

A DISSERTATION

Submitted
to Michigan State University
in partial fulfillment of the requirements
for the degree of

Electrical Engineering – Doctor of Philosophy

2018

ABSTRACT

FULLY PRINTED FLEXIBLE AND STRETCHABLE ELECTRONICS

By

Suoming Zhang

Through this thesis proposal, the author has demonstrated series of flexible or stretchable sensors including strain gauge, pressure sensors, display arrays, thin film transistors and photodetectors fabricated by a direct printing process.

By adopting the novel serpentine configuration with conventional non-stretchable materials silver nanoparticles, the fully printed stretchable devices are successfully fabricated on elastomeric substrate with the demonstration of stretchable conductors that can maintain the electrical properties under strain and the strain gauge, which could be used to measure the strain in desired locations and also to monitor individual person's finger motion. And by investigating the intrinsic stretchable materials silver nanowires (AgNWs) with the conventional configuration, the fully printed stretchable conductors are achieved on various substrates including Si, glass, Polyimide, Polydimethylsiloxane (PDMS) and Very High Bond (VHB) tape with the illustration of the capacitive pressure sensor and stretchable electroluminescent displays. In addition, intrinsically stretchable thin-film transistors (TFTs) and integrated logic circuits are directly printed on elastomeric PDMS substrates. The printed devices utilize carbon nanotubes and a type of hybrid gate dielectric comprising PDMS and barium titanate (BaTiO_3) nanoparticles. The BaTiO_3 /PDMS composite simultaneously provides high dielectric constant, superior stretchability, low leakage, as well as good printability and compatibility with the elastomeric substrate. Both TFTs and logic circuits can be stretched beyond 50% strain along either channel length or channel width directions for thousands of cycles while showing no significant degradation in electrical performance. Finally, by applying the SWNTs as the channel layer of the thin film transistor, we successfully fabricate the fully printed flexible photodetector which exhibits good electrical

characteristics and the transistors exhibit good reliability under bending conditions owing to the ultrathin polyimide substrate as well as the superior mechanical flexibility of the gate dielectric and carbon nanotube network. Furthermore, we have demonstrated that by using two types of SWCNT samples with different optical absorption characteristics, the photoreponse exhibits unique wavelength selectivity, as manifested by the good correlation between the responsive wavelengths of the devices with the absorption peaks of the corresponding carbon nanotubes.

All the proposed materials above together with the unique direct printing process may offer an entry into more sophisticated flexible or stretchable electronic systems with monolithically integrated sensors, actuators, and displays for real life applications.

To my family and friends, for their unconditional support.

ACKNOWLEDGMENTS

Even though only my name appears in the front page of this thesis proposal, many people have been contributing and helping me along the road.

First of all, I would like to thank my advisor Dr. Chuan Wang for his support, encouragement, inspiration and invaluable mentorship throughout my PhD period. As a diligent, humble and energetic person, you have been my all-time idol. And I also want to acknowledge my research committee including Dr. Wen Li, Dr. Nelson Sepúlveda, Dr. Junghoon Yeom for their constructive guidance and valuable feedback.

Also, I have to thank my labmates and their family including Dr. Le Cai, Jinshui Miao, Yuan Wu, Dr. Qinqin Wei, Haochuan Wan, Yiheng Zhang, Zhihao Xu, Wenyue Ma, Tianhang Sun, Qifan Wang, Dr. Lei Zhang, Dr. Min Yu for all the guidance, idea sharing, discussion and ridicule (emphasis). All of these have made my Ph.D. life splendid and full of joy. Special appreciation to Dr. Le Cai and Jinshui Miao for all your great suggestions and care.

I would like to thank our collaborators including Dr. Timothy Grotjohn, Dr. Tim Hogan, Dr. Xiaobo Tan, Dr. Chunqi Qian for the guidance and also the fundings. Thank all the staff and secretary including Baokang Bi, Brian Wright, Karl Dersch, Roxanne Peacock, Laurie Rashid and Meagan Kroll for their assistance.

I would like to thank all the members in Friday's basketball group, especially Tongyu Wang, Wei Li and Zhihao Xu for all the rebounds, hand-off, screen and the fun moment we have had together.

And most importantly, I would like to specially thank my parents for believing in me all the time and also for their selfless love, spiritual and financial support. Thank my wife for her wholehearted support. One thing I want you to know is I'll try my best to love you and never let you down.

TABLE OF CONTENTS

LIST OF TABLES	viii
LIST OF FIGURES	ix
CHAPTER 1 INTRODUCTION	1
1.1 Background	1
1.1.1 Flexible and Stretchable Electronics	1
1.1.2 Scalable Fabrication by Printing	8
1.1.2.1 Flexographic Printing	9
1.1.2.2 Gravure Printing	10
1.1.2.3 Screen Printing	11
1.1.2.4 Inkjet Printing	12
1.2 Motivation and Challenges	14
1.3 Anticipated Contributions	15
1.4 Dissertation Outline	16
CHAPTER 2 FULLY PRINTED STRETCHABLE CONDUCTORS AND STRAIN GAUGES	18
2.1 Introduction	18
2.2 Fabrication Process and Measurement Setup	20
2.3 Results and Discussion	20
2.4 Potential Application	27
2.4.1 Stretchable Conductor	27
2.4.2 Strain Gauge	28
2.5 Summary	31
CHAPTER 3 PATTERNING SILVER NANOWIRES ON VARIOUS SUBSTRATES USING A DIRECT PRINTING METHOD FOR STRETCHABLE CONDUCTORS, SENSORS AND DISPLAYS	32
3.1 Introduction	32
3.2 Fabrication Process and Measurement Setup	34
3.3 Results and Discussion	36
3.4 Summary	50
CHAPTER 4 FULLY PRINTED STRETCHABLE THIN FILM TRANSISTORS AND INTEGRATED LOGIC CIRCUITS	51
4.1 Introduction	51
4.2 Fabrication Process and Measurement Setup	52
4.2.1 Materials	52
4.2.2 Ink Formulations	53

4.2.3	Device Fabrication	53
4.2.4	Characterizations	55
4.3	Results and Discussion	56
4.4	Summary	78
CHAPTER 5 FULLY PRINTED FLEXIBLE PHOTODETECTOR BASED ON		
	CARBON NANOTUBES	80
5.1	Introduction	80
5.2	Results and Discussion	82
5.3	Potential Application - Wavelength Selective Photodetector	86
5.4	Summary	89
CHAPTER 6 CONCLUSION AND FUTURE WORK		
6.1	Summary of Thesis	91
6.2	Future work	93
6.2.1	Human Motion Controlled Robotic System	93
6.2.2	Real-time Monitoring of the Blood Pressure	94
6.2.3	Stretchable System Integrated by Sensors and Displays	97
BIBLIOGRAPHY		100

LIST OF TABLES

Table 4.1	Physical properties of the solvents for PDMS	63
-----------	--	----

LIST OF FIGURES

Figure 1.1	Application of flexible electronics: Bendable, Rollable or Foldable smart-phones [12]	2
Figure 1.2	Schematic for conceptional stretchable displays	3
Figure 1.3	Mechanical buckling for wavy configuration.(a) Schematic illustration of the buckling process for building stretchable Si devices on elastic substrates. (b) SEM image of wavy Si ribbons with uniform wavelengths and amplitudes. (c) Stretching test of wavy Si p-n diode ribbons on a PDMS substrate -11% (top), 0% (middle), and 11% (bottom) [26]. (d) Optical micrograph of buckled Si Nanowires. [27] (e) AFM image of molecular scale buckled SWNTs [28].	4
Figure 1.4	(a) Top images show the schematic representation of horseshoe-shaped stretchable interconnects. Bottom photograph shows the prototype stretchable high-frequency interconnects. (b) Optical images of stretching test in electronics with serpentine bridges. From [29].	6
Figure 1.5	(a) Schematic representation of the synthesis procedure for SWNT film, SWNT elastic conductor and SWNT paste, (b) conductivity with respect to uniaxial strain for SWNT film (1), SWNT elastic conductor (2) and commercially available carbon-particle-based elastic conductor (3), (c) variation in conductance of SWNT elastic conductor under uniaxial stretching (25%, 50%, 70%, 110% and 130%) cycles. From [37]. (d) Schematic representation of hybrid Ag-MWNT composite film, (e) conductivity variation with respect to tensile strain for five different wt% of Ag flakes in hybrid Ag-MWNT composite film; inset shows the cycling test under 20% tensile strain. From [38]	7
Figure 1.6	A comparison between printing process and traditional process	8
Figure 1.7	Process flow for flexographic printing [44]	10
Figure 1.8	The schematic diagram for gravure printing [46]	11
Figure 1.9	Schematic diagram for screen printing [48]	12
Figure 1.10	Schematic diagram for inkjet printing [49]	13

Figure 2.1	Fully printed stretchable conductor and strain gauge using AgNPs. (a) Schematic diagram of the device. (b) The sample fixed onto a linear stage which is used to do the stretching test. (c) Optical microscope image of the printed device with the radius of 200 μm , 400 μm , 800 μm and 1600 μm from top to the bottom respectively (d) Optical image of the device with the radius of 200 μm before and after 10% strain stretching.	21
Figure 2.2	(a) SEM image of the AgNPs film. (b) AFM image of the AgNPs film.	22
Figure 2.3	Stretchability of the fully printed device using AgNPs. (a) The stretchability of the device with different radius including that of the straight line device. (b) The extracted gauge factor as a function of strain for the device with different radius. (c) The gauge factor as a function of devices radius under different strain of 1%, 5% and 10%. (d) The time response of the device with the radius of 1600 μm while being stretched between 0% strain and 20% strain back and forth.	23
Figure 2.4	The stability of the printed devices with the radius of (a) 1600 μm and (b) 200 μm under stretching test of 10% strain up to 1000 cycles.	25
Figure 2.5	Simulation results and optical images for fully printed AgNPs devices. (a) The left part is the simulated strain distribution for the device with the radius of 200 μm under 10% strain and the right part is the optical images of the locations with the highest strain (Location A) and the lowest strain (Location B) under different amount of strain from 0% to 15%. (b) Similarly, the left part is the strain distribution for the device with the radius of 1600 μm and the right part is the optical images for the same locations with (a) under the same strain.	26
Figure 2.6	The current of the LED when the connected stretchable conductor had been stretching between 0% strain and 20% strain.	28
Figure 2.7	Fully printed AgNPs device as a stretchable conductor. The illumination of the LED when the connected stretchable conductor was under (a) 0% strain (release status) and (b) 20% strain (stretched status).	29
Figure 2.8	Fully printed AgNPs device as a strain gauge for detecting the finger motion. (a) The relative change of resistance as a function of strain for the printed device with multiple serpentine sections and the insert figure shows how we did the finger motion detection using the printed device. (b) The resistance response at each corresponding stage of (c). Photograph of the strain gauge attached to the finger with different bend angles.	30

Figure 3.1	(a)Printer used for this work. (b)Schematic diagram illustrating the printing process.	36
Figure 3.2	Optical micrographs of AgNWs printed on Si wafer using nozzles with openings of (a)500 μm and (b)200 μm	37
Figure 3.3	Optical microscope images of the AgNW features printed on Si wafer with nozzle moving speeds of (a) 0.5 mm/s, (b) 5 mm/s and (c) 50 mm/s.	38
Figure 3.4	Micrographs of AgNW network printed on Si wafer with different contact angle of (a) $<20^\circ$, (b) $\sim 60^\circ$, (c) $>90^\circ$	38
Figure 3.5	Micrographs of AgNW networks printed on Si wafer under different temperatures: (a) room temperature, (b) 60 $^\circ\text{C}$ and (c) 100 $^\circ\text{C}$	39
Figure 3.6	Micrograph of AgNW network printed (a) in a dot-by-dot manner and (b) in a continuous printing manner.	40
Figure 3.7	Effect of surfactant concentration on the printing results on PDMS. (a) Resistance of the AgNW networks printed on PDMS (100 printing passes) as a function of surfactant concentration in the AgNW dispersion. (b) Micrographs of AgNW networks printed on PDMS (one printing pass) using inks with different amount of surfactant.	40
Figure 3.8	Printed AgNW patterns on various substrates. (a) MSU shaped AgNW patterns printed on PDMS. Scale bar: 1 cm. (b) Straight line patterns of AgNWs printed on silicon wafer, glass slide, polyimide thin film, and VHB tape. Scale bars: 2 cm.	41
Figure 3.9	Optical micrograph (top) and SEM image (bottom) of the AgNW network printed on Si wafer with a feature width of $\approx 270 \mu\text{m}$. This feature was printed with a nozzle opening of $\approx 180 \mu\text{m}$. Scale bars: 50 and 1 μm , respectively.	42

Figure 3.10 Electrical and electromechanical characterization of the printed AgNW features with different nanowire lengths. a) SEM images of the AgNW network with average nanowire length of ≈ 4.4 , ≈ 15.6 and $\approx 38.5 \mu\text{m}$ (from top to bottom). Scale bar: $5 \mu\text{m}$. b) Nanowire length distribution of the three different AgNW inks. c) Feature resistance as functions of number of printing runs for AgNWs with different nanowire lengths. The printed features are $\approx 5000 \mu\text{m}$ long and $\approx 500 \mu\text{m}$ wide. Inset: Same data presented in log scale. d) Resistance as a function of printed feature length for all three kinds of AgNW inks (feature width is $\approx 500 \mu\text{m}$ for all samples). e) Relative change in resistance as a function of tensile strain for features with average nanowire lengths of ≈ 38.5 and $\approx 4.4 \mu\text{m}$. f) Cyclic stretching test results for the feature with an average nanowire length of $\approx 38.5 \mu\text{m}$. Inset: Measurement setup. Scale bar: 1 cm. 43

Figure 3.11 Biaxially stretchable conductors based on the printed AgNWs. a) Feature resistance as functions of areal tensile strain (top) and stretching cycles (bottom) for a AgNW feature printed on a biaxially prestretched PDMS substrate. Insets: The sample at relaxed state (left) and being stretched to an areal strain of 125% (right). b) The current-voltage (I-V) curves of the LED-driving circuit using the printed biaxially stretchable AgNW conductor as interconnect with the areal strain varying from 0% to 156%. Insets: Photographs of the circuit while the interconnect is under 0 (left) and 125% (right) areal tensile strain. Scale bar: 2 cm. 45

Figure 3.12 Soft capacitive pressure sensor array using the printed AgNW features as stretchable electrodes. a) Relative change in capacitance as a function of applied pressure for an individual pixel. Inset: Structural schematic of the pressure sensor. b) Photograph of a 10×10 pressure sensor array with a line width of $\approx 600 \mu\text{m}$ and a pitch size of $\approx 1600 \mu\text{m}$. Scale bar: 1 cm. c) Photographs of placing different objects on the sensor array to demonstrate its pressure mapping capability. From left to right: a 10 g weight, M-, S-, and U-shaped objects. d) The corresponding 2D pressure contour plot determined from the measured capacitance change and the calibration curve in (a). 46

Figure 3.13	Stretchable electroluminescent (EL) displays using the printed AgNWs as electrodes. (a) Schematic of the device structure. (b) EL spectra of the device made of green phosphors under different stimulation conditions. (c,d) EL intensity of the device made of green phosphors as functions of frequency (c, measured at 1 kV) and magnitude (d, measured at 500 Hz) of the AC voltage. (e) Normalized EL intensity plotted as a function of tensile strain when measured under AC voltage with different magnitudes and a frequency of 1 kHz. Inset: Photographs of a device made of green phosphors under 0 and 20% tensile strains. Scale bars: 5 mm. (f) Normalized EL intensity versus stretching cycles measured under AC voltage with a magnitude of 1.5 kV and a frequency of 1 kHz. (g) Photographs of a 6×6 EL display array made of green phosphors (left), an MSU display pattern using orange, green, and blue phosphors for M, S, and U, respectively (middle), and the MSU-shaped display under 0 and 20% tensile strains (right). Scale bars: 1 cm.	49
Figure 4.1	Schematic diagrams illustrating the fabrication processes of printed stretchable TFTs.	55
Figure 4.2	Fully printed and intrinsically stretchable carbon nanotube thin-film transistors (TFTs) and integrated logic circuits. (a) Schematic illustrating the structure of a printed stretchable TFT. Unsorted carbon nanotubes, high-purity semiconducting single-walled carbon nanotubes (sSWCNT), and BaTiO ₃ /PDMS composite are used as the source/drain/gate electrodes, channel semiconductor, and gate dielectric, respectively. (b) Optical micrograph of a TFT printed on a PDMS substrate. (c-e) Scanning electron micrograph of the carbon nanotube network in the source/drain electrodes (c) and channel (d) and atomic force micrograph of the BaTiO ₃ /PDMS gate dielectric (e). (f) Optical photograph of a representative sample consisting of four TFTs, a resistive load inverter, and a resistive load two-input NOR gate and NAND gate, at tensile strains of 0% (top), $\sim 25\%$ (middle), and $\sim 50\%$ (bottom).	56

Figure 4.3	Fully-printed all-CNT back-gated TFT on Si/SiO ₂ substrate. a, Photograph of the unsorted carbon nanotube ink. b, Schematic of the back gated TFT printed on Si with the unsorted carbon nanotubes as source/drain electrodes. c,d, Scanning electron microscopy (SEM) images showing the carbon nanotube networks in the source/drain electrodes (c) and channel (d). Scale bars in c and d represent 200 nm and 1 μ m, respectively. e,f, Representative transfer curves of the back-gated TFTs with evaporated Ti/Au (e) and printed CNT (f) as source/drain electrodes for V_{DS} from 0 to -0.5 V in -0.1 V steps. Insets of e and f show the micrographs of the corresponding TFTs. Scale bars represent 300 μ m and 1000 μ m, respectively. g, Output curves of the TFT with printed CNT as source/drain electrodes at low drain bias. V_{GS} varies from 0 V to 40 V in 10 V step.	58
Figure 4.4	Contact angle of water with and without Triton X-100 on PDMS treated with O ₂ plasma. a, Optical images of water droplets with different concentration of Triton X-100 on PDMS (O ₂ plasma treatment: 30 W, 3 sec) before and after heating at 100 $^{\circ}$ C for 1 hour. b,c, Contact angle of water with different concentrations of Triton X-100 plotted as a function of O ₂ plasma treatment time before (b) and after (c) heating at 100 $^{\circ}$ C for 1 hour.	59
Figure 4.5	Characteristics of the printed CNT electrodes. (a) Resistance of CNT features (length \sim 6 mm, width \sim 0.5 mm) printed on PDMS as a function of the number of printing runs. The error bars are standard deviations obtained from more than five samples. (b) Relative change in resistance ($\Delta R/R_0$) as functions of tensile strain for CNT features with (blue squares) and without (red circles) PDMS encapsulation layer. (c) $\Delta R/R_0$ of a printed CNT feature (with PDMS encapsulation) when the sample is being repeatedly stretched between 0% and 60% strain.	60
Figure 4.6	Characteristics of the BaTiO ₃ /PDMS gate dielectric. (a) Relative permittivity of the composite gate dielectric as a function of the volume content of BaTiO ₃ nanoparticles measured from parallel plate capacitors fabricated on glass substrate. The error bars are standard deviations obtained from more than five samples. Inset: cross-sectional schematic of the parallel plate capacitor. (b) Capacitance measured at various frequencies for the composite gate dielectrics with BaTiO ₃ volume content of 15% (blue squares) and 26% (red circles), respectively. (c) Leakage current density of the composite gate dielectric with a thickness of around 2 μ m.	64

Figure 4.7	(a) Relative change in capacitance ($\Delta C/C_0$) as a function of tensile strain measured from a parallel plate capacitor printed on PDMS. Inset: cross-sectional schematics of the capacitor at relaxed state and stretched state. (b) $\Delta C/C_0$ at 0% (red circles) and 50% (blue squares) strains measured during repeated stretching tests for more than 2000 cycles. (c) Leakage current density of the composite gate dielectric measured at 0% (red circles) and 60% (blue squares) strains.	65
Figure 4.8	Optical micrographs of a BaTiO ₃ /PDMS feature printed on PDMS while the substrate is at relaxed state (0% strain), stretched to 40% or 100% strain, and returned to 0% strain. Scale bars in all images represent 200 μm	66
Figure 4.9	Electrical characteristics of top-gated TFTs on silicon substrate with BaTiO ₃ /PDMS as gate dielectric. a,b, Transfer characteristics of devices with 300 nm SiO ₂ (a) or printed BaTiO ₃ /PDMS (b) as gate dielectric. Insets of a and b show the cross sectional schematics of the corresponding devices. c, Representative output characteristics of a TFT with the printed BaTiO ₃ /PDMS hybrid dielectric. d, A scattering points statistics of the electrical performance of devices with BaTiO ₃ /PDMS as gate dielectric.	68
Figure 4.10	Representative electrical characteristics of the fully printed stretchable TFTs on PDMS. (a) Semilogarithmic scale plot showing the forward and backward sweep transfer characteristics ($I_{SD} - V_{GS}$) of a TFT measured at V_{DS} of -5 V (red) and -0.5 V (blue) and the gate leakage current curve ($I_{SG} - V_{GS}$) measured at V_{DS} of -0.5 V (gray dashed line). (b) I_{SD} (blue) and transconductance (red) as functions of V_{GS} plotted in linear scale for the same device in panel (a). (c) Output characteristics of the same TFT with V_{GS} varying from 30 V to -30 V. Inset shows the $I_{DS} - V_{DS}$ curves under low drain bias indicating negligible Schottky barriers at the semiconductor and S/D electrode interfaces.	69
Figure 4.11	(a, b) Optical micrographs showing two devices stretched along channel length (a) and channel width (b) directions, respectively. Scale bars represent 1 mm.	70

Figure 4.12	(a, d) Transfer characteristics at V_{DS} of -0.5 V, while the devices are stretched to various strain levels along the channel length (a) and channel width (d) directions, respectively. (b, e) Transfer characteristics at V_{DS} of -0.5 V, while the device is stretched to 50% strain for the 1st time (red), the 370th time (green), the 760th time (blue), and the 1400th time (orange) along channel length (b) and channel width (e) directions, respectively. (c, f) Field-effect mobility (left axes) and on/off current ratio (right axes) as functions of tensile strain (upper panel, in the 1st cycle) and stretching cycles (lower panel, at 50% strain) along channel length (c) and channel width (f) directions, respectively.	71
Figure 4.13	Output characteristics of a fully-printed stretchable CNT TFT at pristine state (0% strain) (a), after being stretched to 60% strain (dashed lines in panel b) and after returning to 0% strain (solid lines in panel b).	72
Figure 4.14	Electrical characteristics of a stretchable TFT when being stretched to 100% strain along the channel length direction. a, Evolution of the transfer characteristics at various tensile strain values up to 100%. b, Field-effect mobility and on/off current ratio as functions of tensile strain.	73
Figure 4.15	Extra data about the stretching tests conducted on the same devices presented in Figure 4.12 of the main paper. a,c, Transfer curves measured at V_{DS} of -0.5 V under 0% (blue) and 50% (red) strains during the 1400th stretching cycle when the device is stretched along channel length (a) and channel width (c) directions. b,d, Field-effect mobility (red circles) and on/off current ratio (blue squares) at 0% strain as a function of stretching cycle when the device is stretched along channel length (b) and channel width (d) directions.	74
Figure 4.16	Optical micrographs of a printed resistive load inverter (i), a resistive load two-input NOR gate (ii), and a two-input NAND gate (iii).	76

Figure 4.17	Fully printed stretchable integrated logic circuits on PDMS. (a) Inverter voltage transfer characteristics (VTCs) measured with a V_{DD} of 10 V, while the device is stretched to various strain levels along the channel length direction of the driving TFT. Inset shows the inverter gain as a function of tensile strain. (b) Inverter VTCs measured at a V_{DD} of 10 V while the device is at pristine state (0% strain, red) and at 0% strain after 70 (blue) and 100 (green) stretching cycles with a maximum strain of 50% along the channel length direction of the driving TFT. (c, d) Output characteristics of the NOR gate (c) and NAND gate (d) measured at a V_{DD} of 10 V while the device is at pristine state (0% strain, blue circles) and stretched to 60% strain (red squares) along the channel length direction of the driving TFTs. For both NOR gate and NAND gate, input voltages of 80 and 0 V are treated as logic 1 and 0, respectively.	77
Figure 4.18	Output characteristics of (a) a NOR gate measured during the 1870th stretching cycle and (b) a NAND gate measured during the 10th stretching cycle.	78
Figure 5.1	a. Schematic diagram of fully printed SWNTs based TFTs. b. Optical image of the transistor and SEM image of printed SWNTs on top of BTO layer.	82
Figure 5.2	a. Transfer characteristics of fully printed TFTs based on SWNTs with and without the laser illuminating. b. Output characteristics of fully printed TFTs based on SWNTs with and without the laser illuminating. c. The relative change of resistance as a function of the laser intensity under different gate bias.	83
Figure 5.3	Time response of fully printed SWNTs based TFTs a. under various gate bias when fixing the laser intensity to 5.2 W/cm^2 . b. under illuminated laser with various laser intensity when fixing the gate bias to 40 V. c. under illuminated laser with various laser intensity when fixing the gate bias to -40 V.	85
Figure 5.4	Bending tests on the fully printed SWNTs based TFTs under a. different curvature radius and b. different bending cycles.	86
Figure 5.5	Photoluminescence excitation mapping for the (9,8) nanotube sample obtained (a) before and (b) after the chirality-based enrichment process.	87

Figure 5.6	(a-d) Output characteristics (I_{DS} - V_{DS}) of a (9,8) nanotube thin-film transistor measured before and after laser illumination with (a) $\lambda = 520$ nm, (b) $\lambda = 650$ nm, (c) $\lambda = 807$ nm, and (d) $\lambda = 980$ nm. (e-h) Output characteristics of a 99% semiconducting nanotube thin-film transistor measured before and after laser illumination with (e) $\lambda = 520$ nm, (f) $\lambda = 650$ nm, (g) $\lambda = 807$ nm, and (h) $\lambda = 980$ nm.	88
Figure 5.7	Wavelength-selectivity of the bolometric-effect-based photodetectors with different types of carbon nanotubes. (a) UV-Vis-NIR absorption spectra of two different types of SWCNTs, including single chirality (9,8) SWCNTs (orange) and 99% semiconductor-enriched SWCNTs from NanoIntegris, Inc. (red). (b) Photoresponse of devices made with the above two kinds of SWCNTs measured under different laser wavelengths of 520, 650, 807, and 980 nm. The histogram in the upper half of the graph corresponds to a $V_G = 5$ V and bottom half corresponds to a $V_G = -5$ V. Same as panel 4a, the orange columns and red columns correspond to (9,8) SWCNT sample and 99% semiconducting SWCNT sample, respectively.	89
Figure 6.1	Reprint from ref [201], (a) Plot of resistance response as a function of bending degree for the flexion sensors. (b) Schematic diagram of the remote controlling configuration. (c-g) The whole process of the remote controlling performance of four flexion sensors sewed on a textile glove. Relaxed state (c) \rightarrow clamping object (d) \rightarrow lifting object up (e) \rightarrow putting object down (f) \rightarrow releasing object (g)	94
Figure 6.2	ref [202], (a) schematic of transmission mode PPG, (b) schematic of reflection mode PPG, (c) a representative PPG waveform	95
Figure 6.3	ref [206], (a) Placement of a modified 2.5×2.5 mm ² round sensor shown in inset on the radial artery of a human subject. (b) Measured pulse pressure waveform of a human subject with a heart rate of 82 b.p.m. over 12s period with a time resolution of 90 ms.	96

Figure 6.4	<p>Reprint from ref [208], (a)Schematic layout of a single pixel, consisting of a nanotube TFT, an OLED and a pressure sensor (PSR) integrated vertically on a polyimide substrate. (b)Schematic diagram of an array of pixels (16×16) functioning as an interactive e-skin, capable of spatially mapping and visually displaying an applied pressure profile. (c)Photo of a single-colour (green) AMOLED being fully turned on and bent. Voltages of -5 and 10 V are applied to all of the scan and data lines, respectively. The pixel yield, as defined by the percentage of OLEDs in the matrix that emit light, is higher than 97%. (d)Photograph of a full-colour (red, green, blue) AMOLED display with all pixels being turned on. (e)Photo of the same full-colour display shown in d being bent. (f)Circuit schematic of the e-skin matrix. (g)Photograph of a fabricated device, showing that light is locally emitted where the surface is touched. Only the pixels being pressed are turned on. (h)PDMS slabs with C, A, and L shapes are prepared and used to apply pressure onto the sensor array. (i)Green, blue and red colour interactive e-skins are used to spatially map and display the pressure applied with C- (left), A- (centre) and L- (right) shaped PDMS slabs, respectively</p>	98
Figure 6.5	<p>Schematic for a conceptional stretchable electronics system.</p>	99

CHAPTER 1

INTRODUCTION

In the past half century, the electronic components are bulky and rigid since they are fabricated on rigid substrates such as glass or silicon. However, with the rapid development of modern society, the rigid products cannot meet the demand in some scenarios, especially when dealing with the irregular surface where the flexibility and stretchability are needed. Imagine a robot with a skin-like sensor film mounted on the joint part, the sensor film needs to be extremely stretchable to accommodate the twisting or bending motion of the joint [1]. Thanks to the recent progress in research of flexible and stretchable platform like polyimide or Polydimethylsiloxane (PDMS) as well as the active materials including Carbon Nanotubes, Silver Nanowires, the flexible/stretchable electronics become more of a possibility.

1.1 Background

1.1.1 Flexible and Stretchable Electronics

Flexible electronics, also known as flex circuits, is a technology for assembling electronic circuits by mounting electronic devices on flexible plastic substrates, such as polyimide, PET or polyester film [2]. The advancement of flexible electronics has spanned the past forty years ranging from the development of flexible solar cell arrays [3] made from very thin single-crystal silicon to flexible organic light-emitting diode displays on plastic substrates [4]. Compared with the conventional electronics based on rigid substrates, flexible electronics are typically more rugged, lighter, portable, and less expensive to manufacture. Demonstrations of flexible electronics promise the availability of low-cost and lightweight electronics in the near future. The recent rapid development of this field has been spurred by the continuing evolution of large-area electronics with applications in flat-panel displays [5, 6, 7], medical

image sensors [8, 9], and electronic paper [10, 11]. Figure 1.1 shows the applications of flexible electronics in the smartphone with bendable, rollable and foldable properties.



Figure 1.1 Application of flexible electronics: Bendable, Rollable or Foldable smartphones [12]

Although exhibiting the extraordinary advantages in low-cost and large area applications, flexible electronics have inevitably indicated their limitation in certain circumstances where the ability of overcoming certain amount of strain is needed. For instance, wearable electronics [13, 14, 15, 16], which could be mounted on cloth or people's skin, require the active devices' ability to overcome the strain caused by the movement of people's body. Here comes stretchable electronics (also known as elastic electronics), which is a technology for building electronic circuits by depositing stretchable electronic devices and circuits onto stretchable substrates or embedding them completely in a stretchable material such as silicones or PDMS. The compatibility of stretchable electronics to the strain ensures its robust performance when dealing with surface with nonzero Gaussian curvature like a sphere

or an irregular surface like the elbow. There are many potential applications for stretchable electronics such as bio-integrated devices for monitoring of human skin [17, 18], organs [19], disease or health disorders [20], prosthetic skin [21, 22], stretchable display or memory [23], conformal and stretchable sensors [24, 25, 26] for health monitoring of structures of large deflection and curvilinear surfaces such as aircraft and space satellite wings, as well as bioinspired digital cameras. Figure 1.2 shows a schematic of a concept stretchable display.

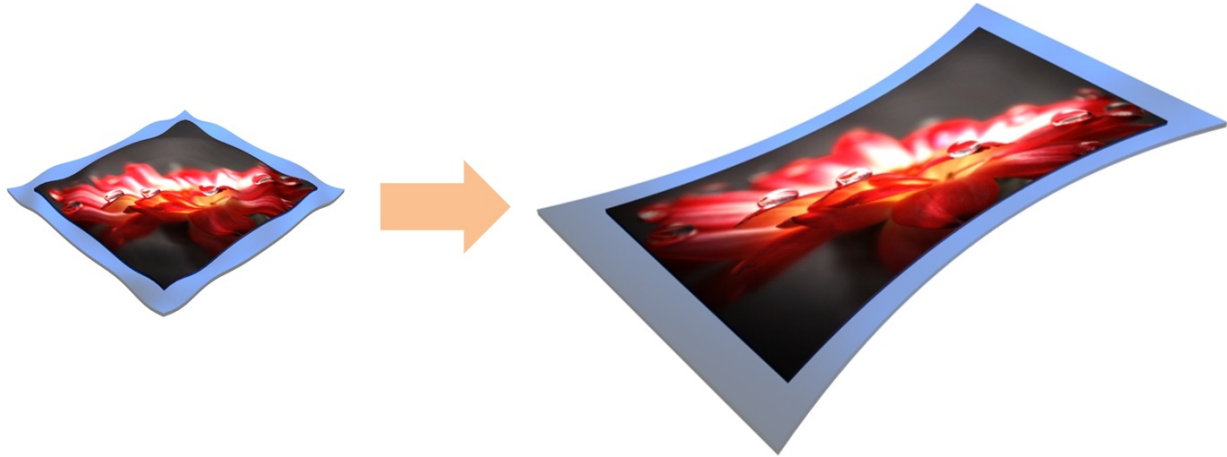


Figure 1.2 Schematic for conceptual stretchable displays

There are typically two strategies to fulfill stretchable electronics. The first one is wavy structural configuration methods that configure conventional non-stretchable materials into wavy shapes, which can accommodate large strains without fracturing the active materials. One example of this approach relies on the buckling phenomena in systems comprised of a thin rigid layer on an elastomeric substrate. When a stiff thin film attached to a polymer substrate is subjected to the compressive stress, the film would relieve the surface strain by forming mechanical buckling. Thus external stretching strain can be accommodated by relaxing the compressive prestrain, thereby improving the stretchability remarkably in active devices and passive interconnects. As shown in Figure 1.3a [27], conventional photolithography fabricated Si ribbons are attached to the prestretched PDMS substrate and then the ribbons together with PDMS are peeled off from the wafer and relaxed to form the highly periodic buckling structure (Figure 1.3b). And Figure 1.3c illustrates the silicon diode being

stretched and compressed in the range of 11% [28]. The buckling method is compatible with other nanomaterials as well, as seen in buckled Silicon nanowires [29] (Figure 1.3d) and buckled Carbon Nanotubes [30] (Figure 1.3e).

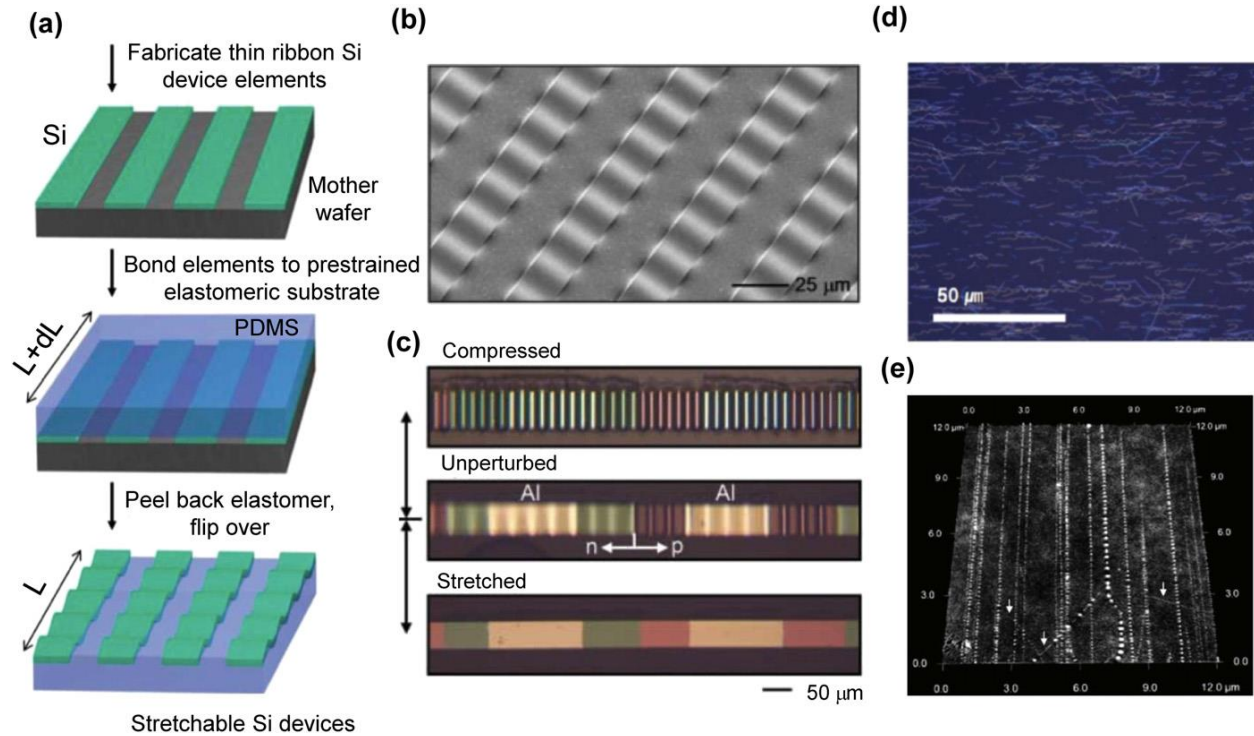


Figure 1.3 Mechanical buckling for wavy configuration. (a) Schematic illustration of the buckling process for building stretchable Si devices on elastic substrates. (b) SEM image of wavy Si ribbons with uniform wavelengths and amplitudes. (c) Stretching test of wavy Si p-n diode ribbons on a PDMS substrate -11% (top), 0% (middle), and 11% (bottom) [26]. (d) Optical micrograph of buckled Si Nanowires. [27] (e) AFM image of molecular scale buckled SWNTs [28].

Another example of this wavy structural configuration method is patterning the active materials into serpentine or horseshoe shaped structure. Thus, the applied strain would be taken by part of the pattern (mainly by the peak and valley of the sinusoidal wave according to the simulation results) rather than by the whole pattern, which is the case of patterning the materials by straight lines.

As an example, metal interconnects are designed into horseshoe configuration to tune the stretchability by changing three parameters: the diameter of the circle (D), the width

of the pattern (W) and the angle between the end of the shape and the horizontal line (H). Consequently, a high elongation was achieved with a high electrical resistance at H_{45} while a low elongation with a low electrical resistance at H_0 [31]. The high frequency stretchable interconnects are shown in the bottom figure of Figure 1.4a [32]. The serpentine structure could also be applied in the conduction lines connecting the rigid device island. As seen in Figure 1.4b, an array of CMOS inverters with the mesh of serpentine bridges was integrated on an elastomeric substrate. When the devices were stretched along the x or y direction, the serpentine bridges effectively compensated the applied strain by changing the geometry of serpentine shape to protect the active devices. As a result, a maximum stretchability up to $\sim 140\%$ is successfully demonstrated without significant degradation of performance of the CMOS array.

Instead of investigating the wavy structure using conventional non-stretchable materials, another approach to realize the stretchable electronics is to explore the intrinsic stretchable materials, which could be either the materials with large aspect ratios such as carbon nanotubes, carbon grease, carbon fibers and metal nanowires or the composite materials consist of conductive materials and stretchable materials such as SWNTs/AgNPs composite [33, 34], SWNTs/PDMS composite [35, 36], AuNPs/PDMS [37, 38], or AgNWs/PDMS composite [39].

For instance, Sekitani et al [40] developed the SWNT/polymer composite films with a uniaxial stretchability up to 70%, as indicated in Figure 1.5a. The SWNTs are uniformly dispersed into vinylidene fluoridehexafluoropropylene copolymer matrix with the help of an ionic liquid 1-butyl-3-methylimidazolium bis(trifluoromethanesulfonyl)imide, acting as stable chemical dopant. And then the SWNT composite film is coated with dimethyl-siloxanebased rubber, which exhibited a conductivity of 57 siemens per centimeter and a stretchability of 134%. Figure 1.5b shows the conductivity variation as a function of tensile strain for (1) a SWNT film, (2) the SWNT elastic conductor and (3) a commercially available conducting rubber. The SWNT film achieves high conductivity of ~ 57 S/cm up to 38% strain, but

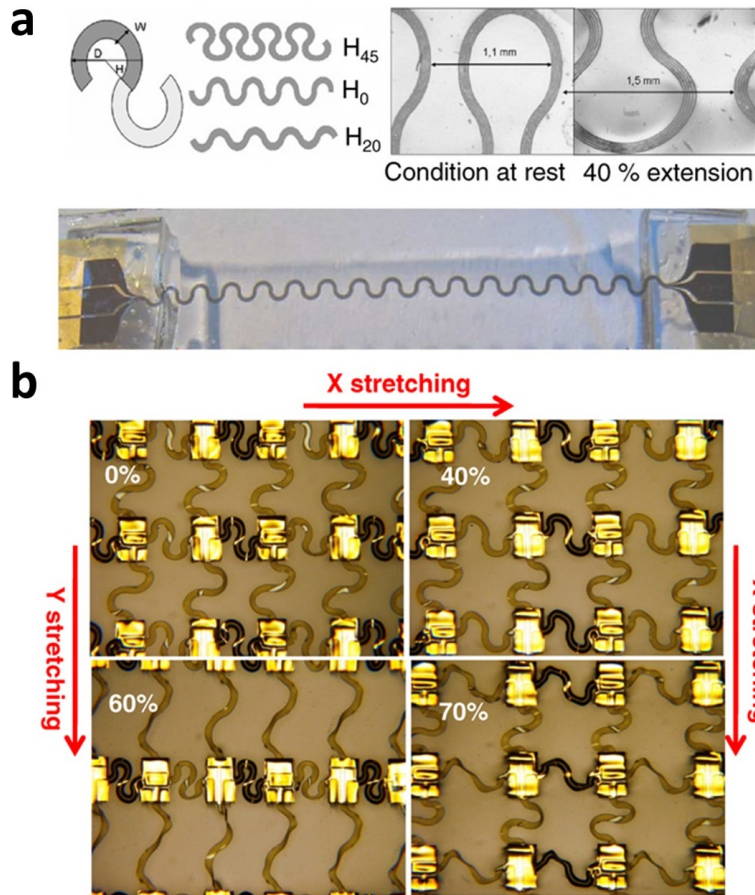


Figure 1.4 (a) Top images show the schematic representation of horseshoe-shaped stretchable interconnects. Bottom photograph shows the prototype stretchable high-frequency interconnects. (b) Optical images of stretching test in electronics with serpentine bridges. From [29].

dramatically drops afterwards. By contrast, the conductivity of the SWNT elastic conductor, even though slightly reduced from the original high conductivity of 57 S/cm, exhibits a large stretchability of 138% with a conductivity of 6 S/cm, which is still much larger than that of the commercially available conducting rubber. However, the conductivity of SWNT elastic conductors demonstrates the significant degradation with the increase of the strain as well as stretching cycles, as shown in Figure 1.5c.

Also, Chun et al [41] have reported another kind of stretchable composite materials by combining micrometer-sized silver flakes and multiwalled carbon nanotubes (MWNTs) and An Ag-MWNT composite film was formed by the conjugation of Ag nanoparticles and

concentration of Ag flake, the stretchability of the film could be as high as $\sim 35\%$. Although the conductivity reduces with the increase of the applied strain, a high conductivity of 706 S/cm is achieved at a strain of 30% for an Ag flake concentration of 8.60 wt%, which is really good performance.

Even though many efforts including investigating new approach and exploring new materials have been made in order to realize stretchable electronics, the adopted fabrication process in most work is still the conventional cleanroom process such as photolithography, metal evaporation and etching, which either requires high vacuum or is not suitable for large area applications. On the contrary, printing technology, which is compatible for large area applications and could be conducted in ambient environment, is considered as the good candidate for the fabrication process of next generation electronics.

1.1.2 Scalable Fabrication by Printing

Printed Process

Low cost

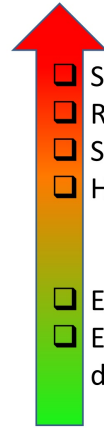


- Large areas
- Flexible/stretchable substrate
- Simple process
- Extremely low cost
- Long switching time
- Low integration density

Low end

Traditional Process

High cost



- Small areas
- Rigid substrate
- Sophisticated process
- High cost
- Extremely short switching time
- Extremely high integration density

High end

Figure 1.6 A comparison between printing process and traditional process

Creating electronic components on various substrates using the solution based materials

by printing process, the printing electronics have attracted increasing interest in the past decade. Compared with traditional cleanroom based process, printing process has many advantages including low cost, light weight, simple fabrication, suitable for large area application and compatible with flexible/stretchable substrate, the comparison for printing process and traditional process is summarized in Figure 1.6.

Printing technologies, such as flexography printing, screen printing, gravure printing and inkjet printing, could be clarified into two approaches: sheet-based approach and roll-to-roll-based approach [42]. Among them, sheet-based screen printing and inkjet printing are suitable for low-volume, high-precision work [43], while gravure printing and flexographic printing, which are considered as roll-to-roll-based approach due to the fact that the process is generally operated on the substrate from a large roll of material, are more adaptive for high-volume production, like solar cell [43]. The type of the substrate, ink viscosity, required thickness of the layer and the resolution play an important role when selecting of the applied printing methods for fabrication of electronic devices.

1.1.2.1 Flexographic Printing

Flexographic printing is a form of printing process which utilizes a flexible relief plate. The technique was firstly applied in 1890 by Bibby, Baron and Sons in Liverpool England and used extensively in food packaging in the US from early 20th century. The equipment of this printing technique is consisting of a series of four rollers: Metering Roller, Anilox Roller, Plate Cylinder and Impression Cylinder. The Metering Roller transfers the ink from an ink tray to Anilox Roller, which processes the ink onto the Plate Cylinder with a uniform thickness. The whole substrate is then moved between the Plate Cylinder and Impression Cylinder and a pressure would be applied from Impression Cylinder to the Plate Cylinder to transfer the image onto the substrate. An additional overhead tunnel dryer would feed through the substrate to remove the remaining solvent or water, resulting in a finished product [45]. Figure 1.7 shows the Flexographic printing process.

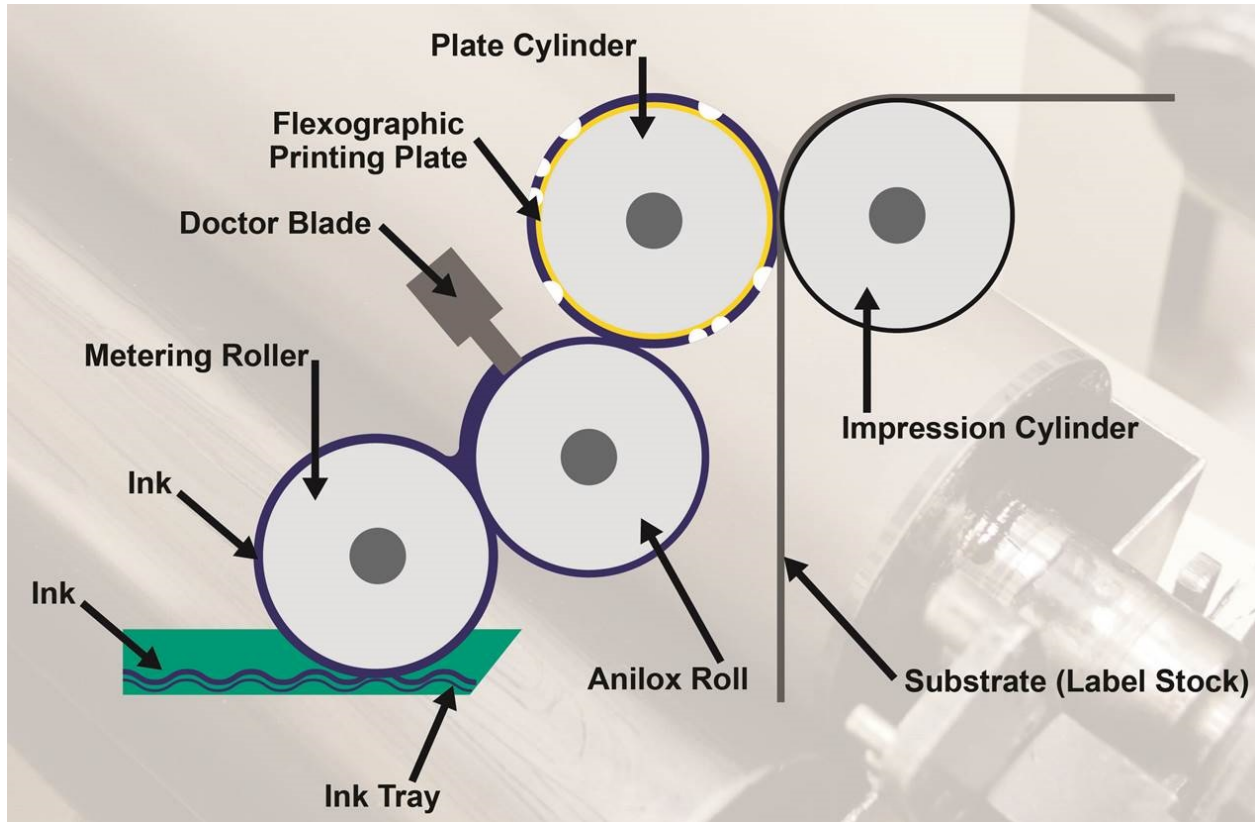


Figure 1.7 Process flow for flexographic printing [44]

1.1.2.2 Gravure Printing

Utilizing the engraved cylinders as the image carriers, the Gravure printing is an old printing technique, which was developed around the same time as Gutenberg was developing relief-based printing in mid-fifteenth century. Before printing, the desired image that is consist of honey comb shaped cell or wells is etched into the surface of gravure cylinder. And while printing, the cylinder rotates in an ink tray to collect the ink to the cell and the doctor blade on the side is designed to scrape the excess ink from the non-image area. And then the printing substrate is passed between the gravure cylinder and a rubber-coated impression roller, resulting in an ink transferring helped by both the capillary action and the pressing force applied by the engraved cells of the cylinder. Most of the performed gravure printing nowadays is web-fed rotogravure printing [47]. The schematic diagram for gravure printing is illustrated in Figure 1.8.

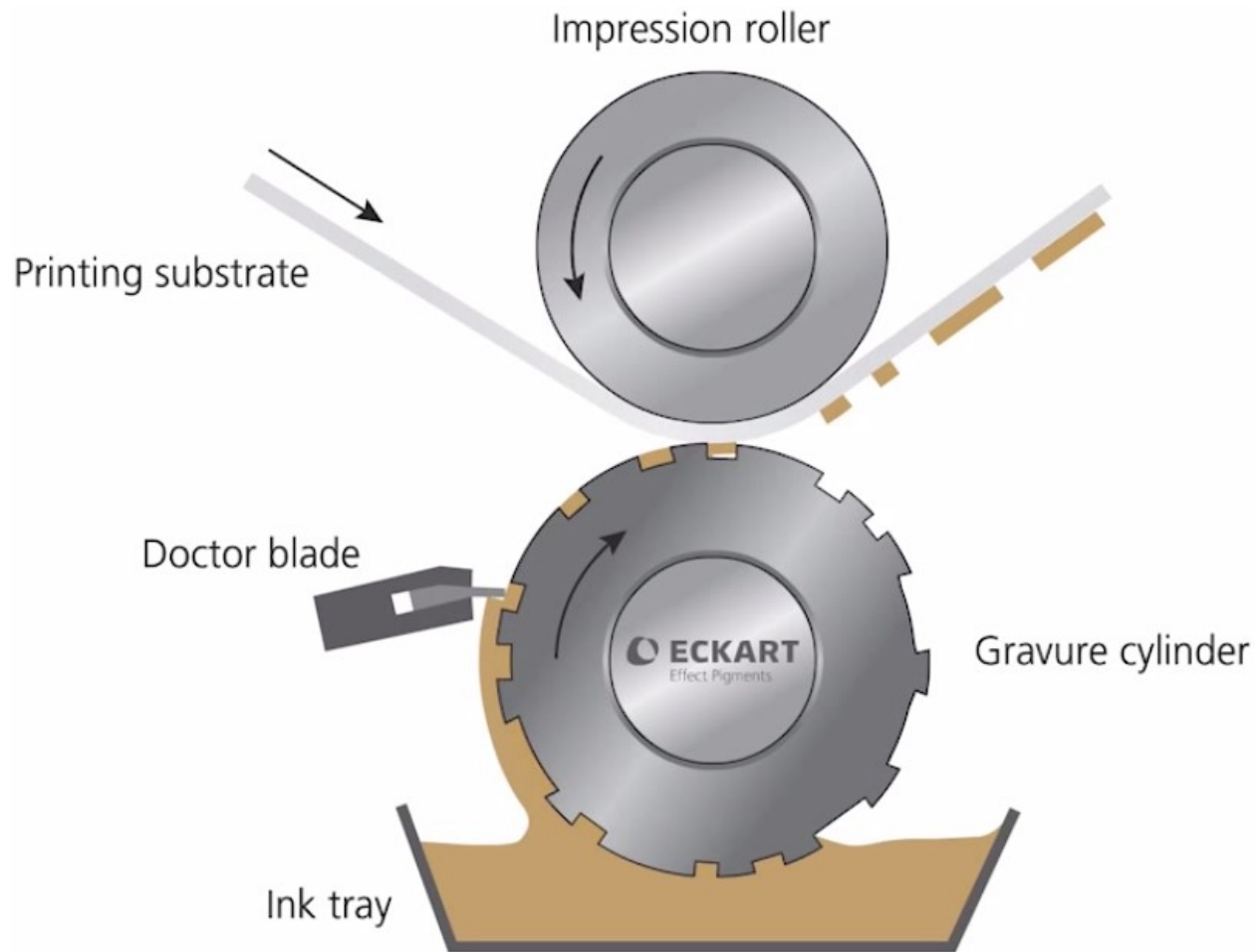


Figure 1.8 The schematic diagram for gravure printing [46]

1.1.2.3 Screen Printing

Derived from the older practice of stencil printing like the pochoir method of stenciling, screen printing is a form of printing in which a thick paste ink is driven through a stencil mask attached to the screen, transferring ink to the areas not covered by the mask on the substrate. This technique was also called silk screen printing initially because silk was adopted as the mask to print through. By using screen printing, firstly, a photo-sensitive layer is applied to a polyester mesh and then exposed to the light through the positive film of the image to be printed to harden the non-image area. This process enables the unhardened area to be washed away, leaving behind a negative image on the mesh through which the ink can flow. And then the desired image could be produced onto the substrate by a blade

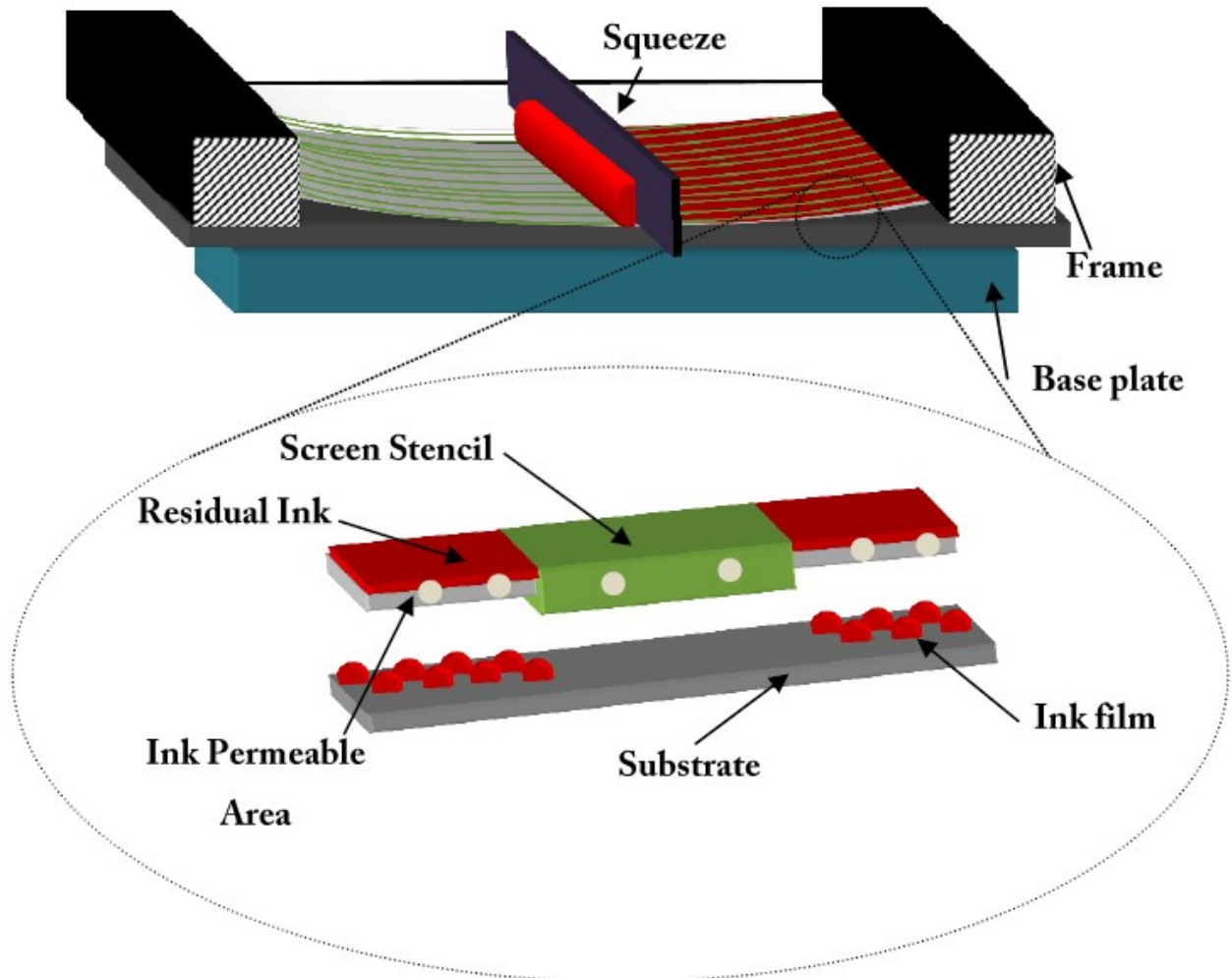


Figure 1.9 Schematic diagram for screen printing [48]

called squeegee through the prepared mesh, following by putting the whole substrate through a drying station that contains UV lamps to dry the ink. The schematic diagram for screen printing is shown in Figure 1.9.

1.1.2.4 Inkjet Printing

Other than Flexographic printing, screening printing and gravure printing, the inkjet printing is a non-impact printing method that the nozzle does not touch the substrate when printing and the image is typically formed digitally without any mask needed. And there are two main technologies in use for inkjet printing: continuous (CIJ) and Drop-on-demand (DOD)

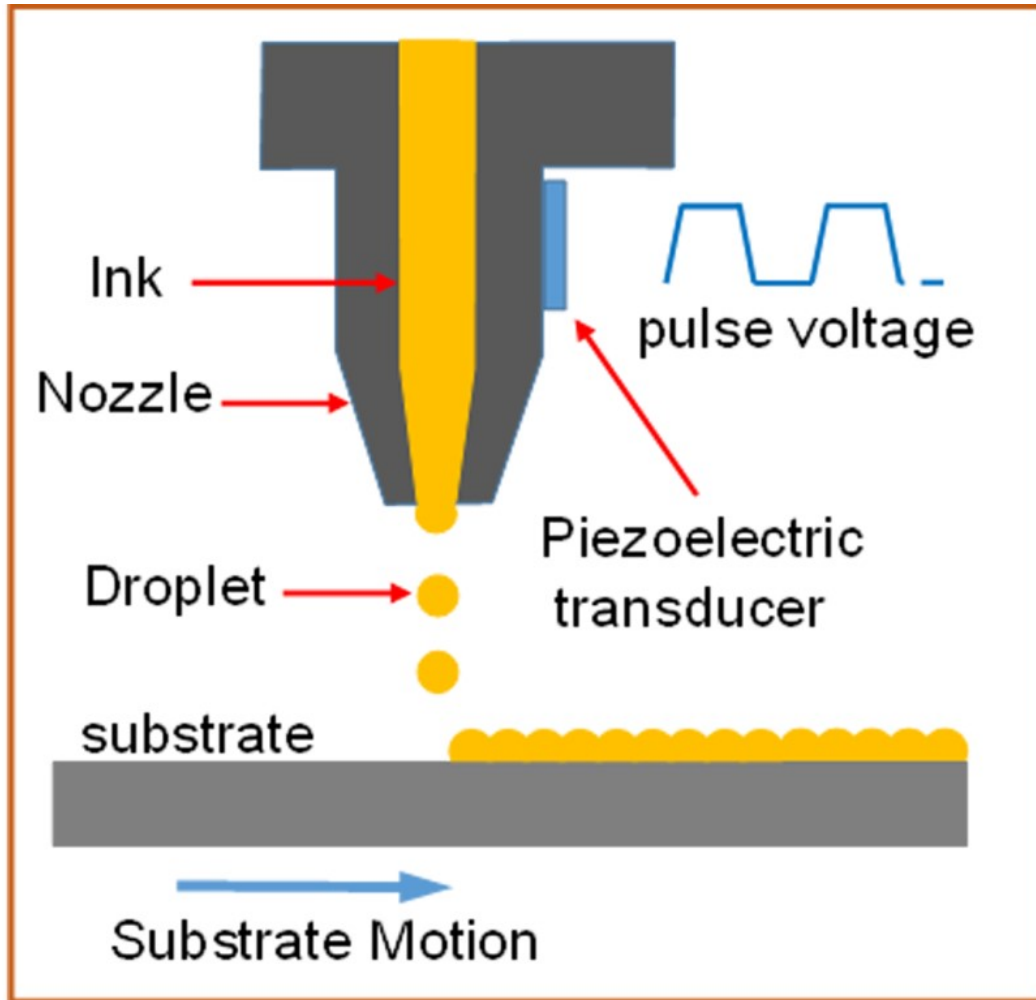


Figure 1.10 Schematic diagram for inkjet printing [49]

[50]. In CIJ technology, a high-pressure pump drives liquid ink from a reservoir through the microscopic nozzle, creating a continuous stream of ink droplets and the formed ink droplets are subjected to an electrostatic field created by a charging electrode as they form, resulting in a well-controlled electrostatic charge on each droplets and thus the printing speed and the quality could be adjusted by controlling the flow of the droplets.

And for DOD technology, it could be divided into thermal DOD and piezoelectric DOD. In the thermal inkjet process, the print cartridges consist of a series of small chambers, each containing a heater, all of which are fabricated by photolithography process. To spray a droplet from each chamber, a pulse of current is applied to the heating element, resulting

in a significant rise in temperature, thus causing the vaporization of the ink and forming a bubble, which increases the pressure in the chamber, pushing the droplet of ink out of the chamber onto the substrate. And for piezoelectric DOD, it uses a piezoelectric material in the chamber behind each nozzle instead of a heating element. When voltage is applied, the pressure pulse in the ink is generated due to the shape change of the piezoelectric, forcing the droplets to disperse. An example of the inkjet schematic diagram is illustrated in Figure 1.10.

1.2 Motivation and Challenges

Nowadays, nearly all established electronics are utilizing the single crystal inorganic materials, such as gallium arsenide and silicon, which is planar and rigid. By contrast, many applications in the present are required to perform in the platform which is soft and curvilinear, such as human body and smart systems. This mismatch impedes the development of the electronics capable of conformal, close integration with systems like human body, for the applications from the detection of electrophysiological signals to the build of human-machine interfaces [51], which also gives us the inspiration of developing electronics based on flexible or even stretchable platform. So far, many efforts have been made to conduct the applications of stretchable electronics, including displays [52], sensors [8, 25, 26, 39], and wearable electronics [13, 14, 15, 16, 53]. And among them, wearable biocompatible electronics, which could be directly attached to the skin or even the organ of human beings, have attracted more and more attentions recently. These wearable electronic devices, whose applications to monitor the parameters including electrocardiogram, body motion, blood pressure, body temperature, have demonstrated the ability to detect the vital signs and display the health conditions of an individual person.

However, one of the challenges faced by those wearable electronic devices is attaching to human body conformally in order to make the measurement accurate and also keep the

patient comfortable. One of the key factors which could improve the conformally attaching issue is the substrate used for those wearable electronics. Researches have investigated several stretchable substrates, such as Polydimethylsiloxane (PDMS) [28, 40, 54], Polyurethaneacrylate (PUA) [55, 56], Polyurethane (PU) [57] and Ecoflex [53, 58]. Most of them are polymer based stretchable materials, which is elastic compared with the conventional Si substrate and the flexible substrate like polyimide. Another solution to enhance the conformally attaching experience is to develop the intrinsic stretchable materials, which could increase the stretchability of the devices in order to maintain their functions along body's moving. In this work, such intrinsic stretchable materials including Silver Nanowires and Carbon Nanotubes would be demonstrated.

Another confronted challenge for the wearable electronics is their cost. At present, nearly all wearable electronics are fabricated by the conventional cleanroom based manufacturing technologies, which typically require multiple sophisticate equipment and have high operating temperature and high vacuum involved, thus increasing the overall expense. And also the devices fabricated by the traditional method are typically rigid and are not comfortable to be attached to human body for long durations. On the contrary, printing techniques could deliver high cost efficiency as well as comparable performance mainly because the active pattern are selectively printed onto the substrate, which terminate the adoption of mask as well as etching process, thus speeding up the fabrication process and reducing the cost. Also, printing techniques are compatible with low temperature and ambient environment, which would further decrease the overall cost, resulting in a cheaper end-product. The ink-jet printing technique would be adopted in this work.

1.3 Anticipated Contributions

In this work, the flexible and stretchable sensors are successfully demonstrated by a direct-writing printing method. Specifically, the flexible photodetectors based on SWNTs is achieved

by the fully printing process and its wavelength selectivity is also illustrated by investigating the bolometric effect. The fully printed stretchable conductors are presented by two different approaches and are demonstrated as strain gauge and pressure sensor & stretchable display in terms of the applications, respectively. And by utilizing carbon nanotubes and a new type of hybrid gate dielectric comprising PDMS and barium titanate (BaTiO_3) nanoparticles, the first intrinsically stretchable thin-film transistors (TFTs) and integrated logic circuits directly printed on elastomeric polydimethylsiloxane (PDMS) substrates have been reported. Both TFTs and logic circuits can be stretched beyond 50% strain along either channel length or channel width directions for thousands of cycles while showing no significant degradation in electrical performance. In a word, the proposed new materials as well as printing techniques in this work may offer a new entry into more sophisticated stretchable electronic systems with monolithically integrated sensors, actuators, and displays, fabricated by scalable and low-cost methods for real life applications.

1.4 Dissertation Outline

The remaining chapters are organized as follows: Chapter 2 demonstrates the fully printed stretchable conductors realized by the wavy structure configuration method with illustrating an application of strain gauge. Chapter 3 presents the fully printed stretchable conductors realized by another strategy — applying the intrinsic stretchable materials. And applications of pressure sensors and stretchable display are demonstrated afterwards. Chapter 4 demonstrates the first reported fully printed stretchable thin film transistors, which can be stretched beyond 50% strain along either channel length or channel width directions for thousands of cycles while showing no significant degradation in electrical performance. Chapter 5 shows the fully printed flexible photodetectors based on SWNTs by investigating the bolometric effect of the SWNTs based Thin Film Transistors. In addition, the wavelength selectivity of the photodetectors is presented by applying different types of the SWNTs in the TFTs.

Chapter 6 concludes the whole work and gives an outlook of the future work.

CHAPTER 2

FULLY PRINTED STRETCHABLE CONDUCTORS AND STRAIN GAUGES

By investigating the geometry design, this chapter exploits the strategy that making the fully printed device fabricated by the non-stretchable material Silver Nanoparticles (AgNPs) stretchable, following by the demonstration of two applications — stretchable conductor and strain gauge. We had printed the AgNPs pattern onto the elastomer substrate and showed the stretchability of the device could be tuned by changing the radius of the serpentine structure. The device with smaller radius was more sensitive to the strain, resulting a high gauge factor of 10^6 , demonstrated as a strain gauge to detect the finger motion of human beings, while the device with larger radius was more stretchable (more than 25%), used as a stretchable conductor for driving the LED. The printed strategy and demonstrated application would have broad prospects in stretchable electronics.

2.1 Introduction

People have been investigating flexible electronics for many years due to its flexibility, light weigh, low cost and suitability for large area applications compared with the conventional Si based electronics [59, 60]. However, its narrow limitation is displayed when dealing with arbitrarily shaped surface or other place where the stretchability is needed. Stretchable electronics, well known due to its promising applications on biological sensors [61, 62, 63, 64, 65, 66, 67], actuators [68], stretchable displays [23, 54], energy storage devices [69, 70] and wearable electronics [71], would be a good candidate for next generation electronics. There are typically two mainly strategies to make devices stretchable: developing the intrinsically stretchable materials or working with the structure design from the established materials. The former option is attractive due to its higher

stretchability compared with the latter one. People had reported the investigated stretchable material such as carbon based materials like the carbon grease [72], carbon nanotubes [54, 67, 73] or carbon fibers [65, 74], polymer based materials like the polypyrrole (PPy) and poly(3,4-ethylenedioxythiophene):poly(styrenesulfonate) (PEDOT:PSS) [75, 76, 77], PEDOT/PU composite [78], or composite materials like SWNTs/AgNPs composite [79], SWNTs/PDMS composite [40, 80, 81, 82], AgNPs/PDMS [83], or AgNWs/PDMS [84, 85, 86, 87]. The stretchability reported in most of the work mentioned above is more than 50% without significant change for the performance.

However, due to the instability and low conductivity for the device fabricated using the former strategy, some people still prefer to adopt the latter strategy to realize the stretchability, which the functional part is exposed under very little amount of strain. By using the conventional materials like Si [88], Mg [51], AgNPs [89] etc, people had developed the honeycomb structure [90], buckling wavy structure [28, 91, 92], or the serpentine structure [51, 88, 93, 94] to make the stretchable interconnects or devices, such as conductors, transistors, photodetectors or integrated circuits. Among those conventional materials, AgNPs is considered as a good candidate in terms of the materials for stretchable electronics owing to its high conductivity and good stability.

The fabrication process also play an important role by effecting the cost of the devices besides the materials themselves [95]. And the conventional vacuum based deposition and photolithography patterning process not only require high vacuum but also waste most of the materials, thus, increasing the cost of the products. Instead, without involving the high vacuum and masks for different layers, the printing process is considered as the candidate for next generation flexible or stretchable electronics due to its environmental friendly, large area fabrication compatibly property [96, 97]. Herein, we had demonstrated the fully printed serpentine pattern fabricated by the AgNPs ink and showed the stretchability of the devices could be tuned by varying their radius, following by demonstrating two applications: the stretchable conductor to drive the LED when stretched to 20% and the strain gauge whose

gauge factor is as high as 10^6 to monitor the finger motion of human beings.

2.2 Fabrication Process and Measurement Setup

Preparation for the substrate: The PUA substrate was made by the mixture of Siliconized urethane acrylate oligomer (CN990, Sartomer), ethoxylated bisphenol A dimethacrylate (SR540, Sartomer) and 2,2-Dimethoxy-2- phenylacetophenone (photoinitiator, Sigma-Aldrich) with the ratio of 10:1:0.01, following by UV light curing for 10 min. The CN990 was chosen in order to improve the stretchability of the substrate, the SR540 was chosen to adjust the stiffness of the substrate and the photoinitiator serves as catalyzer.

Device fabrication: The silver nanoink (PG-007AA from Paru Corporation, South Korea) was printed onto PUA substrate (pre-treated by the oxygen plasma, 60W for 10s) using a GIX Microplotter (Sonoplot Inc.) with the layout pre-designed by the software, and then the whole device was put on top of a hotplate to be annealed for 1 hour under 120 °C For strain gauge application, the liquid metal (LMP-2, ROTOMETALS) and copper wire was put on the two ends of the devices serving as the connection for measurement, following by pouring another layer of PUA solution and then cured by the UV light to form the encapsulation.

Device Characterization: Microscopic morphology of AgNPs film were captured by a Hitachi S-4700II field emission scanning electron microscope (for SEM) and Dimension 3100 SPM (for AFM). The stretching tests were done by a syringe pump and a linear stage. The electrical characteristics were measured using an Agilent B1500A semiconductor parameter analyzer.

2.3 Results and Discussion

The schematic diagram of the printed device is presented in Figure 2.1a. Basically, loaded into the ink dispenser, the silver nanoink (PG-007AA from Paru Corporation, South Korea) was printed onto a polyurethane acrylate (PUA) substrate using a GIX Microplotter (Sono-

plot Inc.). To make the device stretchable, the serpentine structure was pre-designed using the SonoDraw (Sonoplot Inc.). And then the Ag pattern together with the PUA substrate would be placed on a hotplate under 120 °C for 1 hour in order to improve their conductivity.

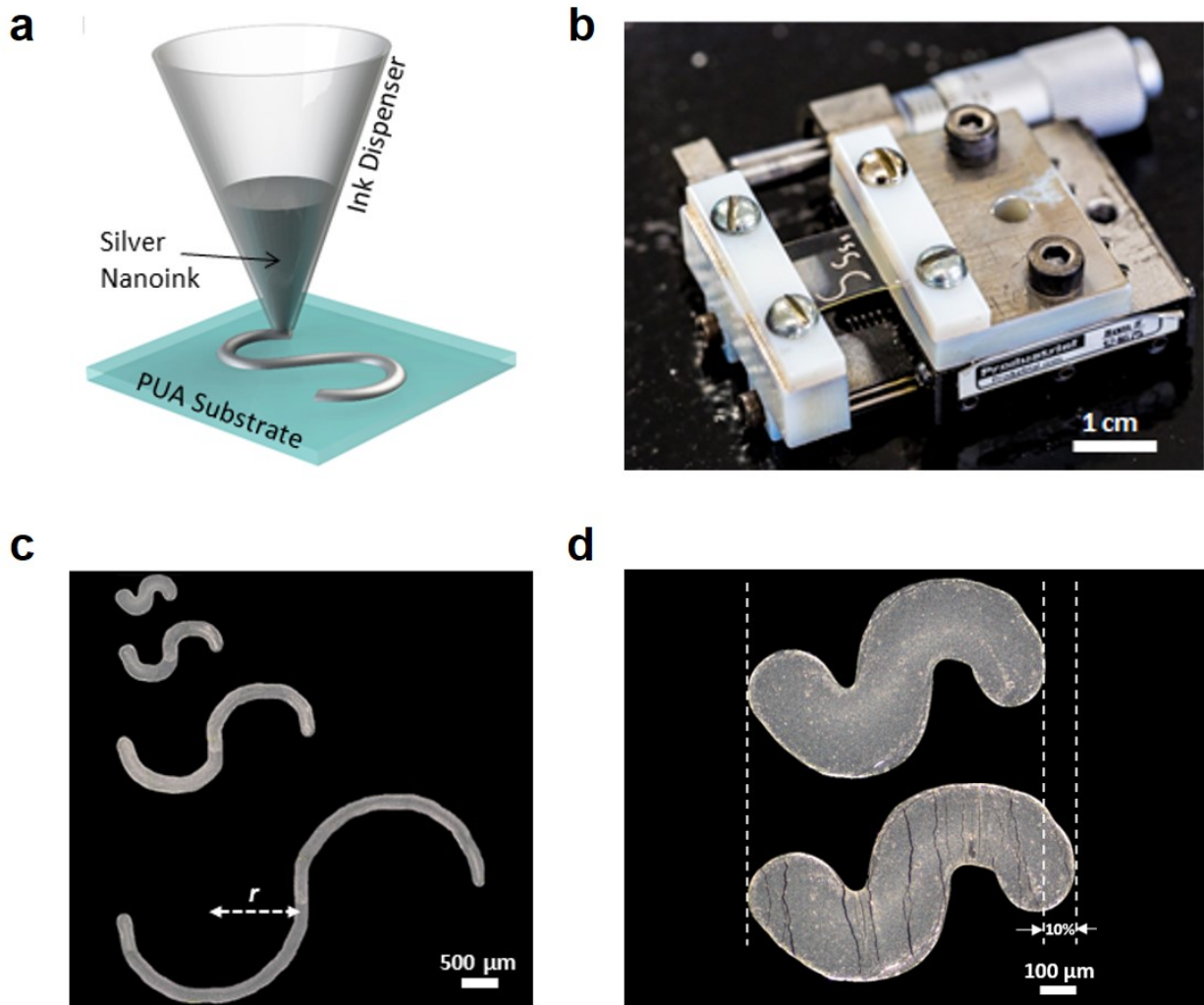


Figure 2.1 Fully printed stretchable conductor and strain gauge using AgNPs. (a) Schematic diagram of the device. (b) The sample fixed onto a linear stage which is used to do the stretching test. (c) Optical microscope image of the printed device with the radius of 200 μm , 400 μm , 800 μm and 1600 μm from top to the bottom respectively (d) Optical image of the device with the radius of 200 μm before and after 10% strain stretching.

After finishing the fabrication process, the in situ measurement in terms of the relationship between strain and the relative change of Ag patterns resistance was conducted by a linear stage shown in Figure 2.1b. The displacement of the device (ΔL) was controlled by the

screw with the scale on the back corner of the linear stage and the resolution of the screw is $10\ \mu\text{m}$. To investigate the relationship of the stretchability and the geometry design, we had printed the serpentine Ag patterns with different radius (r) varies from $200\ \mu\text{m}$ to $1600\ \mu\text{m}$ with a ratio of 2, indicated in Figure 2.1c. And we picked the pattern with smallest radius ($200\ \mu\text{m}$) as an example to show the appearance of the device before and after stretching with a strain of 10 percent. As illustrated in Figure 2.1d, the original device shown in the upper part was uniform and smooth, while the device under 10% strain indicated in the lower part displayed many large cracks throughout the pattern, which could reduce the conductivity of the device significantly. Also, the SEM image and AFM image of the Ag nanoink have been given in Figure 2.2a and Figure 2.2b respectively to characterize the surface morphology of the AgNPs whose diameter is estimated as $200\ \text{nm}$ from the images. Additionally, it could be seen that unlike the nanowires [84, 86, 98] or nanotubes [54, 67, 73], the Ag nanoink material is consist of particles connected with each other and the particles might be apart from each other under large stretching strain, resulting in the reduction of conductivity or even insulating. However, we would still use the Ag nanoink as the materials for stretchable electronics due to its better electrical performance and stability as far as we could focus on the geometry design like we did in Figure 2.1c to make it work under higher strain.

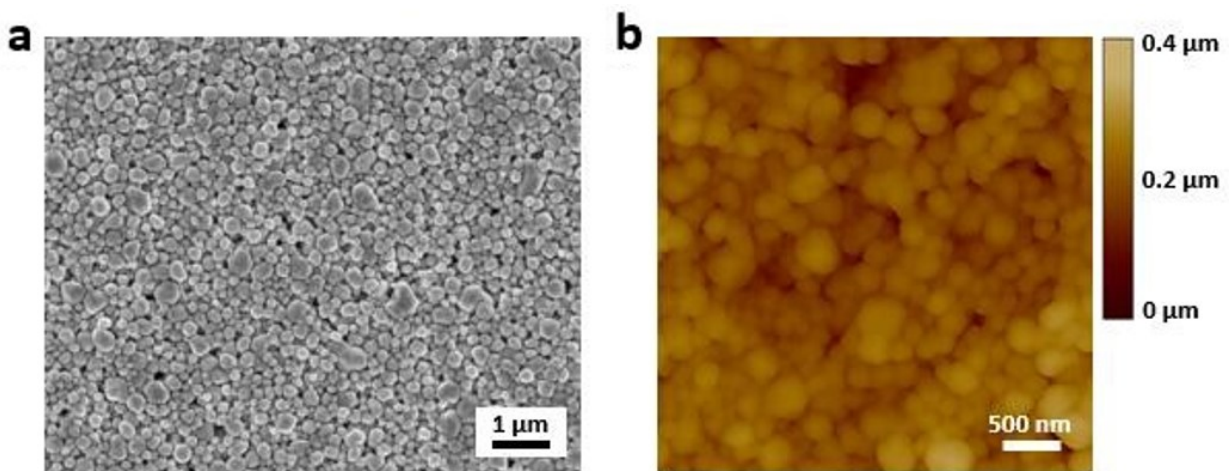


Figure 2.2 (a) SEM image of the AgNPs film. (b) AFM image of the AgNPs film.

The relationship of strain and relative change of the resistance for the patterns with different radius, including the results of the straight line pattern as a comparison, is shown in Figure 2.3a.

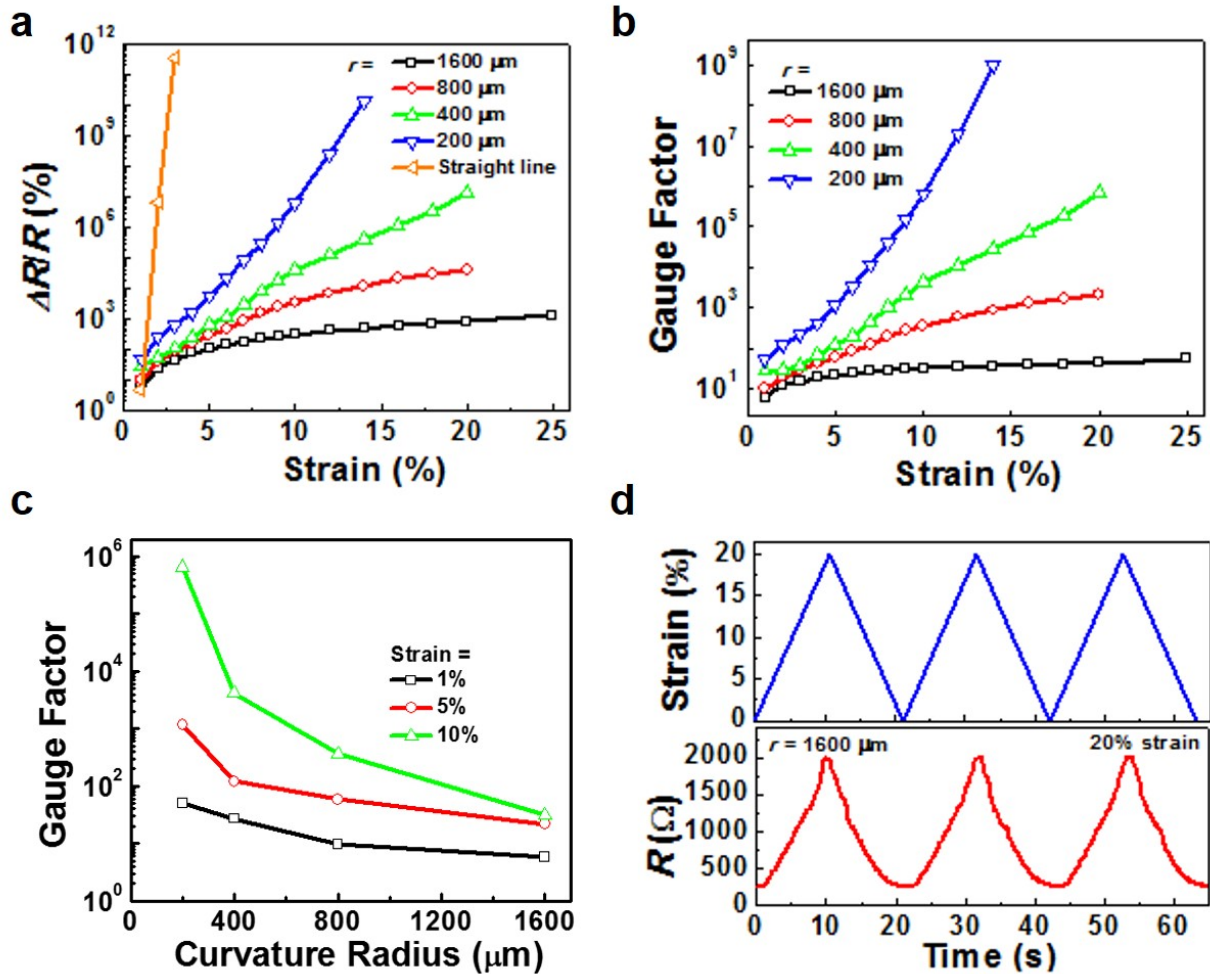


Figure 2.3 Stretchability of the fully printed device using AgNPs. (a) The stretchability of the device with different radius including that of the straight line device. (b) The extracted gauge factor as a function of strain for the device with different radius. (c) The gauge factor as a function of devices radius under different strain of 1%, 5% and 10%. (d) The time response of the device with the radius of 1600 μm while being stretched between 0% strain and 20% strain back and forth.

As expected, the device with the pattern of straight line could only be stretched less than 2 percent with a significant change in resistance of 12 orders of magnitude (yellow curve), while the device with the pattern of serpentine structure could be stretched more (the other

four curves). Furthermore, the pattern with smallest radius ($200\ \mu\text{m}$) could be stretched to 12% before become insulating (blue curve), and more amazingly, the pattern with larger radius ($1600\ \mu\text{m}$) could be stretched up to 25% with only 13 times change in resistance, where the stretchability of the device is limited by the stretchability of the substrate because the PUA substrate ruptures after 25% strain. And we extract the Gauge Factor (defined as $(\Delta R/R)/(\Delta L/L)$) which indicates the sensitivity of the device under strain for all the devices and plot them as a function of strain, illustrated in Figure 2.3b. The results perform the similar trend with Figure 2.3a. The pattern with the radius of $200\ \mu\text{m}$ achieves a very high gauge factor of 10^8 under 12% strain, which demonstrates the potential application for the device as a strain gauge due to its better performance than the conventional metal strain gauge in terms of both stretchability and sensitivity. And the pattern with the radius of $1600\ \mu\text{m}$, which could be stretched beyond 25% with the gauge factor of 52, demonstrates its application as a stretchable conductor because of its higher stretchability and better electrical performance. In Figure 2.3c, we plot the curve for the radius of the pattern as a function of gauge factor under different strain. And the gauge factor shows monotonic trend as the radius increasing, which again indicates the pattern with smaller radius is more sensitive and the pattern with larger radius is more stretchable.

We also measured the stability of the device by fixing the device onto a syringe pump and stretch and release the sample back and forth with a speed of 1 cm/min. The upper graph of Figure 2.3d (blue curve) shows the sketches about how the strain taken by the sample changes along the syringe pumps moving. And the lower part of Figure 2.3d (red curve) illustrates the experiment results about how the resistance of the Ag pattern changes along the syringe pumps moving, which almost follows the same trend with the blue curve above, demonstrating the performance of the device is repeatable and stable. Moreover, we had stretched the device with the radius of $1600\ \mu\text{m}$ and $200\ \mu\text{m}$ up to 1000 cycles under 10% strain and plot the results in Figure 2.4a and 2.4b respectively, in which the lower black circle represents the original value of resistance and the upper red square represents

the resistance of the devices after multiple stretching cycles. Being stretched to 10%, the resistance increases two times from ~ 150 Ohm to ~ 450 Ohm for the device with the radius of $1600 \mu\text{m}$, by contrast, the resistance of the device with the radius of $200 \mu\text{m}$ changes dramatically almost 7 orders of magnitude. Meanwhile, both of the two devices show stable value in term of the resistance for either release status or stretched status, indicating the performance of the device is reliable.

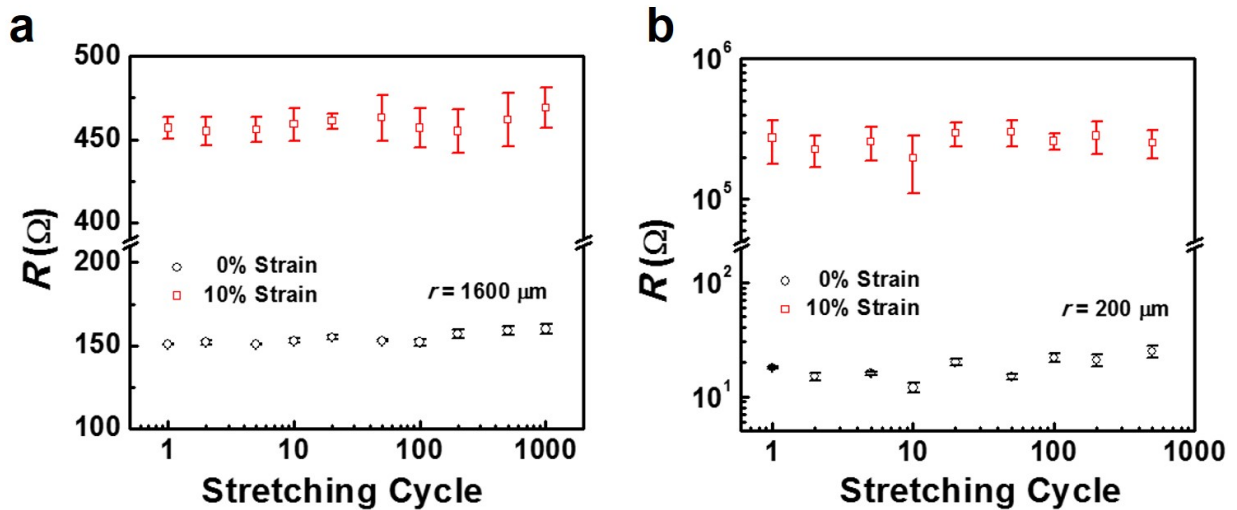


Figure 2.4 The stability of the printed devices with the radius of (a) $1600 \mu\text{m}$ and (b) $200 \mu\text{m}$ under stretching test of 10% strain up to 1000 cycles.

As mentioned above, the resistance of the device would reduce when stretched due to the formed crack under strain, however, the strain distribution is nonuniform throughout the whole serpentine structure when stretched [31]. So we have done the simulation using COMSOL to figure out the strain distribution for the device with the radius of $200 \mu\text{m}$ and $1600 \mu\text{m}$ under 10% strain, shown in Figure 2.5a and 2.5b respectively. The pattern in the back with black profile represents the original status of the device when the colorful pattern in the front shows the devices status under 10% strain. For both of the two devices, the strain had been mainly concentrated upon the crest or trough of the wavy structure, which is referred to the red or pink color. And for the other area, the strain is relatively small, which is corresponded to the blue color. When comparing the two devices, one can see the largest

strain undertaken by the device with the radius of $200\ \mu\text{m}$ (0.45%) is almost one order of magnitude more than that stood by the device with the radius of $1600\ \mu\text{m}$ (0.065%), which could interpret the reason why the device with smaller radius is more sensitive to the strain and the device with larger radius is more stretchable.

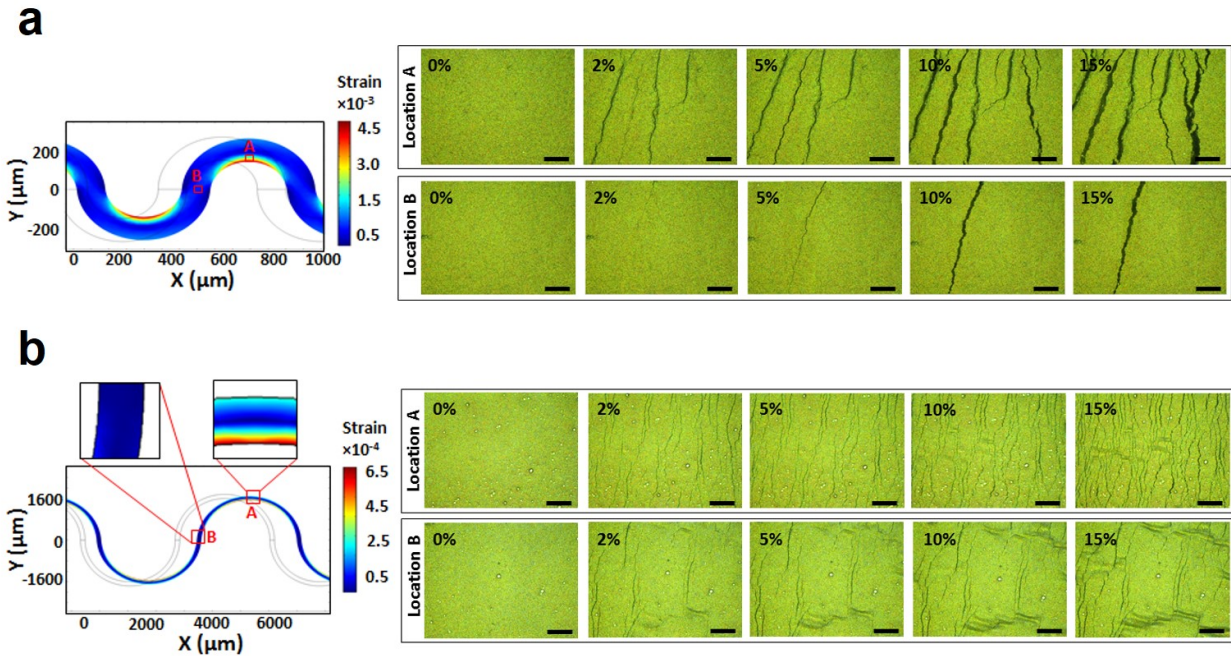


Figure 2.5 Simulation results and optical images for fully printed AgNPs devices. (a) The left part is the simulated strain distribution for the device with the radius of $200\ \mu\text{m}$ under 10% strain and the right part is the optical images of the locations with the highest strain (Location A) and the lowest strain (Location B) under different amount of strain from 0% to 15% . (b) Similarly, the left part is the strain distribution for the device with the radius of $1600\ \mu\text{m}$ and the right part is the optical images for the same locations with (a) under the same strain.

To further confirm the results got from the simulation, we pick up two locations from the devices at which the strain is nearly largest (Location A) and smallest (Location B) to check under the Real-time Extended Depth of Field (EDF) microscopy for comparing the deformation in different regions of the device, shown in the right part of Figure 2.5. For both of the devices, with the strain increasing, the number of cracks becomes more and the width of the cracks become larger for location A compared with that of location B, which

is consistent with the simulation results (the strain undertaken by location A is higher). To be pointed out, the dark lines in horizontal direction for location B of the device with the radius of $1600\ \mu\text{m}$ is the buckling (rather than cracks) caused by the compress force in the vertical direction when the sample is being stretched in the horizontal direction. And when comparing the microscope image of the location A in both of the two devices, the cracks in the device with the larger radius are much thinner than that in the device with smaller radius, which offers another evidence for the fact that the device with larger radius could stand more strain, and thus, more stretchable.

2.4 Potential Application

Two applications of the printed AgNPs devices are demonstrated as follows.

2.4.1 Stretchable Conductor

Due to its higher stretchability, we come up with the potential application for the device with the radius of $1600\ \mu\text{m}$ as a stretchable conductor which could be potentially used as the actuators, interconnects, LED sensors or wearable electronics. In the experiments, we fixed the device onto the syringe pump and connected the device with a commercial available LED in series using the liquid metal and conductive needle as the connection. The device was stretched back and forth from 0% strain to 20% strain. And the time response has been plotted in Figure 2.6. Both the on current and the off current are stable from cycle to cycle when the sample was stretched to 20% and the current dropped from $\sim 11\ \text{mA}$ to $\sim 2\ \text{mA}$, where the performance is not perfect but acceptable.

And from the Figure 2.7a and 2.7b, one can find the illumination of the LED is comparable before and after the sample was stretched, indicating the stretchable conductor is reliable, which may offer a new path to realize the stretchable display.

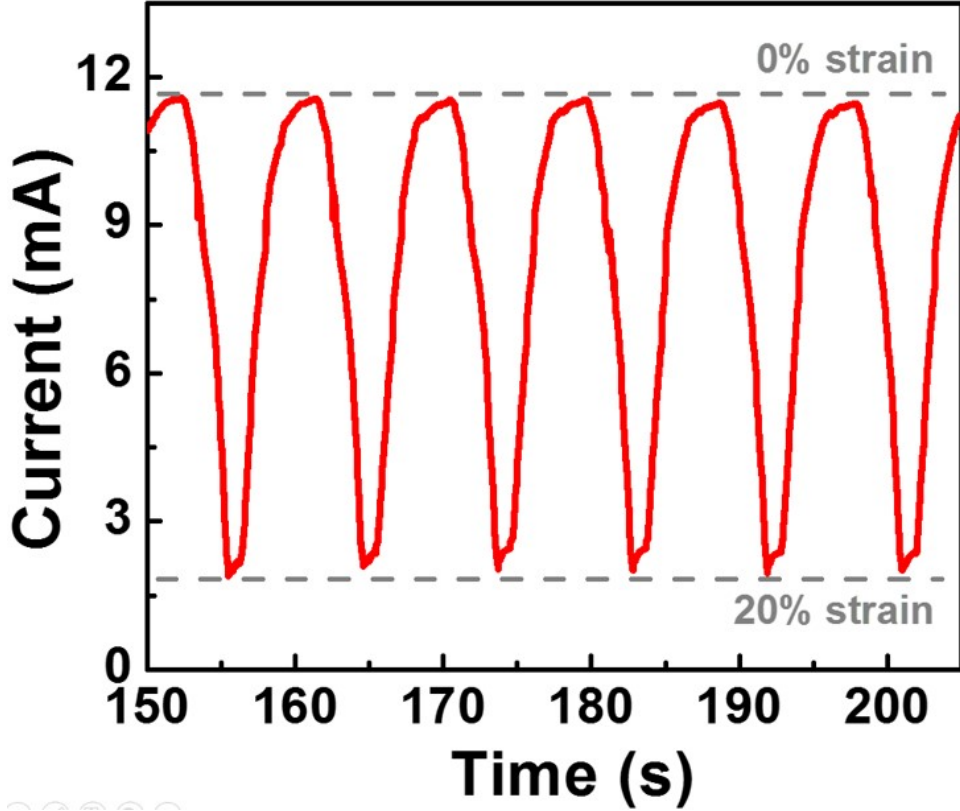


Figure 2.6 The current of the LED when the connected stretchable conductor had been stretching between 0% strain and 20% strain.

2.4.2 Strain Gauge

Even though not as much as the device with the radius of $1600 \mu\text{m}$ in terms of the stretchability, the device with the radius of $400 \mu\text{m}$ could still be stretched to 20% for single segment (higher than conventional metal strain gauge), which means it could still be wrapped onto some irregular surfaces where the strain is limited. Additionally, the device with radius of $400 \mu\text{m}$ is very sensitive to the strain so that it achieve the gauge factor of 10^6 under 20% strain, which is way higher than the conventional metal strain gauge, ensuring its better performance as a strain gauge. In this work, we propose its application as a strain gauge to monitor the finger motion. Basically, we printed several segments of the serpentine pattern with the radius of $400 \mu\text{m}$ to make sure the length of the pattern is longer than the displacement of the finger joint when bended and use the liquid metal droplet and the copper

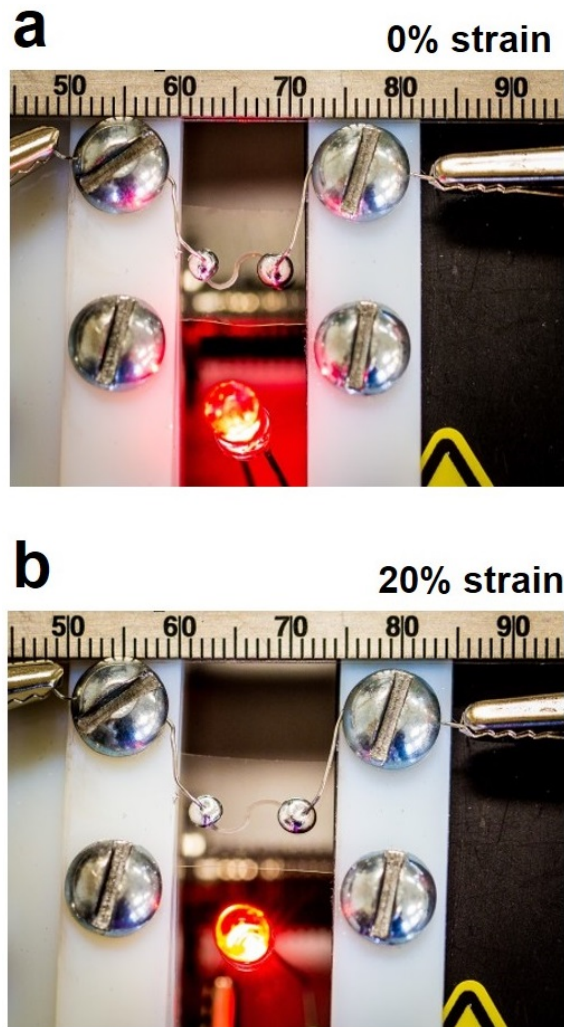


Figure 2.7 Fully printed AgNPs device as a stretchable conductor. The illumination of the LED when the connected stretchable conductor was under (a) 0% strain (release status) and (b) 20% strain (stretched status).

wire as the connection when doing the measurement to avoid the mechanical failure during the movement of the finger. Besides, to further protect the connections and to make the Ag pattern more stretchable, another layer of PUA had been poured on top of the whole device including the connections and cured under the UV light to form the encapsulation. And finally the device with encapsulation was attached to the glove by a double-side tap, shown in the insert figure of Figure 2.8a. Since the performance for the device with multiple segments would be slightly different with that of the device with single segment, we had

re-measured the stretchability of the device using the syringe pump (Figure 2.8a). When the finger moved forward from gesture I to VI and move backward from gesture VI to I step by step (Figure 2.8c), the relative change of the devices resistance showed accordingly change, as shown in Figure 2.8b, where each stage clearly corresponds each gesture in Figure 2.8c, and we estimated the strain for each gesture according to the relative change of the resistance we get from Figure 2.8b and corresponded that to Figure 2.8a. From the results presented, we demonstrate our fully printed stretchable strain gauge is compatible for detecting the finger motion of human beings with a large range of strain.

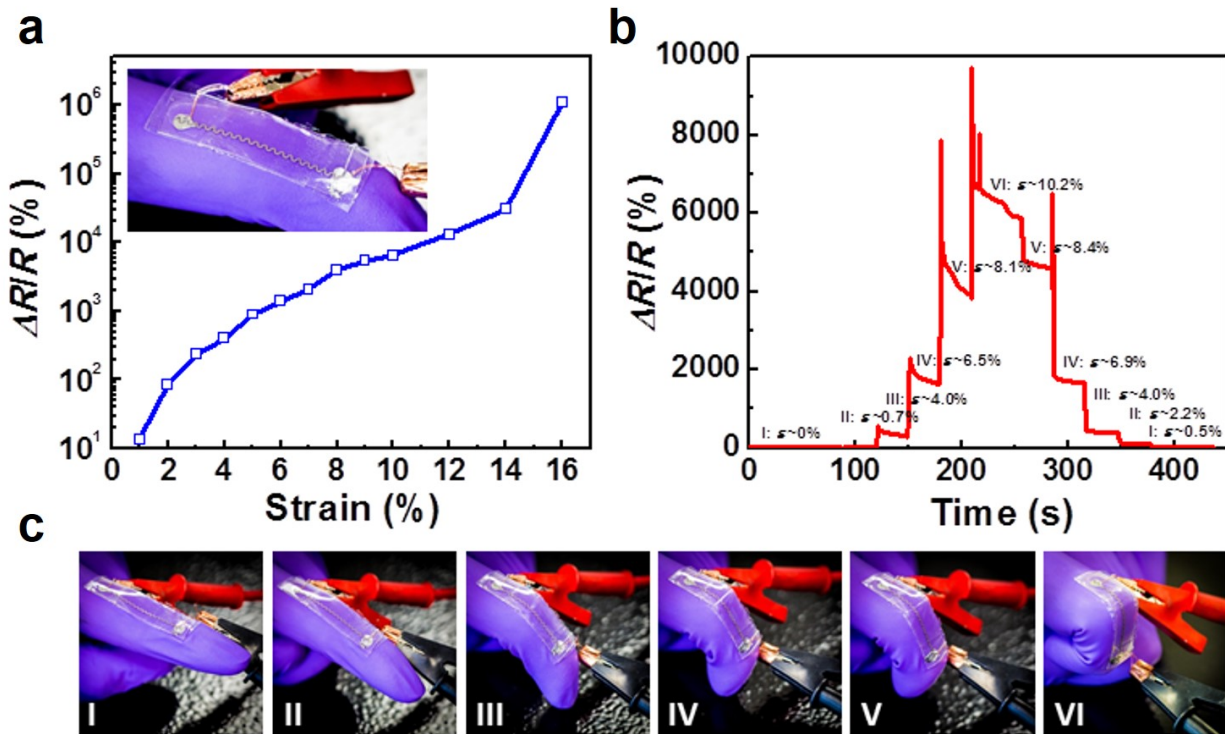


Figure 2.8 Fully printed AgNPs device as a strain gauge for detecting the finger motion. (a) The relative change of resistance as a function of strain for the printed device with multiple serpentine sections and the insert figure shows how we did the finger motion detection using the printed device. (b) The resistance response at each corresponding stage of (c). Photograph of the strain gauge attached to the finger with different bend angles.

2.5 Summary

In summary, we have successfully fabricated the fully printed stretchable devices by the Ag nanoink on an elastomer PUA substrate using a serpentine structure. And the performance of the devices is tunable by varying the radius of the serpentine pattern. The device with smaller radius had been demonstrated as a strain gauge to monitor the finger motion of human beings due to its high sensitivity to the strain when the device with larger radius had been demonstrated as a stretchable conductor to drive a conventional LED due to its higher stretchability. The strategy presented here will be beneficial for the development of stretchable electronic applications, such as interconnects, wearable sensors, actuators and stretchable light emitting displays.

CHAPTER 3

PATTERNING SILVER NANOWIRES ON VARIOUS SUBSTRATES USING A DIRECT PRINTING METHOD FOR STRETCHABLE CONDUCTORS, SENSORS AND DISPLAYS

A unique direct printing method is developed to additively pattern silver nanowires (AgNWs) with length of up to $\sim 40 \mu\text{m}$. Uniform and well-defined AgNW features are printed on various substrates by optimizing a series of parameters including ink composition, printing speed, nozzle size, substrate temperature, and hydrophobicity of the substrate surface. The capability of directly printing such long AgNWs is essential for stretchable electronics applications where mechanical compliance is required as manifested by a systematic study comparing the electrical and electromechanical performance of printed AgNW features with different nanowire lengths. Such printed AgNWs are used to demonstrate biaxially stretchable conductors, ultrasensitive capacitive pressure sensor arrays, and stretchable electroluminescent displays, indicating their great potential for applications in low-cost wearable electronics. This strategy is adaptable to other material platforms like semiconducting nanowires, which may offer a cost-effective entry to various nanowire-based mechanically compliant sensory and optoelectronic systems.

3.1 Introduction

Materials with high electrical conductivity and excellent mechanical compliance are crucial to realize stretchable electronics [99]. Researchers have explored a wide range of materials, among which are carbon nanotubes [100, 101], graphene [102], metal nanowires [103, 104], conductive polymers [105], and metal nanoparticles dispersed in elastomers [106]. Silver nanowires (AgNWs), in particular, are considered as one of the most promising candidates owing to the combination of superior conductivity, relatively low cost, and the ability to

form highly stretchable and transparent films [107]. In recent years, AgNWs have been extensively investigated as not only stretchable conductors but also electrodes of various flexible and stretchable functional devices like light emitting diodes [108, 109], solar cells [110], and electronic skins [111]. Despite the significant progress in the field, patterning AgNWs by additive manufacturing methods such as inkjet printing that can significantly reduce the fabrication cost and improve the design flexibility [112] has rarely been investigated and proven extremely challenging. In most published studies, the AgNW networks were deposited by drop casting or rod coating that does not possess patterning capability unless combined with specially engineered hydrophobic/hydrophilic micropatterns to manipulate wetting of the AgNW dispersion on substrate surfaces [113]. There are several reports of patterning AgNW networks by stencil printing [104] or spray coating [114] through a shadow mask, albeit with patterning resolution limited to millimeter scale and inevitable material waste. Indeed, the use of masks greatly compromises the adaptability and flexibility of these methods.

Direct writing methods such as fountain pen nanolithography have been proven powerful tools for delivering nanomaterials onto various substrates with high resolution and versatility [115]. The reasons that the direct printing of AgNWs can be extremely challenging are multifold [116]. First, the AgNWs used as stretchable conductors are usually at least tens of micrometers long [103], which significantly exceeds the empirically determined printable size of $a/50$ (a is the size of the printing nozzle) for regular inkjet printers. Hence the nozzle tends to be clogged very easily. An additional issue is the lack of effective control over the ink bleeding and solvent evaporation because of the low volume content of AgNWs in the ink. As a result, the printed AgNW features often possess rather rough edges and poor uniformity. Recently, researchers have tried reducing the nanowire length by ultrasonication scissoring [116, 117] or tuning the ink rheology by adding polymers to facilitate direct printing [118]. Although very sharp and uniform features can be obtained, the conductivity and stretchability are greatly compromised because of the dramatically reduced nanowire length

or the presence of polymer additives. Herein, we report a method for directly printing AgNWs with length up to $\sim 40 \mu\text{m}$ on a variety of substrates including silicon wafer, polyimide, glass, polydimethylsiloxane (PDMS), and 3M VHB tape. By optimizing a series of printing parameters, we were able to obtain very well defined and uniform AgNW features that can be used as stretchable interconnections as well as electrodes for capacitive pressure sensor arrays and stretchable electroluminescent (EL) displays. This unique additive patterning method may find applications in a wide range of nanowire-based functional stretchable electronic and optoelectronic systems.

3.2 Fabrication Process and Measurement Setup

Materials: Water-based AgNW dispersion was purchased from ACS Materials, LLC. PDMS (Sylgard 184) and Ecoflex (0010) were purchased from Dow Corning and Smooth-on, respectively. Ethylene glycol and Triton X-100 were purchased from Alfa Aesar and Sigma Aldrich, respectively. Liquid metal (Galinstan) and PELCO colloidal silver paste were purchased from Rotometals and Ted Pella, Inc., respectively. Orange (D611), green (D512), and blue-green (D502) phosphors were purchased from Shanghai KPT Co., Ltd. Polyimide (PI-2525) was purchased from HD Microsystems. Carbon nanotube (CNT) paste (VC101) was purchased from SouthWest NanoTechnologies.

Printing AgNWs: The water-based AgNW dispersion was first centrifuged to remove Ag particles and nanowire aggregates. 20 vol% ethylene glycol was then added to the dispersion to tune the ink rheology and to avoid nonuniform features caused by severe coffee-ring effect of pure water. The ink was subsequently printed on pristine surface of Si wafers, glass slides or polyimide films using a Sonoplot Microplotter at a substrate temperature of $\sim 60^\circ\text{C}$. Specifically, the glass micropipette (purchased directly from Sonoplot) was gradually brought into contact with the substrate surface, which induced a meniscus to appear and to bridge the micropipette and the substrate. The micropipette was then moved back-and-

forth along a pre-designed trajectory in a controlled manner, dragging the meniscus around, and leaving some AgNWs on the surface after each pass. Generally, sufficiently conductive features can be obtained by ~ 40 printing runs. For printing on PDMS, the surface of PDMS was treated with O₂ plasma (30 W, 15 s), and 0.01 vol% Triton X-100 was added to the ink to tune its surface energy. Unless otherwise noted, we used the following optimized parameters for printing AgNWs: nozzle size of $\sim 200 \mu\text{m}$, nozzle moving speed of 5 mm/s, intentionally controlled contact angle of $\sim 60^\circ$ (for the sake of meniscus formation) and substrate temperature of $\sim 60^\circ\text{C}$. The printed AgNW features were measured and used directly without any annealing step.

Fabricating Capacitive Pressure Sensors: Parallel AgNW lines were first printed on PDMS films. A copper wire was then attached to each AgNW line using colloidal silver paste as measurement lead. The sensor array was then assembled by sequentially stacking an AgNW-PDMS film, an Ecoflex film, and the other AgNW-PDMS film in a manner such that the two sets of AgNW lines face and are perpendicular to each other. Each intersection of the top and bottom AgNW lines defines one pixel.

Fabricating EL Displays: PDMS and phosphors were mixed thoroughly with a weight ratio of 2:1 and then casted to form thin films of $\sim 130 \mu\text{m}$ thick. AgNW lines were then printed onto both sides of the composite film to fabricate the display array. The EL display array adopts a similar structure with the pressure sensor array. For the MSU-shaped display, AgNWs were printed with the desired pattern on one side of the PDMS/phosphor composite film, and CNT paste was painted onto the other side as the back electrode. For the EL device used for luminance measurements and stretching tests, continuous AgNW networks were blade-coated on both sides of a composite film which was then sliced into narrow strips. Copper wires were used as the measurement leads and all devices were fully encapsulated in PDMS before testing.

Electrical and Stretchability Measurements: All electrical characteristics including the I-V curve, the resistance and the capacitance were measured using an Agilent B1500A Semicon-

ductor Parameter Analyzer. Scanning electron micrographs and optical micrographs were captured with a Hitachi S-4700II field emission SEM(FESEM) and an Olympus BX51 optical microscope, respectively. The stretching tests were conducted automatically using a syringe pump (Legato 110). For recording the capacitance-pressure characteristics of the pressure sensor, a set of weights was used to apply incremental pressure to the sensor. For EL display characterization, AC voltage was generated from a function generator (Agilent 33220A) and then amplified by a voltage amplifier (Trek 2210). All measurements were carried out under ambient conditions.

3.3 Results and Discussion

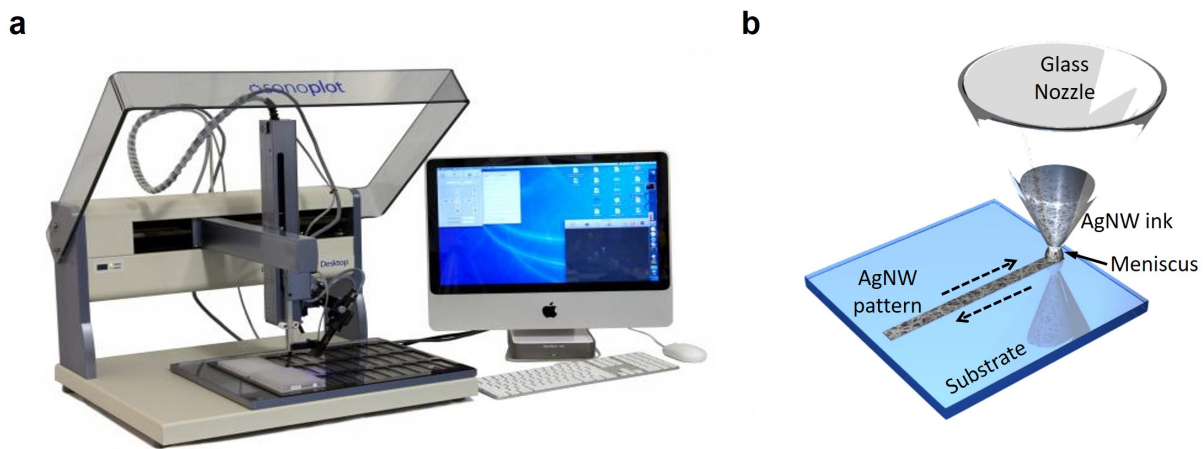


Figure 3.1 (a)Printer used for this work. (b)Schematic diagram illustrating the printing process.

The printing process is illustrated in Figure 3.1. Briefly, AgNW ink is loaded into a glass micropipette by capillary force. The micropipette is then brought into contact with the substrate surface. A liquid meniscus is subsequently formed if the AgNW ink wets the substrate surface. Finally, the micropipette is moved along a predefined path back-and-forth in a controlled manner and drags the meniscus around. AgNWs are consequently deposited on the trajectory of the meniscus. Unlike conventional inkjet printing, this direct

writing process does not involve delivering discrete liquid droplets onto the substrate and thus has no problem of uncontrollable solvent evaporation or ink bleeding. In fact, the solvent dries almost immediately after the meniscus passes. Additionally, nozzle clogging can be effectively alleviated by using micropipettes with bigger openings and expelling AgNW aggregates regularly. It is nontrivial, however, to obtain uniform and sharp printed features. A number of parameters including nozzle size, micropipette moving speed, hydrophobicity of substrate surface, substrate temperature as well as solvent composition, need to be carefully optimized. And the details have been illustrated as follows.

1. Effect of nozzle size on the printing results.

Figure 3.2 shows the optical micrographs of the AgNWs printed using nozzles with openings of $\sim 500 \mu\text{m}$ (Fig. 3.2a) and $200 \mu\text{m}$ (Fig. 3.2b). Both nozzles could give very uniform features, albeit the $200 \mu\text{m}$ nozzle led to a finer feature and sharper edges. Most of our results are based AgNWs printed using a $\sim 200 \mu\text{m}$ nozzle.

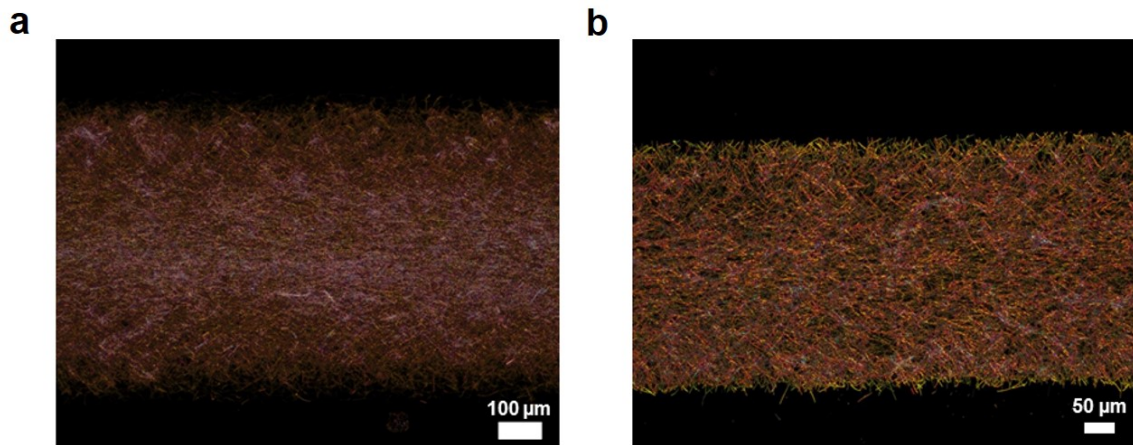


Figure 3.2 Optical micrographs of AgNWs printed on Si wafer using nozzles with openings of (a) $500 \mu\text{m}$ and (b) $200 \mu\text{m}$

2. Effect of nozzle moving speed on the printing results.

Figure 3.3 presents the optical micrographs of three AgNW features printed with different nozzle moving speeds. As expected, higher moving speeds lead to lower nanowire densities. On the other hand, the nanowires have more time to aggregate at the bottom of the nozzle if

the printing speed is too low. Therefore, considering this trade-off between network density and uniformity, we chose a printing speed of ~ 5 mm/s for most of our samples.

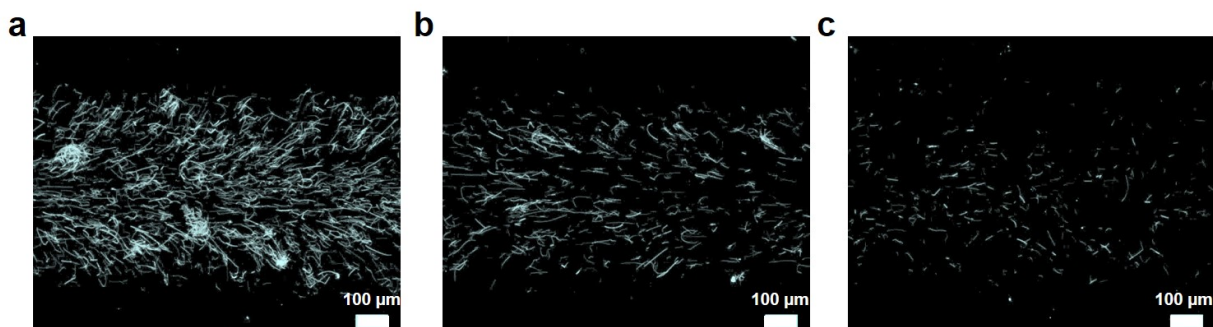


Figure 3.3 Optical microscope images of the AgNW features printed on Si wafer with nozzle moving speeds of (a) 0.5 mm/s, (b) 5 mm/s and (c) 50 mm/s.

3. Effect of substrate hydrophobicity on the printing quality.

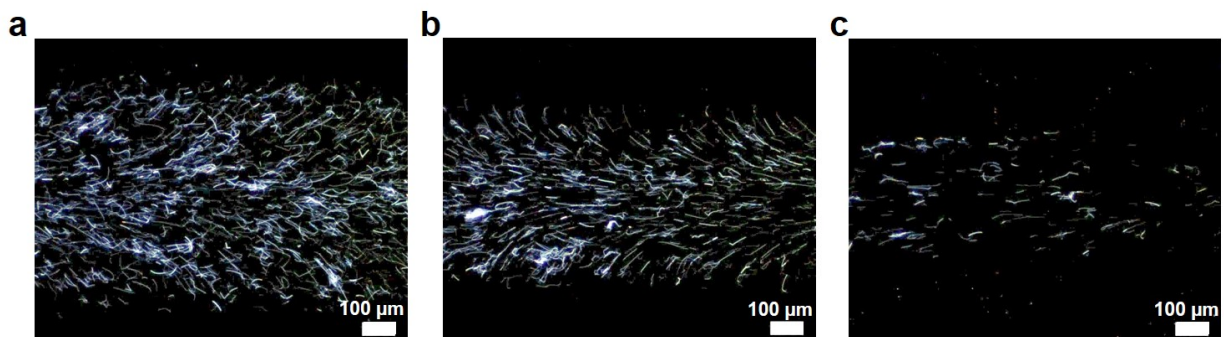


Figure 3.4 Micrographs of AgNW network printed on Si wafer with different contact angle of (a) $<20^\circ$, (b) $\sim 60^\circ$, (c) $>90^\circ$

The wetting behavior of the ink on substrate surface plays a critical role in meniscus formation, which in turn controls the morphology of the printed features. Pristine surface of silicon wafer (contact angle $\varphi \sim 60^\circ$) was found to offer the best results for water based inks (Figure 3.4b). Treatment with O_2 plasma or Rain-X renders the Si surface very hydrophilic ($\varphi < 20^\circ$) or hydrophobic ($\varphi > 90^\circ$). As shown in Figure 3.4a and c, a contact angle of $<20^\circ$ leads to very wide features while almost no nanowire can be printed on hydrophobic surface. So, we intentionally tuned the contact angle to be $\sim 60^\circ$ for all substrates before printing

AgNWs on them.

4. The effect of substrate temperature on the printing quality.

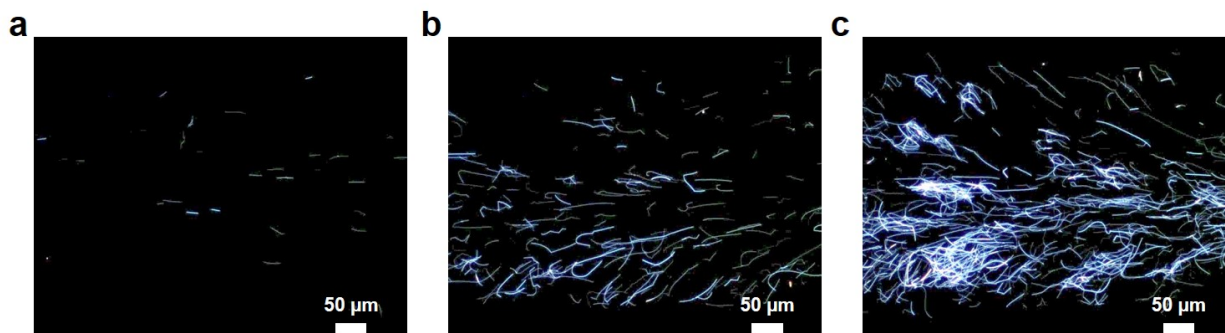


Figure 3.5 Micrographs of AgNW networks printed on Si wafer under different temperatures: (a) room temperature, (b) 60 °C and (c) 100 °C.

As expected, substrate temperature also plays an important role. As shown in Figure 3.5, if the temperature is too low, the solvent evaporates very slowly so that only very few nanowires can be left on the surface after each printing pass. On the other hand, at very high substrate temperatures, the solvent will evaporate so fast that lots of aggregates are formed and deposited on the surface. Therefore, the substrate temperature needs to be carefully controlled during the printing process. We found that a good balance between nanowire network density and uniformity could be achieved when the substrate temperature was set to around 60 °C.

5. Dot-by-dot printing versus continuous printing.

We had also tried printing the AgNWs network in a dot-by-dot manner. Briefly, the tip was brought into contact with the surface, and then lifted completely, leaving a large droplet behind on the surface. The same process was repeated after moving the tip to an adjacent location. After repeating such process for many times, very conductive features could be obtained, albeit with an apparently poorer uniformity than those by continuous printing, as shown in Figure 3.6a and in comparison with Figure 3.6b.

6. Effect of surfactant concentration on the printing results on PDMS substrate.

Triton X-100 was used to tune the AgNW ink surface tension and to facilitate the print-

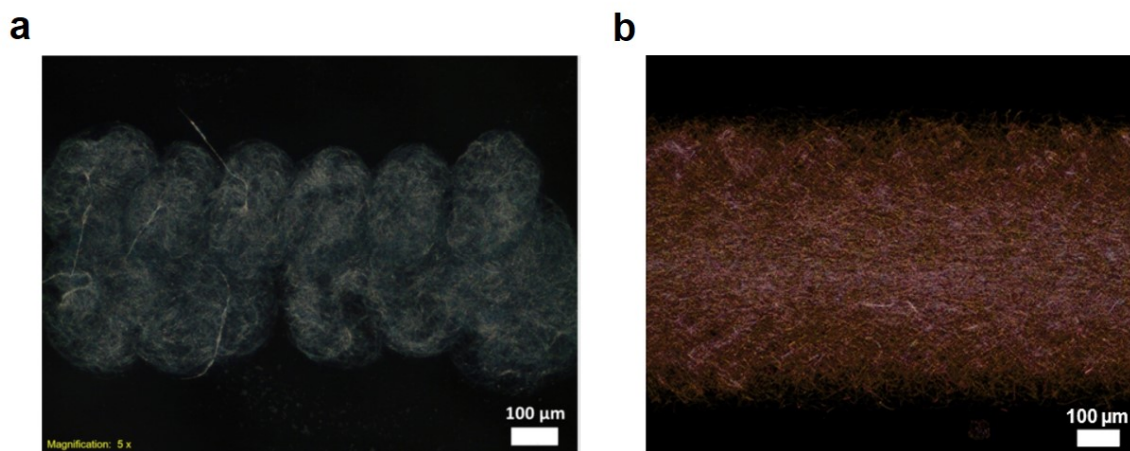


Figure 3.6 Micrograph of AgNW network printed (a) in a dot-by-dot manner and (b) in a continuous printing manner.

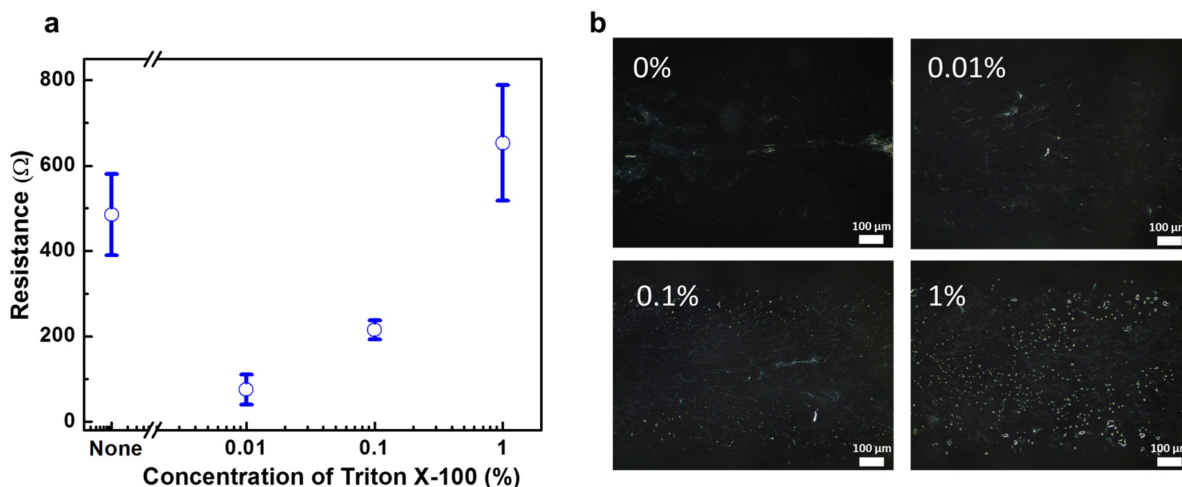


Figure 3.7 Effect of surfactant concentration on the printing results on PDMS. (a) Resistance of the AgNW networks printed on PDMS (100 printing passes) as a function of surfactant concentration in the AgNW dispersion. (b) Micrographs of AgNW networks printed on PDMS (one printing pass) using inks with different amount of surfactant.

ing on PDMS. The concentration of Triton X-100 needs to be very carefully controlled. Insufficient amount of Triton X-100 leads to inadequate wetting thus unsuccessful printing while too much Triton X-100 may affect the electrical conduction between AgNWs due to its insulating nature. By comparing the resistance of AgNW features printed from inks with different amount of Triton X-100 (other parameters were kept the same), we found that a

concentration of 0.01 vol.% gave the best electrical performance, as shown in Figure 3.7a. A close look at the microscopic morphology of the printed features provides some insights. Specifically, at a very high concentration (~ 1 vol.%), lots of particles appeared in the printed feature, which was likely due to the precipitation of Triton X-100 while the solvent evaporates. Such a high content of Triton X-100 induces a significant increase in feature resistance because all AgNWs are wrapped by thick layers of Triton X-100 which greatly suppress the electrical conduction. Considering the above, we used AgNW inks with 0.01 vol.% or 0.1 vol.% Triton X-100 for devices fabricated on PDMS.

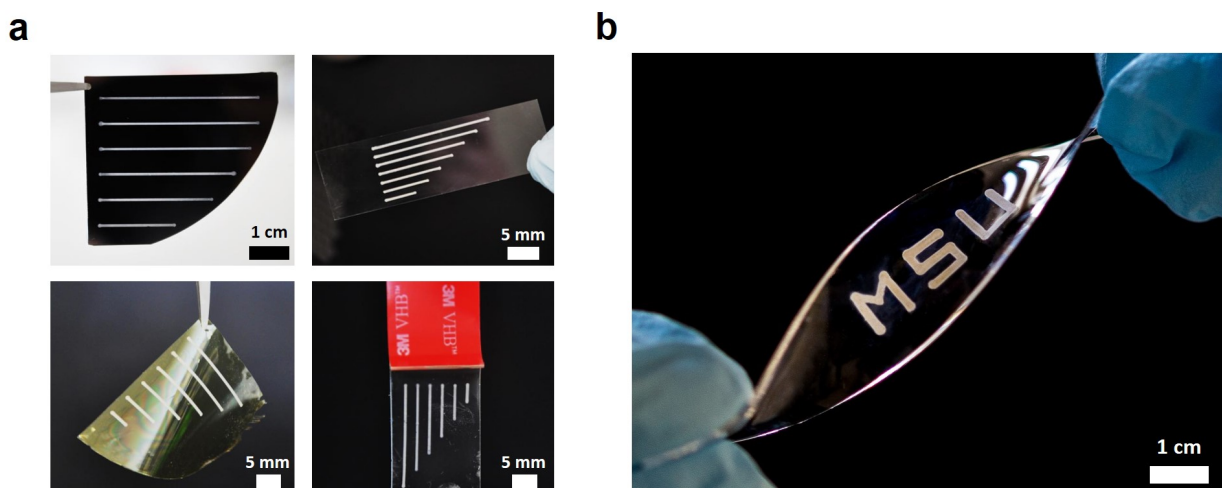


Figure 3.8 Printed AgNW patterns on various substrates. (a) MSU shaped AgNW patterns printed on PDMS. Scale bar: 1 cm. (b) Straight line patterns of AgNWs printed on silicon wafer, glass slide, polyimide thin film, and VHB tape. Scale bars: 2 cm.

By adjusting the above parameters, we were able to achieve optimal conditions for successfully printing uniform AgNW patterns onto various substrates, as shown in Figure 3.8a and b. Figure 3.9 presents the dark field optical micrograph and scanning electron microscope (SEM) image of the dense AgNW network printed on Si wafer, revealing very good uniformity, and well-defined sharp edges.

We have systematically studied printing of AgNW inks with different average nanowire lengths, namely 4.4, 15.6 and 38.5 μm . Figure 3.10 a,b presents their SEM images and nanowire length distribution, respectively. All three kinds of AgNWs can be printed with very

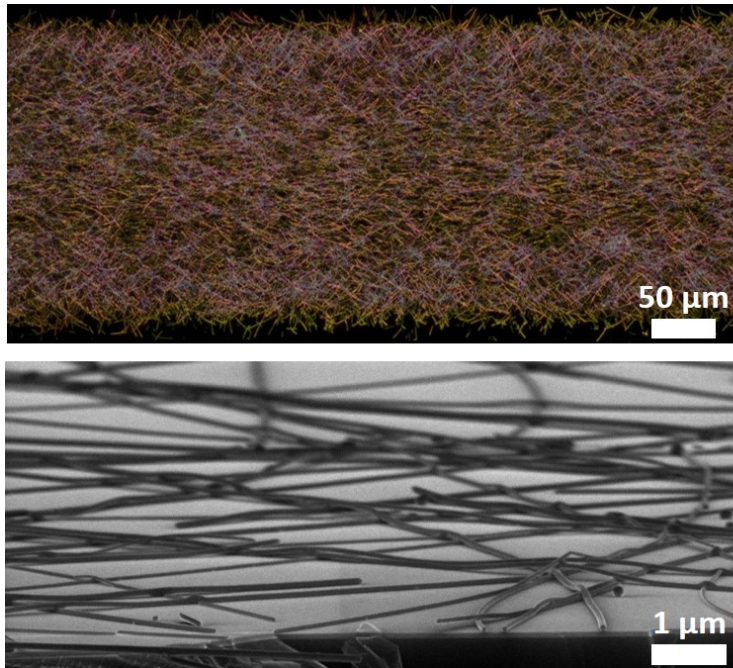


Figure 3.9 Optical micrograph (top) and SEM image (bottom) of the AgNW network printed on Si wafer with a feature width of $\approx 270 \mu\text{m}$. This feature was printed with a nozzle opening of $\approx 180 \mu\text{m}$. Scale bars: 50 and 1 μm , respectively.

well-defined and uniform features. It is impressive that the AgNWs with length significantly exceeding the rule-of-thumb printable size ($<10 \mu\text{m}$ for typical micropipettes used here) can still be printed very easily, which is likely due to the flow-induced alignment as the nanowires pass through the nozzle [116]. This is manifested by the well-aligned AgNWs on the inner wall of the micropipette. The electrical performance of the printed AgNW patterns, as shown below, greatly depends on the nanowire length. Figure 3.10c shows the resistance versus number of printing passes for all three kinds of AgNWs measured from printed features of $\approx 5000 \mu\text{m}$ long and $\approx 500 \mu\text{m}$ wide. Regardless of nanowire lengths, the feature resistance initially decreases drastically by more than an order in magnitude and starts to reduce with a much lower rate after a certain number of printing passes, implying the percolating conduction of the AgNW networks. As expected, longer nanowires require fewer printing passes to form a conductive network and have lower electrical resistance compared with patterns with shorter nanowires for a given number of passes. Figure 3.10d presents

the resistance as a function of printed feature length (feature width is $\approx 500 \mu\text{m}$). All three kinds of AgNWs show excellent linearity, indicating the AgNWs are uniformly distributed throughout the entire pattern.

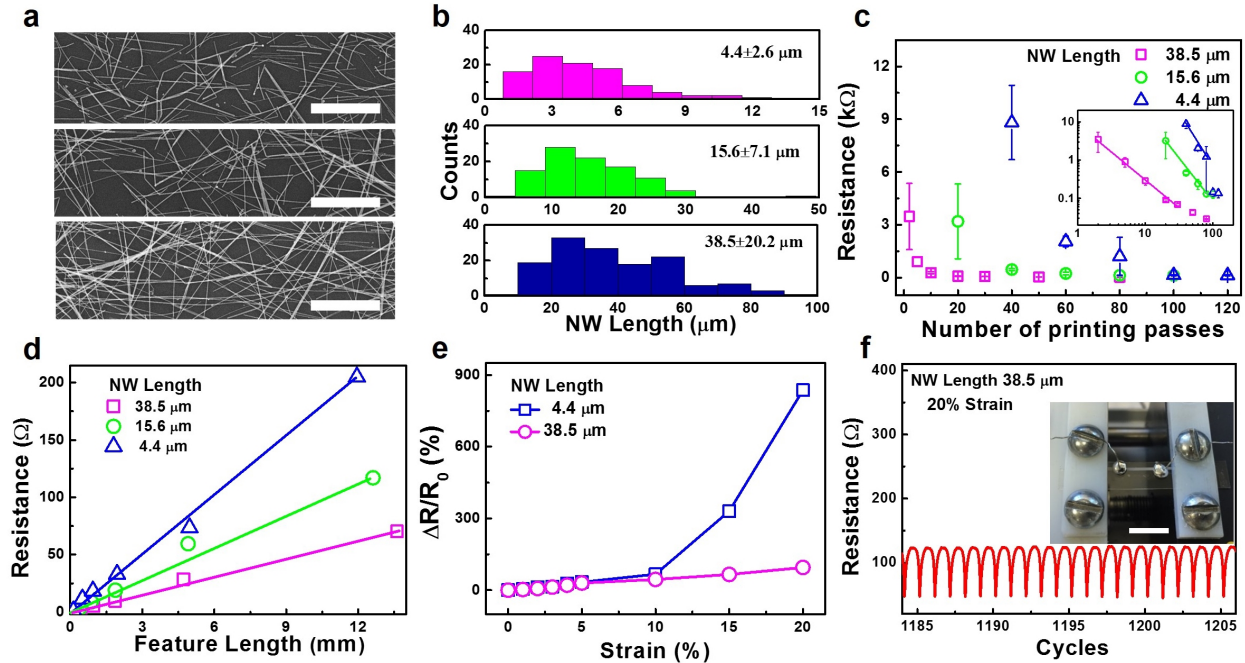


Figure 3.10 Electrical and electromechanical characterization of the printed AgNW features with different nanowire lengths. a) SEM images of the AgNW network with average nanowire length of ≈ 4.4 , ≈ 15.6 and $\approx 38.5 \mu\text{m}$ (from top to bottom). Scale bar: $5 \mu\text{m}$. b) Nanowire length distribution of the three different AgNW inks. c) Feature resistance as functions of number of printing runs for AgNWs with different nanowire lengths. The printed features are $\approx 5000 \mu\text{m}$ long and $\approx 500 \mu\text{m}$ wide. Inset: Same data presented in log scale. d) Resistance as a function of printed feature length for all three kinds of AgNW inks (feature width is $\approx 500 \mu\text{m}$ for all samples). e) Relative change in resistance as a function of tensile strain for features with average nanowire lengths of ≈ 38.5 and $\approx 4.4 \mu\text{m}$. f) Cyclic stretching test results for the feature with an average nanowire length of $\approx 38.5 \mu\text{m}$. Inset: Measurement setup. Scale bar: 1cm .

As mentioned above, AgNW is a promising candidate for stretchable conductors and we have found that the stretchability greatly depends on the nanowire length. Figure 3.10e shows the stretchability of patterns printed using AgNWs with different lengths. When stretched to 20% tensile strain, the resistance of printed features with $4.4 \mu\text{m}$ long AgNWs increases drastically to nearly ten times of its pristine value. In contrast, the resistance of

features with $38.5 \mu\text{m}$ long AgNWs changes by 90%. This difference can be interpreted by the fact that longer nanowires tend to have greater curvature and better capability to retain good interwire contacts upon stretching. The irreversible increase in resistance was induced by the cracking of AgNWs under tensile strains, which could be clearly seen in the in situ microscopic images showing the morphological change of the AgNW network under tensile strains. The reliability of printed patterns with $38.5 \mu\text{m}$ long AgNWs upon cyclic stretching tests is shown in Figure 3.10f. The patterns could maintain excellent conduction at both relaxed and stretched states throughout the course of up to 2000 stretching cycles with a maximum tensile strain of 20%.

In order to further improve the stretchability of the printed AgNW features, we prestretched the PDMS substrate to 30% strain along both parallel and perpendicular directions before printing. After printing the AgNWs onto the prestretched PDMS substrate, the preapplied strain was released and biaxial stretching tests were conducted on the AgNW patterns. As shown in the top panel of Figure 3.11a, the stretchability was greatly improved by prestretching the substrate during the printing process. The feature resistance only increases very slightly by $\approx 38\%$ (from 145 to 200 Ω) when stretched to 125% areal strain (50% strain along both horizontal and vertical directions). We have also investigated the durability of the AgNW patterns printed on the prestretched PDMS substrates. As illustrated in the bottom panel of Figure 3.11a, the feature resistance at 0 and 125% areal strains only shows very slight change throughout the 500 stretching cycles. The application of the printed AgNW pattern as stretchable interconnection was subsequently demonstrated by incorporating it into the driving circuit of a light-emitting diode (LED). As shown in Figure 3.11b, the I-V curves of the LED essentially overlap with each other during the process of stretching the AgNW interconnect to an areal strain of 125%. Hence, the LED shows no noticeable variation in luminance, as presented in the two insets of Figure 3.11b. When the areal strain is further increased to 156%, the I-V curve shows slight downshift, but is still sufficient to drive the LED. In principle, the stretchability could potentially be improved even further

by using greater prestrains during printing. To the best of our knowledge, this is the first report of printed, biaxially stretchable conductors based on AgNWs.

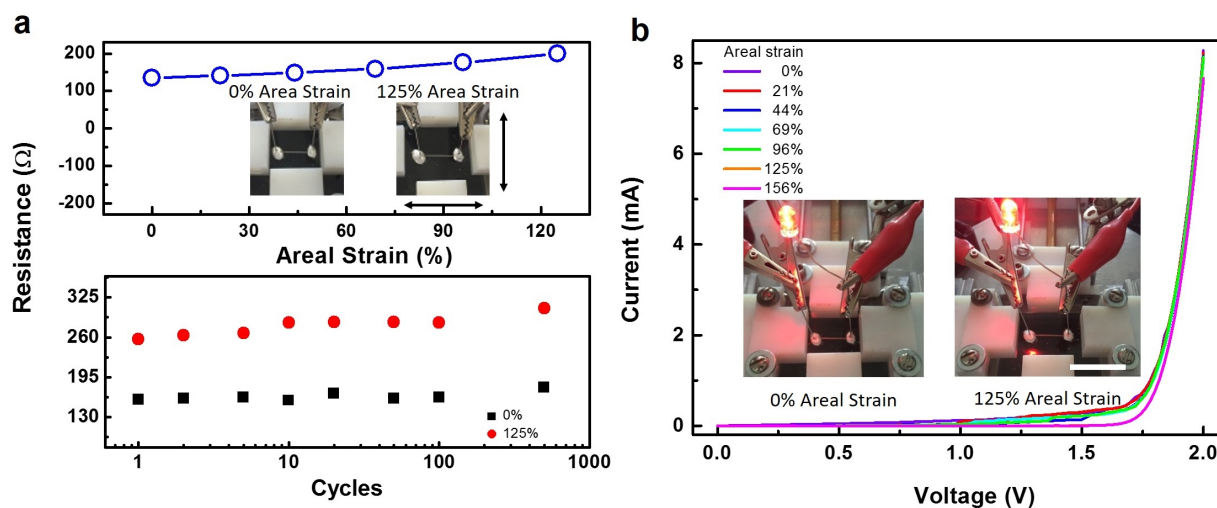


Figure 3.11 Biaxially stretchable conductors based on the printed AgNWs. a) Feature resistance as functions of areal tensile strain (top) and stretching cycles (bottom) for a AgNW feature printed on a biaxially prestretched PDMS substrate. Insets: The sample at relaxed state (left) and being stretched to an areal strain of 125% (right). b) The current-voltage (I-V) curves of the LED-driving circuit using the printed biaxially stretchable AgNW conductor as interconnect with the areal strain varying from 0% to 156%. Insets: Photographs of the circuit while the interconnect is under 0 (left) and 125% (right) areal tensile strain. Scale bar: 2 cm.

The capability of direct printing offers a viable approach of additively pattern AgNWs for stretchable sensor and display applications. Pressure sensing is one of the basic functionalities of human skin and has been a research focus in the electronic skin field for many years [119]. Piezoresistive and piezocapacitive effects are the most widely explored working mechanisms of pressure sensors [120]. Capacitive pressure sensors usually adopt a parallel plate capacitor structure and register changes in capacitance when normal pressure is applied. A high sensitivity and small hysteresis can be obtained by using an elastomer as the dielectric medium [121]. Although AgNWs have been used as electrodes of capacitive pressure sensors in a couple of studies [103], most of them were patterned through shadow masks that are subtractive and not additive [107, 111]. Here, as a proof-of-concept demonstration, we have fabricated a soft capacitive pressure sensor array using the printed AgNWs as electrodes.

Briefly, parallel AgNW lines were first printed on two PDMS films. The AgNW/PDMS films were subsequently laminated in a face-to-face and orthogonal manner with a layer of soft silicone rubber (Ecoflex 0010, Smooth-on) as spacer.

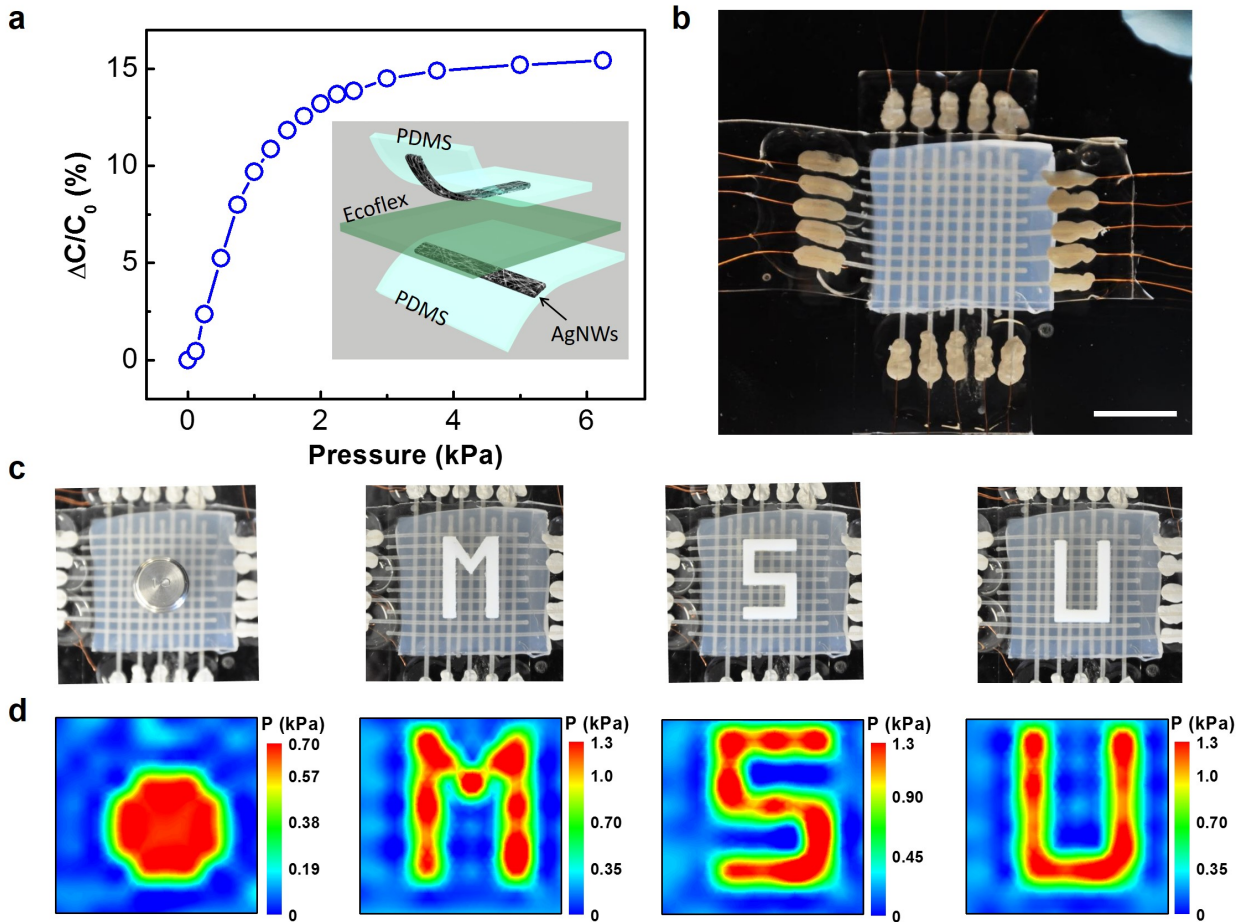


Figure 3.12 Soft capacitive pressure sensor array using the printed AgNW features as stretchable electrodes. a) Relative change in capacitance as a function of applied pressure for an individual pixel. Inset: Structural schematic of the pressure sensor. b) Photograph of a 10×10 pressure sensor array with a line width of $\approx 600 \mu\text{m}$ and a pitch size of $\approx 1600 \mu\text{m}$. Scale bar: 1 cm. c) Photographs of placing different objects on the sensor array to demonstrate its pressure mapping capability. From left to right: a 10 g weight, M-, S-, and U-shaped objects. d) The corresponding 2D pressure contour plot determined from the measured capacitance change and the calibration curve in (a).

As illustrated in the inset of Figure 3.12a, each pixel is formed by a parallel plate capacitor with the AgNW lines and Ecoflex as electrodes and dielectric layer, respectively. Figure 3.12b shows the photograph of a 10×10 pressure sensor array. We first investigated the

capacitive response of a single pixel to external pressure. When the pixel is pressed, the Ecoflex rubber will become thinner and, due to Poisson effect, the electrode area will also get enlarged slightly. Consequently, the pixel capacitance will increase according to equation $C = \varepsilon A/t$, where ε , A , and t are the dielectric constant, overlapping area of the two electrodes, and thickness of Ecoflex, respectively. As shown in Figure 3.12a, the relative change in capacitance ($\Delta C/C_0$) increases proportionally with a slope (sensitivity) of $10.6\% \text{ kPa}^{-1}$ in low-pressure regime and starts saturating after the pressure exceeds $\approx 1.5 \text{ kPa}$. The saturation phenomenon can be attributed to the strain stiffening of the Ecoflex rubber [122]. Our pressure sensor exhibits unambiguous capacitive response within the measured pressure range of $\approx 100 \text{ Pa}$ to 6 kPa which is well below the usual sensing regime ($>10 \text{ kPa}$) of human skin [119]. It should be noted that, a sensitivity of $10.6\% \text{ kPa}^{-1}$ and minimum detectable pressure of $\approx 100 \text{ Pa}$ are very respectable values considering the dielectric layer is not texturized to special microstructures [121]. For practical applications, the applied pressure can be determined reciprocally from the $\Delta C/C_0$ pressure curve shown in Figure 3.12a. Next, we demonstrate the use of the 10×10 pressure sensor array to spatially map the pressure profiles applied by a cylindrical weight and MSU shaped objects. As depicted in Figure 3.12d, the 2D pressure profiles determined from the electrical signal ($\Delta C/C_0$) replicate the shape of all objects with high fidelity, implying the sensor array's potential application as high resolution and ultrasensitive electronic skin. In the future, the line width and interline spacing of the printed AgNW features can be reduced by using nozzles with smaller openings, which could lead to further improved resolution of the sensor array.

Finally, by replacing the Ecoflex 0010 between the two AgNW electrodes with a composite composed of PDMS and EL phosphors, we have demonstrated a printed stretchable EL display. It is well known that EL phosphors, like ZnS doped with transition metals, can emit light under AC voltage stimulation, which was speculated to be caused by electric field induced tunneling through embedded junctions and subsequent radiative recombination [123]. The light intensity of the EL display increases with the magnitude and frequency of the AC

voltage. By changing the type and concentration of dopants, polychrome light emission can be realized. While EL phosphors have been widely used in the form of powder EL cells for back lighting of liquid crystal displays, they are very brittle and thus not suitable for flexible or stretchable display applications. An extensively used strategy to make stretchable materials from brittle inorganic micro-/nanoparticles is to disperse them in a polymer matrix like silicone such that the desired electrical properties of the inorganic particles and the elasticity of silicone are preserved simultaneously [124, 125, 126]. The same strategy has proven to work well for phosphors. In recent years, a couple of groups have reported stretchable EL display/lighting devices based on composites composed of silicone and phosphors [127, 128, 129]. Here, we demonstrated silicone/phosphor composite-based stretchable EL displays in various configurations using our printed AgNWs as electrodes. As shown in Figure 3.13a, the EL device adopts a similar structure with the pressure sensor, with the Ecoflex layer replaced with a PDMS/phosphor composite. The light emission performance of the EL devices was studied systematically. Figure 3.13b presents the light emission spectra of a green EL device under various stimulation conditions. The peaks of the EL spectra center at ≈ 510 nm and show no noticeable changes when the excitation frequency changes from 0.5 to 1 kHz and magnitude changes from 1 to 2 kV. The luminance is plotted as functions of excitation frequency and magnitude in Figure 3.13c,d, respectively. As expected, the luminance increases dramatically as the excitation frequency is increased from 10 Hz to 1 kHz or as the voltage is increased from 300 V to 2 kV. The relation between luminance and excitation voltage can be fit very well using the established equation [123].

$$L = L_0 \times e^{-c/V^{1/2}} \quad (3.1)$$

The devices were then subjected to stretching tests and the results are shown in Figure 3.13e,f. The devices could withstand tensile strains up to 20% for more than 1000 cycles, albeit with noticeable degradation in luminance at 20% strain. The degradation in luminance could be attributed to the gradual loss in conductance of the AgNW electrodes or

the electrical contacts between the electrodes and measurement leads as they get stretched.

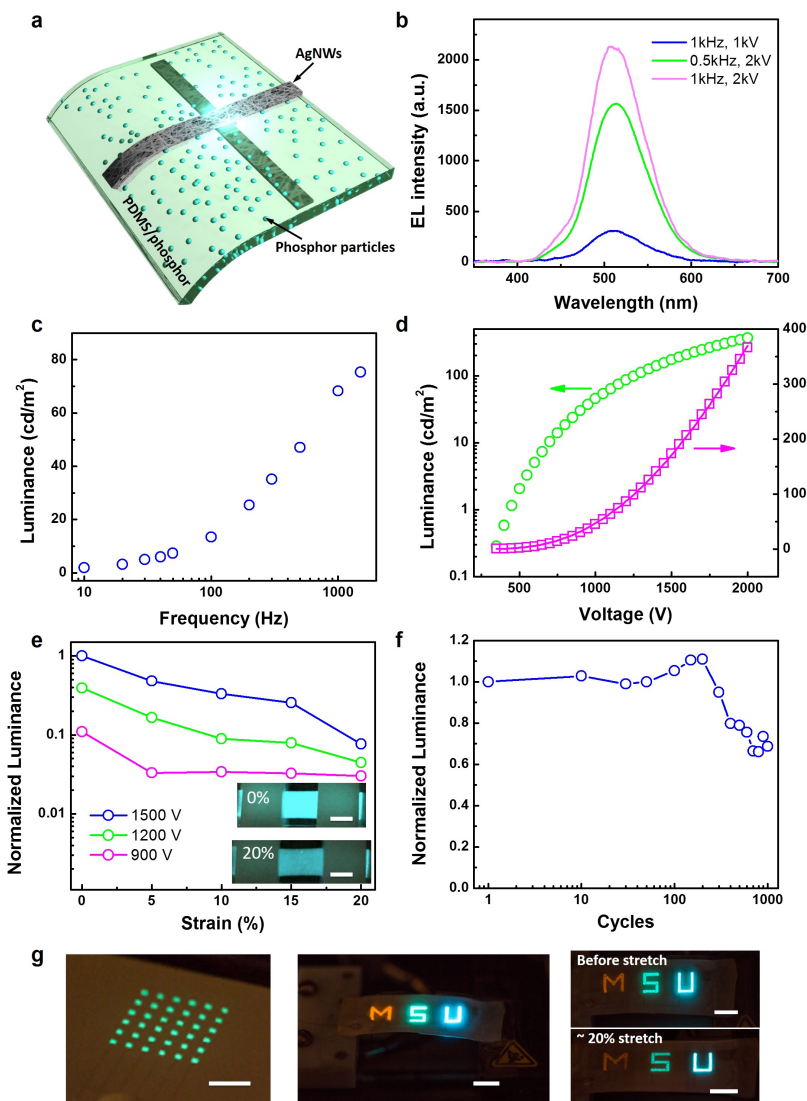


Figure 3.13 Stretchable electroluminescent (EL) displays using the printed AgNWs as electrodes. (a) Schematic of the device structure. (b) EL spectra of the device made of green phosphors under different stimulation conditions. (c,d) EL intensity of the device made of green phosphors as functions of frequency (c, measured at 1 kV) and magnitude (d, measured at 500 Hz) of the AC voltage. (e) Normalized EL intensity plotted as a function of tensile strain when measured under AC voltage with different magnitudes and a frequency of 1 kHz. Inset: Photographs of a device made of green phosphors under 0 and 20% tensile strains. Scale bars: 5 mm. (f) Normalized EL intensity versus stretching cycles measured under AC voltage with a magnitude of 1.5 kV and a frequency of 1 kHz. (g) Photographs of a 6×6 EL display array made of green phosphors (left), an MSU display pattern using orange, green, and blue phosphors for M, S, and U, respectively (middle), and the MSU-shaped display under 0 and 20% tensile strains (right). Scale bars: 1 cm.

The stability in light emission performance under tensile strain can be further improved by using longer nanowires or using more robust conductive glue as the electrical contacts during the electrical measurements. Figure 3.13g presents EL display devices in different configurations that were enabled by the direct printing of AgNWs. The demonstrations include a 6×6 green display array (left) and an MSU shaped polychrome (orange, green, and blue) display with different types of phosphors patterned in one composite film. The polychrome display worked very well under a tensile strain of $\approx 20\%$, albeit with some degradation in light intensity.

3.4 Summary

In summary, we have developed a direct printing process for additively pattern AgNWs with length up to $\approx 40 \mu\text{m}$ on various substrates. Well-defined and uniform AgNW features could be obtained by optimizing the printing conditions including nozzle size, ink formulation, surface energy, substrate temperature, and printing speed. Systematic characterizations were performed to investigate the electrical and electromechanical properties of the printed features with different nanowire lengths. By printing the AgNWs on a biaxially prestretched PDMS substrate, we have realized a stretchable conductor that could maintain stable conductance under an areal strain of up to 156% (256% of its original area). Additionally, using the printed parallel AgNWs as electrodes, we have demonstrated an ultrasensitive capacitive pressure sensor array and an EL display on mechanically compliant substrates, implying the great potential of this unique additive patterning method in wearable electronics applications. Furthermore, the same strategy can be adapted to other material platforms like semiconducting nanowires, which may offer a cost-effective entry to various nanowire-based mechanically compliant sensory and optoelectronic systems.

CHAPTER 4

FULLY PRINTED STRETCHABLE THIN FILM TRANSISTORS AND INTEGRATED LOGIC CIRCUITS

This chapter reports intrinsically stretchable thin-film transistors (TFTs) and integrated logic circuits directly printed on elastomeric polydimethylsiloxane (PDMS) substrates. The printed devices utilize carbon nanotubes and a type of hybrid gate dielectric comprising PDMS and barium titanate (BaTiO_3) nanoparticles. The BaTiO_3 /PDMS composite simultaneously provides high dielectric constant, superior stretchability, low leakage, as well as good printability and compatibility with the elastomeric substrate. Both TFTs and logic circuits can be stretched beyond 50% strain along either channel length or channel width directions for thousands of cycles while showing no significant degradation in electrical performance. This work may offer an entry into more sophisticated stretchable electronic systems with monolithically integrated sensors, actuators, and displays, fabricated by scalable and low-cost methods for real life applications.

4.1 Introduction

Stretchable electronic systems built on soft substrates offer more conformal surface coverage and better durability than flexible electronics and have generated significant research interest recently for potential applications in wearable/implantable health monitoring and diagnostic devices [130, 131, 132], electronic skin for prosthesis or soft robotics [133, 134], stretchable displays [135, 136] and more. Nevertheless, the required large area and low-cost fabrication of high-performance intrinsically stretchable electronic devices have remained extremely difficult. There are three key technical challenges faced by large-area stretchable electronics: (1) high-performance and robust stretchable electronic material platforms; (2) scalable and low-cost fabrication processes; and (3) integration of stand-alone stretchable

devices into functional systems. Stretchable electronics are generally realized through two approaches, namely, structural stretchability enabled by the use of buckling or serpentine structures in stiff materials or intrinsic stretchability endowed by new elastomeric or composite materials [137]. The first structural engineering approach utilizes high-performance rigid semiconductors (e.g., silicon or III-V materials) and conventional clean-room-based microfabrication processes, which have led to the demonstration of numerous types of sophisticated stretchable electronic systems [130, 138, 139]. Despite the great success, this first approach may not be suitable for certain large-area applications due to the high manufacturing cost. Moreover, only a fraction of the area is actually occupied by active devices, and the rest of the area is filled with voids and thus wasted. In this regard, intrinsically stretchable materials are of particular interest because they are usually solution processable and even printable and, thus, potentially suitable for large-area and cost-effective manufacturing [140, 141]. A number of new materials have been under exploration, among which are silver nanowires [142], carbon nanotubes [143, 144, 145], graphene [146], conductive polymers [147], and organic semiconductors [148]. Intrinsically stretchable thin-film transistors (TFTs) have been demonstrated recently by a variety of approaches based on the above materials [149, 150, 151, 152, 153, 154, 155]. However, printing has never been used as the fabrication process, and all previous reports were only limited to proof-of-concept level demonstrations of individual transistors.

4.2 Fabrication Process and Measurement Setup

4.2.1 Materials

Polydimethylsiloxane (Sylgard 184, 10:1) slabs with a thickness of ~ 0.5 mm were prepared as the stretchable substrates. High-purity semiconducting carbon nanotubes (IsoNanotubes-S 98%, 0.01 mg/mL, NanoIntegris) were used as the channel semiconductors. Highly functionalized unsorted carbon nanotubes (P3-SWNT, Carbon Solutions, Inc.) were used for

the source, drain, and gate electrodes of the TFTs. Barium titanate nanoparticles (BaTiO_3 , 99%, 50 nm, cubic), Triton X-100 (laboratory grade) and poly-L-lysine (0.1% w/v in water), and 4-methyl-2-pentanone (99%) were purchased from US Research Nanomaterials, Sigma-Aldrich, and Alfa Aesar, respectively.

4.2.2 Ink Formulations

To prepare the inks for printed electrodes, 5 mg of P3-SWNT carbon nanotube powder was dissolved in DI water by successive bath sonication (Crest CP360D, power level 9, 3 h) and probe sonication (VirTis VirSonic 100, 10 W, 5 min) followed by ultracentrifugation (13000 rpm, 1 h) to remove remaining agglomerations. Triton X-100 (0.1% wt) was finally added into the solution to facilitate the printing on PDMS. The ink for hybrid gate dielectric was prepared by first mixing PDMS (base only), BaTiO_3 nanoparticles, and 4-methyl-2-pentanone followed by magnetic stirring for 30 min. The mixture was then subjected to successive bath sonication (power level 9, 4 h) and probe sonication (15 W, 10 min) to break the large aggregations of BaTiO_3 . The weights of PDMS and 4-methyl-2-pentanone were fixed at 1 and 4 g, respectively, while the weight of BaTiO_3 was varied from 0.5 to 2 g. Lastly, 0.3 g of curing agent was added to the dispersion before printing.

4.2.3 Device Fabrication

The fabrication steps used for TFTs and integrated logic circuits are detailed below, as shown in Figure 4.1:

1. Treat the surface of polydimethylsiloxane (PDMS) substrates (Sylgard 184, 10:1, ~ 0.5 mm thick) with O_2 plasma (30 W, 500 mTorr, 3~5 sec). This step renders the PDMS surface hydrophilic due to the formation of a very thin layer of silica.
2. Functionalize the treated PDMS surface with amine-group by immersing it in poly-L-lysine (0.1% w/v in water, Sigma-Aldrich) for 10 min followed by rinsing

with deionized (DI) water and blowing dry with N₂.

3. Semiconducting single-walled carbon nanotubes (sSWCNT)(0.01 mg/ml, 98% semiconducting enriched, NanoIntegris) are deposited onto the functionalized PDMS surface by dropcasting for 30 min followed by rinsing with DI water and blowing dry with N₂.

4. The channels of the TFTs (width $\sim 2500 \mu\text{m}$, length $\sim 150 \mu\text{m}$) are defined by printing unsorted carbon nanotube (CNT) solution (0.5 mg/ml, with 0.1 mg/ml TritonX-100) for 40 \sim 50 layers as the source and drain electrodes.

5. S1813 (Microchem) photoresist is printed onto the channel as a protective layer. The semiconducting carbon nanotubes out of the channel region are subsequently etched away by O₂ plasma (60 W, 500 mTorr, 1 min). (Step 5 is skipped for devices with semiconducting carbon nanotubes printed in the channel)

6. BaTiO₃/PDMS ink is printed as the gate dielectric followed by curing at 150 °C for 20 min.

7. The surface of the gate dielectric is rendered hydrophilic by O₂ plasma treatment (30 W, 500 mTorr, 2 sec).

8. Unsorted carbon nanotube solution (same as step 4) are printed onto the gate dielectric for 20 \sim 30 layers as the top gate electrode.

Steps 1-8 conclude the fabrication of the stretchable TFTs. For the integrated logic circuits, several additional steps are added:

9. More unsorted carbon nanotube solution is printed for 40 \sim 50 layers as the interconnection in the logic circuits and to define the channel of load resistor.

10. Carbon nanotubes are printed in the channel of the load resistor layer by layer until an optimal resistance value is achieved.

11. Finally, before stretching tests, PDMS is printed to cover the whole carbon nanotube features as an encapsulation layer to prevent the devices from catastrophic cracking

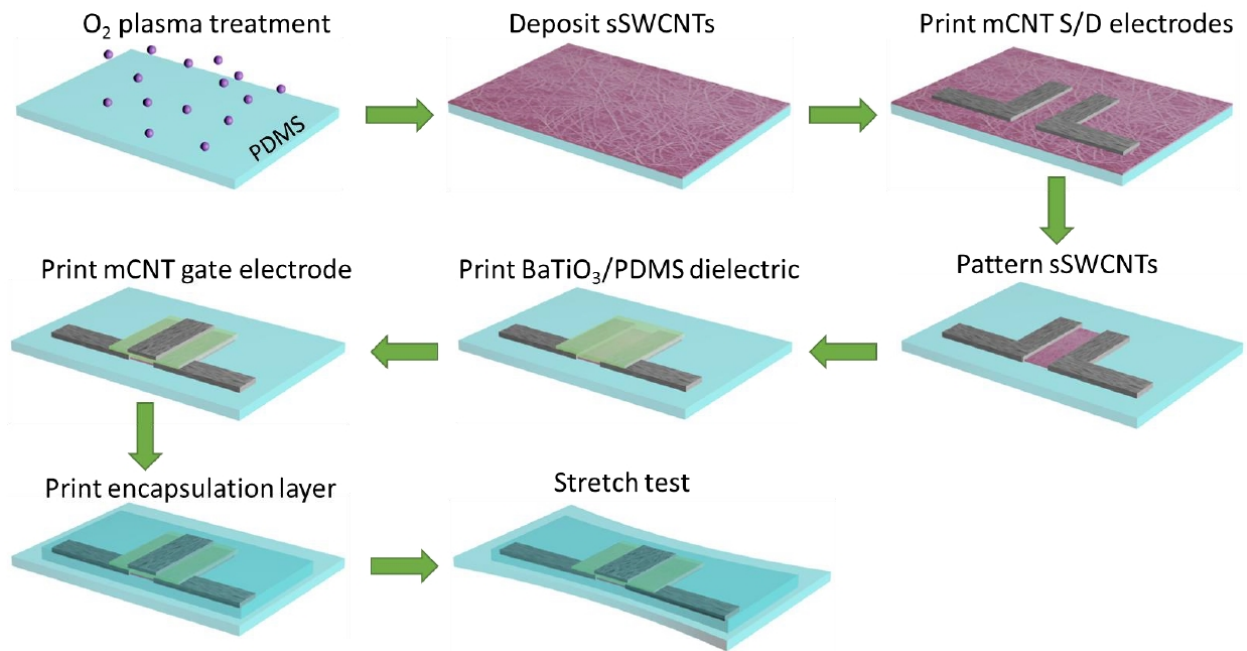


Figure 4.1 Schematic diagrams illustrating the fabrication processes of printed stretchable TFTs.

4.2.4 Characterizations

The electrical characteristics of TFTs and logic gates were measured by an Agilent B1500A semiconductor parameter analyzer. Resistance of the printed CNT electrodes was measured by a Keithley 2100 multimeter controlled by a LabView program. The gate dielectric layer material was characterized by the CV module (B1520A) of the Agilent B1500A analyzer. Stretching tests were performed automatically with a syringe pump. Scanning electron micrographs, atomic force micrographs, and optical micrographs were captured with a Hitachi S-4700II field emission scanning electron microscope (FESEM), a Dimension 3100 atomic force microscope (AFM), and an Olympus BX51 optical microscope, respectively. All measurements were conducted under ambient conditions.

4.3 Results and Discussion

In this work, we take one significant step forward by demonstrating fully printed stretchable integrated circuits on PDMS substrates. Unsorted carbon nanotubes (CNTs) and high-purity semiconducting single-walled carbon nanotubes (sSWCNTs) are used as the source/drain/gate electrodes and channel semiconductor, respectively.

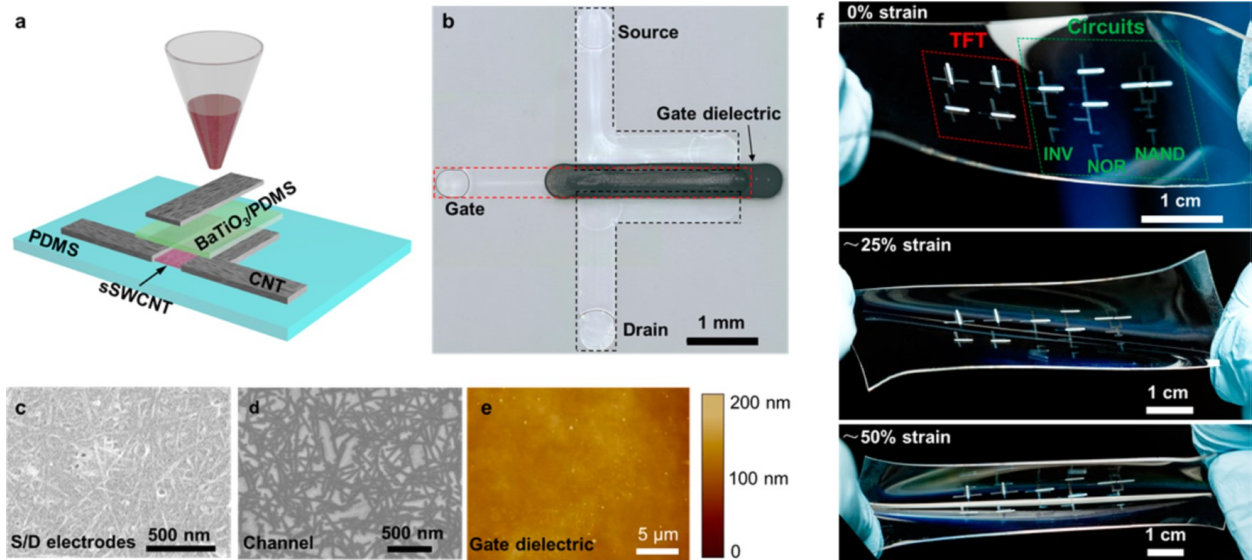


Figure 4.2 Fully printed and intrinsically stretchable carbon nanotube thin-film transistors (TFTs) and integrated logic circuits. (a) Schematic illustrating the structure of a printed stretchable TFT. Unsorted carbon nanotubes, high-purity semiconducting single-walled carbon nanotubes (sSWCNT), and BaTiO₃/PDMS composite are used as the source/drain/gate electrodes, channel semiconductor, and gate dielectric, respectively. (b) Optical micrograph of a TFT printed on a PDMS substrate. (c-e) Scanning electron micrograph of the carbon nanotube network in the source/drain electrodes (c) and channel (d) and atomic force micrograph of the BaTiO₃/PDMS gate dielectric (e). (f) Optical photograph of a representative sample consisting of four TFTs, a resistive load inverter, and a resistive load two-input NOR gate and NAND gate, at tensile strains of 0% (top), ~ 25% (middle), and ~50% (bottom).

As shown in the schematic (Figure 4.2a) and optical micrograph (Figure 4.2b), our stretchable TFTs were fabricated using an all-printing process and adopt a top-contact, top-gated device structure (refer to the Fabrication Process and Measurement setup section for more details). Compared with silver or gold nanoparticle inks, the most widely used conducting materials in printed electronics, CNT electrodes provide better electrodesemi-

conductor contacts due to the perfect structural and electronic consistency between carbon nanotubes [156]. In addition, carbon nanotubes are a perfect choice for stretchable electrodes because of their ultrahigh aspect ratio and the formation of highly deformable mesh structures in macroscale assemblies [143]. Parts c and d of Figure 4.2 reveal the dense unsorted CNT network in the source/drain electrodes and the monolayer sSWCNT network in the TFT channel region. The gate dielectric is a composite consisting of PDMS, the same material as the stretchable substrate, and BaTiO₃ nanoparticles, a ceramic material with a relative permittivity of up to ~ 200 . This hybrid dielectric material combines the best of both worlds; i.e., the high permittivity of BaTiO₃ and superior stretchability of PDMS, as shown below, deliver excellent electrical performance, mechanical robustness, and compatibility with the substrate. The atomic force micrograph (AFM) of the printed BaTiO₃/PDMS is shown in Figure 4.2e. Figure 4.2f presents photographs of a representative sample with printed TFTs and integrated logic circuits (inverter, NOR, and NAND gates) in the relaxed state and under tensile strain of $\sim 25\%$ or $\sim 50\%$.

The unsorted carbon nanotubes used for the electrodes and interconnections are purified with nitric acid and contain 1.0-3.0 atomic percent carboxylic acid [157], and thus, they can be well dispersed in pure water without the assistance of any surfactant (Figure 4.3a). In order to investigate the performance of print CNTs when used as Source/Drain electrode, we have fabricated two identical devices on Si/SiO₂ substrates with printed CNTs and thermally evaporated metal electrode as the source/drain electrodes, respectively. The device structure is illustrated in Figure 4.3b and the microscope images of the devices are shown in the insert figure of Figure 4.3e and f. For the device with printed CNTs as the electrodes, we have taken the SEM image for both of the CNT electrodes region and CNT channel region, which are both dense and uniform, shown in Figure 4.3c and d, respectively. As shown in Figure 4.3e and f, The device with printed carbon nanotube source/drain electrodes (Figure 4.3f) exhibits comparable electrical characteristics with that using evaporated Ti/Au as source/drain electrodes (Figure 4.3e) in terms of both field effect mobility ($16 \text{ cm}^{-2}\text{V}^{-1}\text{s}^{-1}$

vs. $17.7 \text{ cm}^{-2}\text{V}^{-1}\text{s}^{-1}$) and on/off current ratio (700 vs. 177). The low drain bias output curves of the device with carbon nanotube electrodes (Figure 4.3g) exhibit very good linearity, indicating negligible Schottky barrier at the CNTs/sSWCNTs interface.

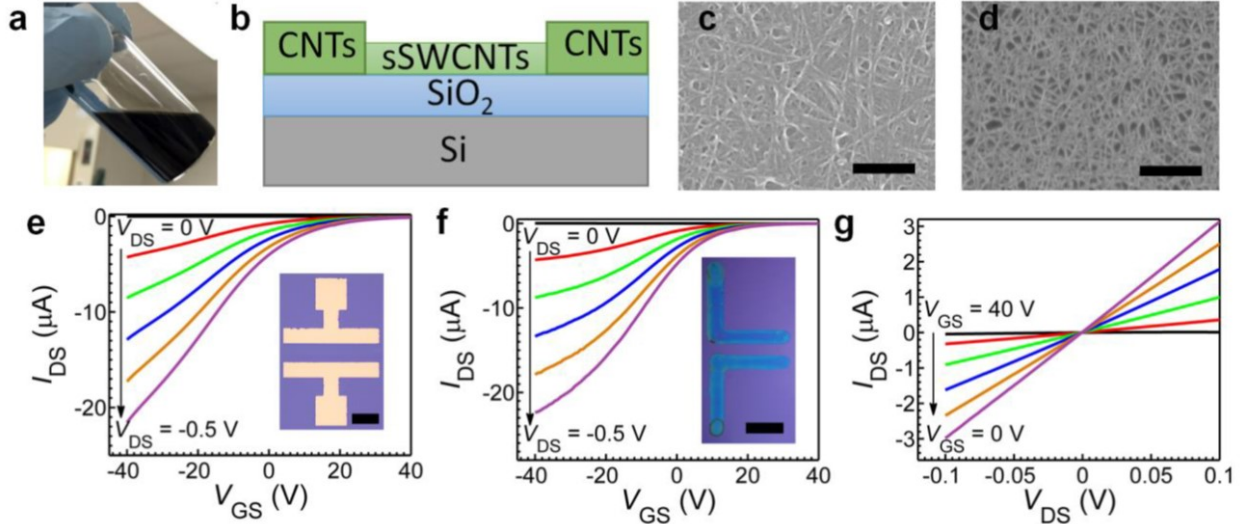


Figure 4.3 Fully-printed all-CNT back-gated TFT on Si/SiO₂ substrate. a, Photograph of the unsorted carbon nanotube ink. b, Schematic of the back gated TFT printed on Si with the unsorted carbon nanotubes as source/drain electrodes. c,d, Scanning electron microscopy (SEM) images showing the carbon nanotube networks in the source/drain electrodes (c) and channel (d). Scale bars in c and d represent 200 nm and 1 μm , respectively. e,f, Representative transfer curves of the back-gated TFTs with evaporated Ti/Au (e) and printed CNT (f) as source/drain electrodes for V_{DS} from 0 to -0.5 V in -0.1 V steps. Insets of e and f show the micrographs of the corresponding TFTs. Scale bars represent 300 μm and 1000 μm , respectively. g, Output curves of the TFT with printed CNT as source/drain electrodes at low drain bias. V_{GS} varies from 0 V to 40 V in 10 V step.

The device shown in Figure 4.3f is printed on Si/SiO₂ substrates. However, Directly printing aqueous solution on PDMS surface is very difficult because of the high hydrophobicity of PDMS. Although PDMS surface can be rendered hydrophilic by O₂ plasma or UV ozone treatment, it recovers the hydrophobicity very quickly, especially at high temperatures [158]. We solved this challenging problem by adding a small amount of Triton X-100 to lower the surface tension of water. In order to investigate the influence of Triton X-100 on the wetting behavior of water on PDMS, we treated PDMS surface with O₂ plasma at a power of 30 W for 3, 6 and 10 sec, followed by heating the PDMS at 100 °C for 1 hour. Contact

angles of water with different concentrations of Triton X-100 on the treated PDMS were measured before and after heating. The results are presented in Figure 4.4a. Pure water exhibit contact angles of $\sim 110^\circ$ and $\sim 40^\circ$ on pristine PDMS surface and PDMS treated with O_2 plasma at 30 W for 10 sec, respectively. Adding 0.01% or 0.1% Triton X-100 drastically decreases the contact angles, as shown in Figure 4.4b.

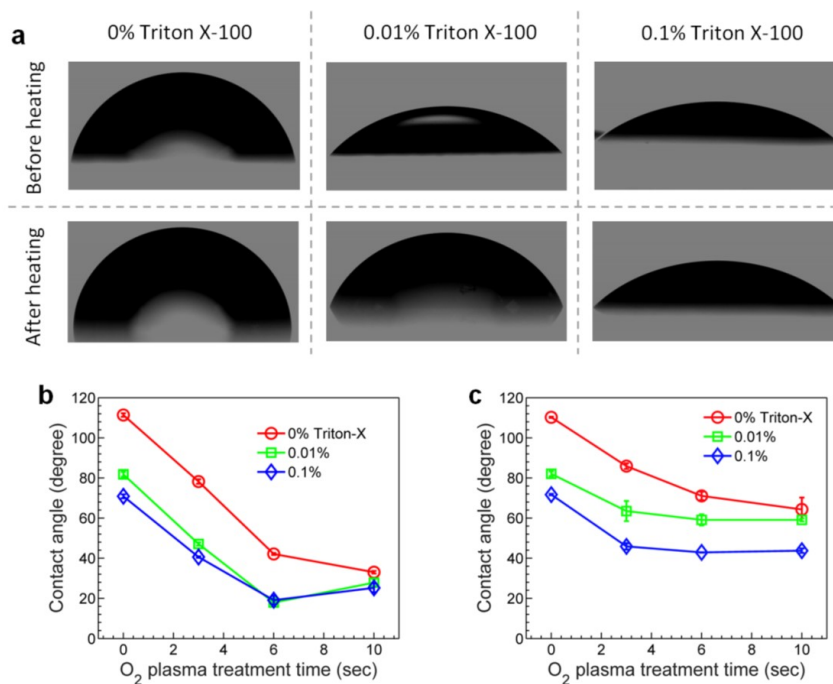


Figure 4.4 Contact angle of water with and without Triton X-100 on PDMS treated with O_2 plasma. a, Optical images of water droplets with different concentration of Triton X-100 on PDMS (O_2 plasma treatment: 30 W, 3 sec) before and after heating at $100^\circ C$ for 1 hour. b,c, Contact angle of water with different concentrations of Triton X-100 plotted as a function of O_2 plasma treatment time before (b) and after (c) heating at $100^\circ C$ for 1 hour.

However, after the PDMS is heated at $110^\circ C$ for 1 hour, the surface hydrophobicity is recovered, as manifested by the high contact angles of pure water on all PDMS surfaces (Figure 4.4c). In contrast, the contact angles of water with 0.01% and 0.1% Triton X-100 on O_2 plasma treated PDMS, regardless of the treatment durations, settle at $\sim 60^\circ$ and $\sim 40^\circ$, respectively. The above results indicate that a small amount of Triton X-100, combined with mild O_2 plasma treatment, can significantly improve the wetting of water on PDMS surface, even at elevated temperatures. Furthermore, it was found that the CNT solution

with 0.1% Triton X-100 yield better printing results than that with 0.01% Triton X-100, which is in agreement with the literature results that a contact angle of below 50° is desired for ink-jet printing [159]. Further increasing the Triton concentration beyond 0.1% will result in very low contact angles and may produce uncontrollable ink bleeding. Therefore, inks with 0.1% Triton X-100 were used for all of our printed devices. It should also be pointed out that while the Triton X-100 is a widely used surfactant, the main purpose of adding it here is for tuning the surface tension of the ink instead of facilitating the dispersion of carbon nanotubes. As described previously, the unsorted carbon nanotubes used in this work contain 1.0-3.0 atomic percent carboxylic acid groups and can be dispersed in pure water directly without any surfactant. In fact, 0.1% Triton X-100 is significantly lower than the concentration needed to disperse CNTs without functional groups [160]. Lastly, because the concentration of Triton X-100 used in our inks is very low, the electrical properties of the CNTs are not affected noticeably.

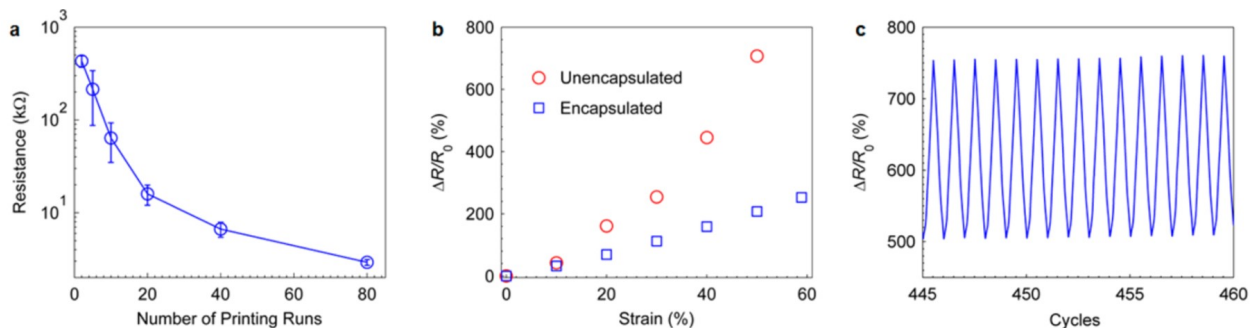


Figure 4.5 Characteristics of the printed CNT electrodes. (a) Resistance of CNT features (length ~ 6 mm, width ~ 0.5 mm) printed on PDMS as a function of the number of printing runs. The error bars are standard deviations obtained from more than five samples. (b) Relative change in resistance ($\Delta R/R_0$) as functions of tensile strain for CNT features with (blue squares) and without (red circles) PDMS encapsulation layer. (c) $\Delta R/R_0$ of a printed CNT feature (with PDMS encapsulation) when the sample is being repeatedly stretched between 0% and 60% strain.

Since the CNT solution has a quite low concentration (<0.5 mg/mL), multiple printing runs are required to obtain a conductive feature. Figure 4.5a presents the resistance of the printed CNT features after various numbers of printing runs. The resistance drops

dramatically during the first ~ 20 runs and reaches several $k\Omega$ after ~ 40 runs, which is sufficiently low to work as the source/drain electrodes for CNT TFTs (channel resistance is greater than hundreds of $k\Omega$). Extensive studies have shown that, due to the one-dimensional attributes of CNTs and the mesh structure of their macroscale assemblies, CNT thin films exhibit excellent stretchability [143]. Additionally, the increase in resistance under tensile strain can be further alleviated by a polymeric encapsulation layer [161]. Comparing the pristine CNT features printed on PDMS with those encapsulated by an additional PDMS layer, one can clearly see that the encapsulated CNT film exhibits better stretchability, with a change in resistance of $\sim 200\%$ under 60% tensile strain (Figure 4.5b). The critical role of PDMS encapsulant in improving the stretchability of the CNT film can be attributed to the greatly mitigated stress concentration in CNT networks by the surrounding cross-linked PDMS molecules, which prevents the occurrence of macroscale cracks that are responsible for a more pronounced increase in resistance of the unencapsulated features. After hundreds of stretching cycles with a maximum strain of 60%, the resistance of an encapsulated CNT features settles at around 5 times of its original value (Figure 4.5c).

One of the greatest challenges in realizing intrinsically stretchable TFTs is the high-performance stretchable gate dielectric material that can simultaneously offer high gating strength, good mechanical robustness, and solution processability [143, 149]. Conventional inorganic gate dielectrics like SiO_2 and Al_2O_3 are rigid and brittle and, thus, not suitable for stretchable devices unless engineered to a wrinkled configuration by sophisticated approaches [149]. In addition, they usually require vacuum-based deposition processes (evaporation or atomic layer deposition), which are costly and not suitable for low-cost applications or green manufacturing. A number of alternative material platforms, like polymeric dielectrics [151, 155], ion gels [150, 153, 154], and hybrid dielectrics [162], have been proposed. Solution-processed polymeric dielectrics have been widely used for both flexible and stretchable TFTs, but most of them exhibit rather low dielectric constants and gating strength, which leads to high operating gate voltages. Ionic gels (block copolymer networks swollen by ionic liquids)

have also attracted extensive research interest as stretchable gate dielectric materials due to their gigantic capacitance and superior stretchability [163]. The practical applications of ion gels are, however, greatly hampered by their instability in ambient conditions, difficulties in suppressing gate leakage current, and possible electrochemical reactions at the dielectric/conductor or dielectric/semiconductor interface. In contrast, hybrid dielectrics consisting of inorganic dielectric nanofillers dispersed in a polymer matrix show the best overall performance by combining the high permittivity of inorganic dielectrics with the solution processability and mechanical robustness of polymers. A large variety of inorganic high-k dielectric and polymer composites have been explored [162]. For instance, several groups have demonstrated that the BaTiO₃/PMMA composites show excellent performance as the gate dielectric for printed flexible CNT TFTs [164, 165, 166]. Despite the progress, almost all studies focus on hybrid dielectrics that are only flexible and cannot survive large tensile deformations.

Here in this work, we have developed a highly stretchable hybrid gate dielectric material by blending cubic phase BaTiO₃ nanoparticles (particle size \sim 50 nm) and PDMS (see the details in the Section 4.2). And in order to mix the BaTiO₃ nanoparticles and PDMS together, a proper solvent should be carefully chosen. An ideal solvent should not only be able to dissolve the active materials but also have appropriate values of vapor pressure and surface tension that are suitable for printing. Hexane is usually used for dissolving PDMS [167, 168]. The high vapor pressure of hexane, however, means it evaporates too fast and makes it a bad choice for printing PDMS. Here, we choose 4-methyl-2-pentanone as the solvent for PDMS. As shown in Table 4.1, the solubility parameter of 4-methyl-2-pentanone is close to that of PDMS, making it a good solvent for PDMS. In addition, the vapor pressure is close to that of water and thereby very suitable for printing. Finally, the surface tension is 23.6 mN/m, which is about 1/3 of water and ensures good wetting on PDMS surface. As a result, 4-methyl-2-pentanone is ideal for dissolving PDMS for printing process.

Systematic electrical characterizations (Figure 4.6 and 4.7) reveal that the BaTiO₃/PDMS

Table 4.1 Physical properties of the solvents for PDMS

	<i>Vapor pressure at 25°</i> (<i>mmHg</i>)	<i>Surface tension</i> (<i>mN/m</i>)	<i>Solubility parameter</i> (<i>cal^{1/2}cm^{-3/2}</i>)
<i>H₂O</i>	17	72	23.5
<i>Hexane</i>	150	18.43	7.24
<i>C₆H₁₂O</i>	19.9	23.6	8.4
<i>PDMS</i>			9.3

hybrid dielectric exhibit superior performance in almost all aspects, including dielectric constant, high frequency characteristics, leakage current, and stretchability. Before mixing the BaTiO₃ and PDMS, we have calculated the volume content of BaTiO₃ nanoparticles using the following equation:

$$f = \frac{m_{BaTiO_3}/\rho_{BaTiO_3}}{m_{BaTiO_3}/\rho_{BaTiO_3} + m_{PDMS}/\rho_{PDMS}} \quad (4.1)$$

where m represents the mass and ρ represents the density. Based on the reported density values of BaTiO₃ (5.85 g/cm³) and PDMS (0.965 g/cm³), the volume content of BaTiO₃ is calculated to be 0.08, 0.148 and 0.258 for composites with weight ratios (PDMS:BaTiO₃) of 1:0.5, 1:1, and 1:2, respectively. The solutions with various BaTiO₃ contents are spin coated on Si or glass to fabricate parallel capacitors and used to characterize the dielectric constant of the BaTiO₃/PDMS films. As shown in Figure 4.6a, the relative permittivity increases dramatically and reaches ~ 9 at a BaTiO₃ volume content of $\sim 26\%$. Inks with higher BaTiO₃ contents are very difficult to be dispersed evenly. The relative permittivity versus BaTiO₃ volume content can be fitted very well by the well-known Lichteneckers equation 4.2 that is widely used to describe composite dielectric systems with spherical fillers [169]

$$\ln(\varepsilon_{cr}) = f \times \ln(\varepsilon_{fr}) + (1 - f) \times \ln(\varepsilon_{mr}) \quad (4.2)$$

where ε_{cr} , ε_{fr} , ε_{mr} are the relative permittivities of the composite, nanofiller and polymer matrix, respectively. And f is the volume content of the nanofiller. The fitting parameters obtained here, $\varepsilon_{fr} \sim 307.9$, $\varepsilon_{mr} \sim 2.6$, are close to the relative permittivity of cubic phase BaTiO₃ and PDMS, respectively. The results here imply that hybridization is an effective

approach to greatly enhance the dielectric constant of polymers while maintaining their desirable mechanical property and solution processability.

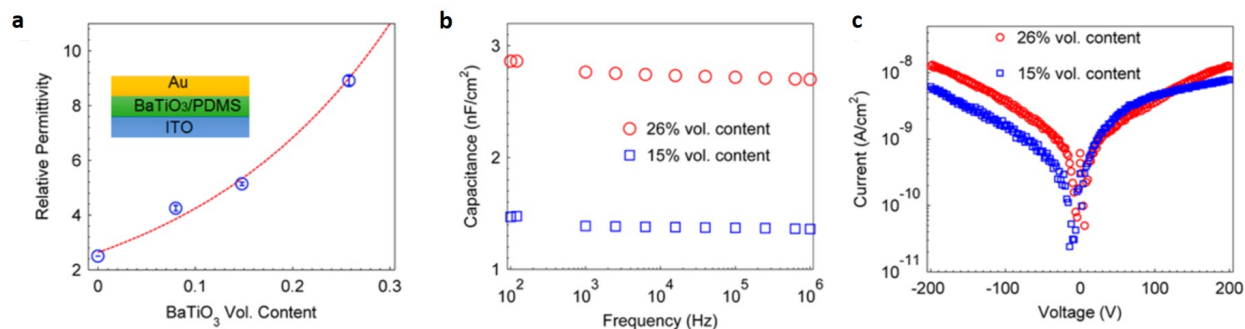


Figure 4.6 Characteristics of the BaTiO₃/PDMS gate dielectric. (a) Relative permittivity of the composite gate dielectric as a function of the volume content of BaTiO₃ nanoparticles measured from parallel plate capacitors fabricated on glass substrate. The error bars are standard deviations obtained from more than five samples. Inset: cross-sectional schematic of the parallel plate capacitor. (b) Capacitance measured at various frequencies for the composite gate dielectrics with BaTiO₃ volume content of 15% (blue squares) and 26% (red circles), respectively. (c) Leakage current density of the composite gate dielectric with a thickness of around 2 μm .

The gigantic capacitance in ionic gel dielectric originates from the establishment of electrical double layers, which relies on the migration of mobile ions in an electric field and is very slow [163]. In contrast, our BaTiO₃/PDMS composite only undergoes dielectric polarization when placed in an electric field and thus exhibits significantly better high frequency performance. Figure 4.6b shows the capacitance-frequency characteristics of parallel plate capacitors made with the BaTiO₃/PDMS dielectrics with $\sim 15\%$ or $\sim 26\%$ BaTiO₃ by volume. As expected, the capacitance is virtually independent of frequency in the range of 100 Hz-1 MHz. We also characterized the leakage current density of our BaTiO₃/PDMS hybrid dielectric using the parallel plate capacitor with a dielectric layer thickness of $\sim 2 \mu\text{m}$. As shown in Figure 4.6c, regardless of the volume content of BaTiO₃, the leakage current density remains below 10 nA/cm² under a voltage of 200 V (electric field of $\sim 1 \text{ MV/cm}$). For a TFT with a channel footprint of $2000 \times 200 \mu\text{m}$, such leakage current density corresponds to a gate leakage current of $\sim 40 \text{ pA}$. The extremely low leakage current implies that the BaTiO₃

nanoparticles have very good compatibility with the PDMS matrix and the dielectric layer is free of pinholes.

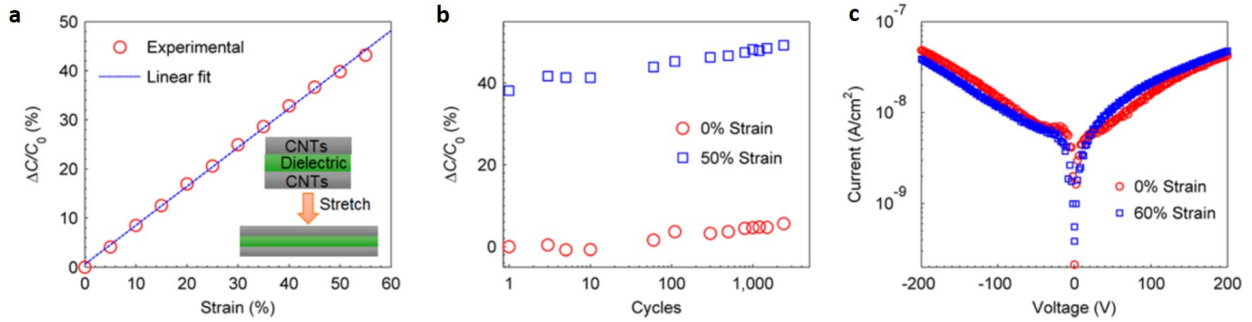


Figure 4.7 (a) Relative change in capacitance ($\Delta C/C_0$) as a function of tensile strain measured from a parallel plate capacitor printed on PDMS. Inset: cross-sectional schematics of the capacitor at relaxed state and stretched state. (b) $\Delta C/C_0$ at 0% (red circles) and 50% (blue squares) strains measured during repeated stretching tests for more than 2000 cycles. (c) Leakage current density of the composite gate dielectric measured at 0% (red circles) and 60% (blue squares) strains.

As discussed above, one of the most intriguing merits of hybrid dielectrics is that they inherit the mechanical properties of polymers [162], which is manifested by the stretching tests on the parallel plate capacitors fabricated on PDMS substrates. Unsorted carbon nanotubes were printed as the top and bottom electrodes of the capacitors (see Section 4.2 for fabrication details). The inset of Figure 4.7a illustrates the device structure and its geometric variations under tensile strains. When the capacitor is subjected to tensile strain, it will extend along the stretching direction (l direction) and shrink along the other two perpendicular directions (w and t directions) due to the Poisson effect. The capacitance at zero strain can be written as

$$C_0 = \varepsilon_{zero} \frac{l_0 w_0}{t_0} \quad (4.3)$$

and The capacitance under tensile stretch can be written as

$$C = \varepsilon \frac{(\lambda_1 l_0)(\lambda_2 w_0)}{\lambda_3 t_0} \quad (4.4)$$

where ε_{zero} represents the permittivity of the dielectric at zero strain and ε is the permittivity under strain. Here, the extending ratio along the stretching direction, λ_1 , equals to $1 + \epsilon$,

where ϵ is the tensile strain. For an isotropic material like PDMS, the compression ratios along the other two directions, λ_2 and λ_3 should have the same value. Given that the permittivity is independent of tensile strains, the capacitance under tensile strain can be written as $C = (1 + \epsilon)C_0$, so that the relative change in capacitance is $\Delta C/C_0 = \epsilon$. In other words, the relative change in capacitance is linear to the tensile strain with a slope of 1 [161]. The experimental data of $\Delta C/C_0$ versus tensile strains for a parallel plate capacitor using BaTiO₃/PDMS dielectric (Figure 4.7a) can be fitted very well by a linear function with a slope of ~ 0.8 . The deviation from the theoretical slope of 1 could be explained by the possible anisotropy induced by the presence of BaTiO₃ nanoparticles in PDMS. In addition, the permittivity of the composites might be slightly dependent on tensile strains, which deserves further study. The increase in capacitance upon stretching leads to a stronger gating strength and thus, as will be discussed below, benefits the performance of the stretchable CNT TFTs.

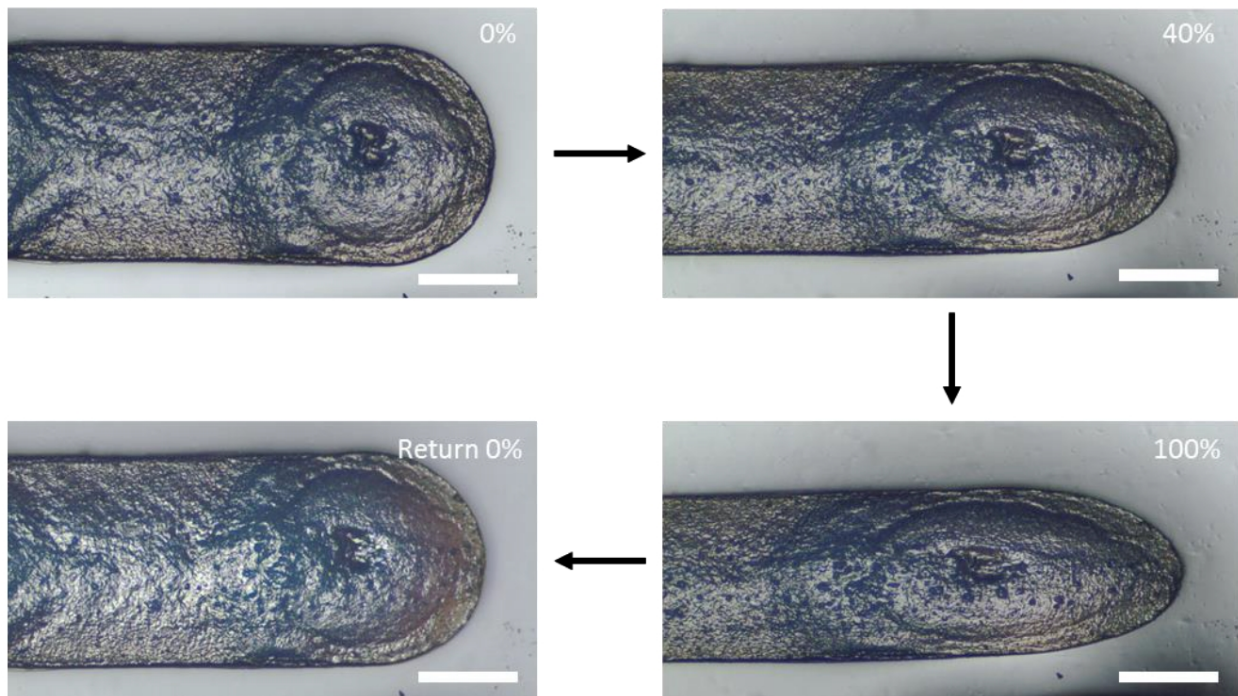


Figure 4.8 Optical micrographs of a BaTiO₃/PDMS feature printed on PDMS while the substrate is at relaxed state (0% strain), stretched to 40% or 100% strain, and returned to 0% strain. Scale bars in all images represent 200 μm .

Cyclic stretching tests were performed to study the durability of the BaTiO₃/PDMS composite dielectric. Figure 4.7b presents the $\Delta C/C_0$ (C_0 represents the pristine capacitance) of a device repeatedly stretched between 0% and 50% strains for 2000 cycles. The $\Delta C/C_0$ at 0% and 50% strain both show very slight increasing trend with roughly the same rate over the entire stretching test, which is different from the capacitors with pure silicone dielectric [161]. The reason for this synchronous shift is unclear at this moment and requires more detailed studies. One possible explanation is the reassembly of BaTiO₃ nanoparticles by migration inside the PDMS molecule network under the stimulation of cyclically changing stress fields [170]. We also monitored the change in leakage current during the stretching tests as shown in Figure 4.7c. It is impressive that the leakage current showed virtually no change when the device is stretched to 60% strain, implying the superior robustness of the BaTiO₃/PDMS dielectric and no formation of pinhole or crack during the stretching process.

An additional advantage of the BaTiO₃/PDMS hybrid gate dielectric is its excellent compatibility with the PDMS substrate, as manifested by the fact that no sliding between the dielectric and PDMS substrate was observed at a tensile strain up to 100% (as shown in Figure 4.8), which is significantly better than ionic gels [154]. Lastly, to confirm that the BaTiO₃/PDMS works well as gate dielectric for CNT TFTs, before fabricating stretchable TFTs on PDMS, we first printed the BaTiO₃/PDMS hybrid dielectric on TFTs with evaporated Ti/Au source/drain electrodes on Si substrates. Comparing Figure 4.9a and b, one can find the device with one layer of printed BaTiO₃/PDMS gate dielectric considerably outperforms the device with 300 nm SiO₂ as dielectric in terms of field-effect mobility ($7.72 \text{ cm}^2\text{V}^{-1}\text{s}^{-1}$ vs. $3.11 \text{ cm}^2\text{V}^{-1}\text{s}^{-1}$) and on/off current ratio (3.67×10^5 vs. 7.91×10^4). In addition, the representative output characteristics of the top-gated TFTs with printed hybrid dielectric (shown in Figure 4.9c) show typical MOSFET-like behavior. We have measured a number of such devices and the results are summarized in Figure 4.9d. The scattered data points indicate that the TFTs on silicon substrate with printed BaTiO₃/PDMS as gate dielectric usually exhibit field-effect mobility of around $7 \text{ cm}^2\text{V}^{-1}\text{s}^{-1}$ and on/off ratio above

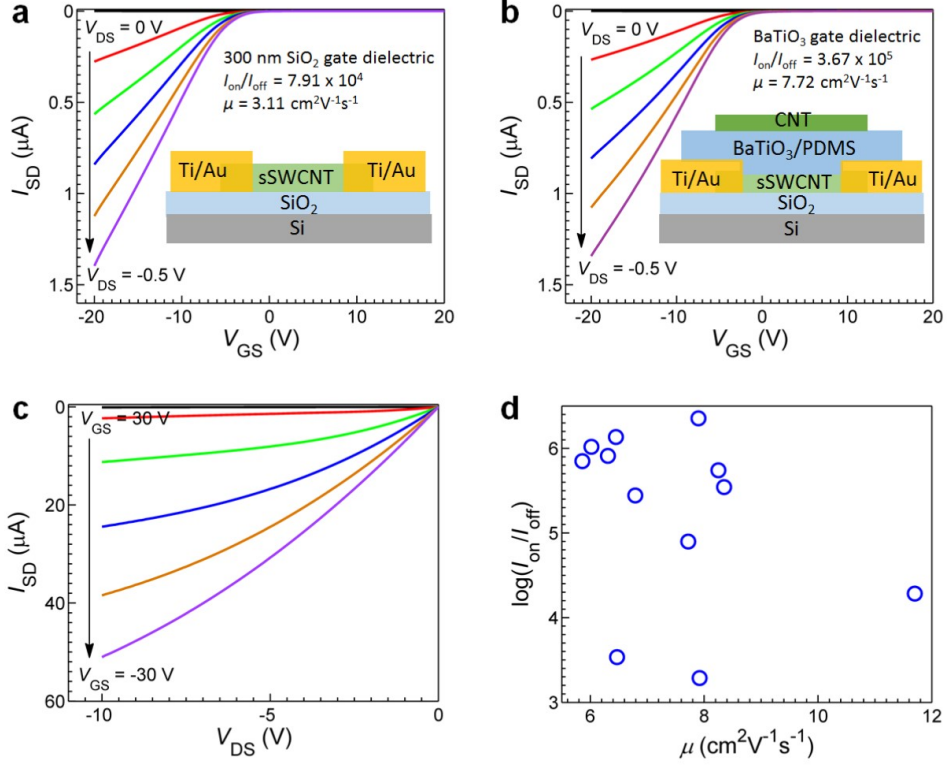


Figure 4.9 Electrical characteristics of top-gated TFTs on silicon substrate with BaTiO₃/PDMS as gate dielectric. a,b, Transfer characteristics of devices with 300 nm SiO₂ (a) or printed BaTiO₃/PDMS (b) as gate dielectric. Insets of a and b show the cross sectional schematics of the corresponding devices. c, Representative output characteristics of a TFT with the printed BaTiO₃/PDMS hybrid dielectric. d, A scattering points statistics of the electrical performance of devices with BaTiO₃/PDMS as gate dielectric.

10⁵. The above results suggest the BaTiO₃/PDMS composite indeed works well as gate dielectric for CNT TFTs.

Based on the stretchable CNT electrodes and BaTiO₃/PDMS hybrid gate dielectric developed above, stretchable TFTs were successfully fabricated on PDMS substrates by an all-printing process. Such printed TFTs typically have channel lengths (L) and channel widths (W) of ~150-200 μm and ~2500 μm, respectively. Figure 4.10 presents the representative transfer ($I_{SD} - V_{GS}$) and output ($I_{SD} - V_{DS}$) characteristics of the stretchable TFTs. The transfer curves presented in Figure 4.10a show good overlap between the forward and backward sweeps, indicating that hysteresis is nearly absent in our devices. In addition, according to the gray dashed line in Figure 4.10a, the gate leakage current remains

at a reasonably low level (~ 100 pA for $V_{GS} = 30$ V), which is in good agreement with the values measured from parallel-plate capacitors in Figure 4.7c. Linear scale transfer curve and transconductance (g_m) versus V_{GS} of the same device are shown in Figure 4.10b. The output characteristics presented in Figure 4.10c show unambiguous saturation behavior at high drain voltages that is typical for field-effect transistors and excellent linearity at low bias regime (Figure 4.10c inset), indicating negligible Schottky barrier at the interfaces between the channel semiconductor and source/drain electrodes. Most of our devices exhibit field effect mobility around $4 \text{ cm}^2\text{V}^{-1}\text{s}^{-1}$ and on/off ratio greater than 500 with maximum values of $7 \text{ cm}^2\text{V}^{-1}\text{s}^{-1}$ and 3000, respectively, which is respectable for the all-printing process.

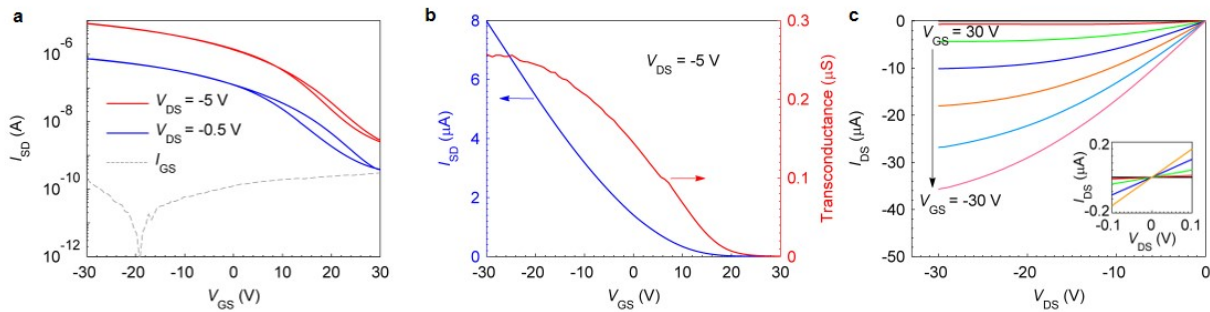


Figure 4.10 Representative electrical characteristics of the fully printed stretchable TFTs on PDMS. (a) Semilogarithmic scale plot showing the forward and backward sweep transfer characteristics ($I_{SD} - V_{GS}$) of a TFT measured at V_{DS} of -5 V (red) and -0.5 V (blue) and the gate leakage current curve ($I_{SG} - V_{GS}$) measured at V_{DS} of -0.5 V (gray dashed line). (b) I_{SD} (blue) and transconductance (red) as functions of V_{GS} plotted in linear scale for the same device in panel (a). (c) Output characteristics of the same TFT with V_{GS} varying from 30 V to -30 V. Inset shows the $I_{DS} - V_{DS}$ curves under low drain bias indicating negligible Schottky barriers at the semiconductor and S/D electrode interfaces.

Next, we investigated the electromechanical properties of the CNT TFTs printed on PDMS by performing systematic stretching tests along both channel length and channel width directions. The optical micrographs in Figure 4.11a and b reveal the geometric variations of two devices being stretched along L and W directions, respectively. When the device is stretched along L direction, the channel length elongates and channel width decreases (due to Poisson effect), while the opposite changes (W increases, L decreases) will take place under tensile strain along W direction. The geometric variations are also reflected

by the dimensional changes of the source/drain and gate electrodes, whose boundaries are marked by dashed lines. The geometric changes in the channel, as shown below, will have an effect on the TFT characteristics.

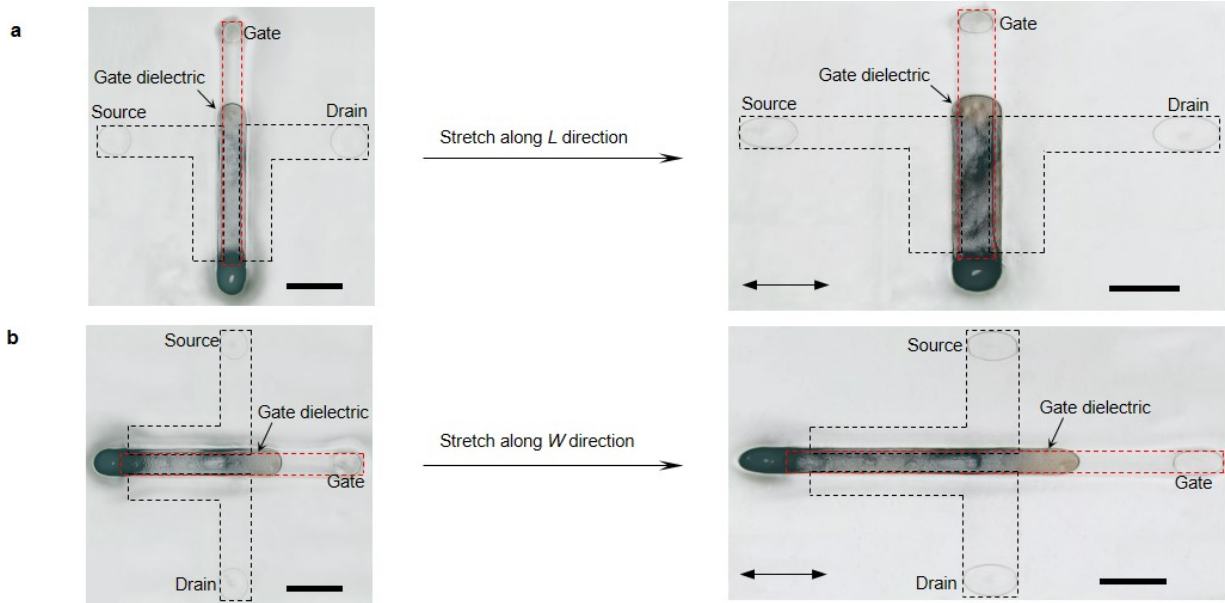


Figure 4.11 (a, b) Optical micrographs showing two devices stretched along channel length (a) and channel width (b) directions, respectively. Scale bars represent 1 mm.

Figure 4.12a and d present the evolution of transfer curves at V_{DS} of -0.5 V while the device is stretched up to 50% strain along the channel length and channel width directions, respectively. The on-state current drops by about one-half of its pristine value at 50% tensile strain along the L direction, while a very small decrease is observed under the same strain along the W direction. Meanwhile, the off-state current is drastically suppressed for both cases. The effects of tensile strain on the TFT drain current (I_{DS}) can be interpreted by three primary factors, namely the geometric change of the channel, the initiation and propagation of cracks in the sSWCNT network, and the enhancement in gating strength due to thinner gate dielectric. First, assuming the sSWCNT network and gating strength do not change, I_{DS} is proportional to the ratio of channel width to channel length (W/L), so I_{DS} would decrease when stretched along L direction and increase when stretched along W direction. Second, it is well-known that the surface of PDMS will be covered by a very thin layer of

silica after O₂ plasma treatment, which is a crucial step for our printing recipe. The silica skin is extremely brittle and, hence, forms ubiquitous cracks when the PDMS substrate is subjected to tensile strain. Consequently, many cracks appear in the otherwise continuous sSWCNT network following the deformation of the silica skin [161].

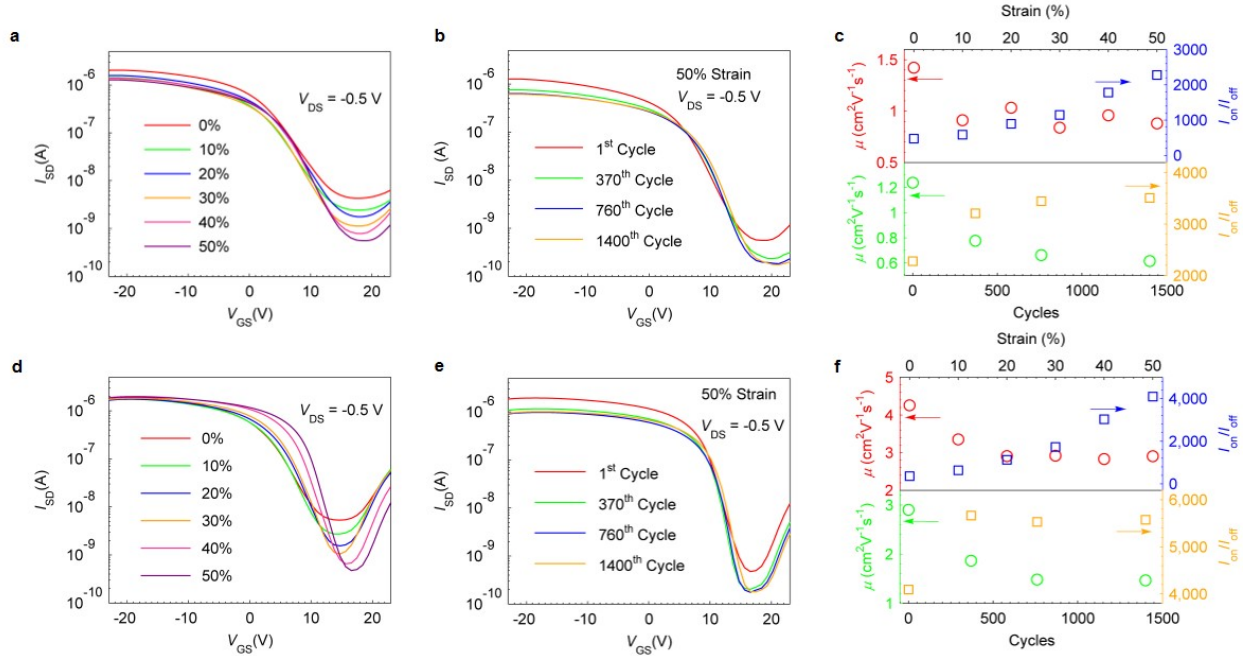


Figure 4.12 (a, d) Transfer characteristics at V_{DS} of -0.5 V, while the devices are stretched to various strain levels along the channel length (a) and channel width (d) directions, respectively. (b, e) Transfer characteristics at V_{DS} of -0.5 V, while the device is stretched to 50% strain for the 1st time (red), the 370th time (green), the 760th time (blue), and the 1400th time (orange) along channel length (b) and channel width (e) directions, respectively. (c, f) Field-effect mobility (left axes) and on/off current ratio (right axes) as functions of tensile strain (upper panel, in the 1st cycle) and stretching cycles (lower panel, at 50% strain) along channel length (c) and channel width (f) directions, respectively.

As a result, many percolating pathways are cut off, leading to a reduction in I_{DS} . Considering both the influence of geometric change of the channel and structural change of the sSWCNT network, one can easily understand the distinct behaviors of on-state current when stretched along different directions. It is worth mentioning that the formation of cracks in the channel has a larger influence on the metallic percolation pathways than on the semi-conducting ones because the sSWCNT ink used here contains only 2% metallic nanotubes,

which is beneficial for the improvement of on/off current ratio under tensile strain. Finally, the BaTiO₃/PDMS dielectric layer will also become thinner under tensile strain (see Figure 4.7a), which contributes to a stronger gating strength and consequently further suppression of the off-state current. The upper panels of Figure 4.12b,e present the device field-effect mobility (left axis) and on/off current ratio (right axis) as functions of tensile strains along the L direction and W direction, respectively. Device mobility (μ) is extracted using the equation in linear region $\mu = g_m L / (W V_{DS} C_{ox})$, where g_m and C_{ox} are transconductance and gate capacitance, respectively. Gate capacitance is determined by direct capacitance-voltage (CV) measurements on the TFTs and considering the geometric changes of the channel. Regardless of stretching direction, mobility decreases by about 1/3 of its original value under 50% strain, reflecting the microscopic structural changes in the sSWCNT networks discussed above. On the other hand, the on/off ratio increases by almost 1 order of magnitude due to the significantly suppressed off-state current.

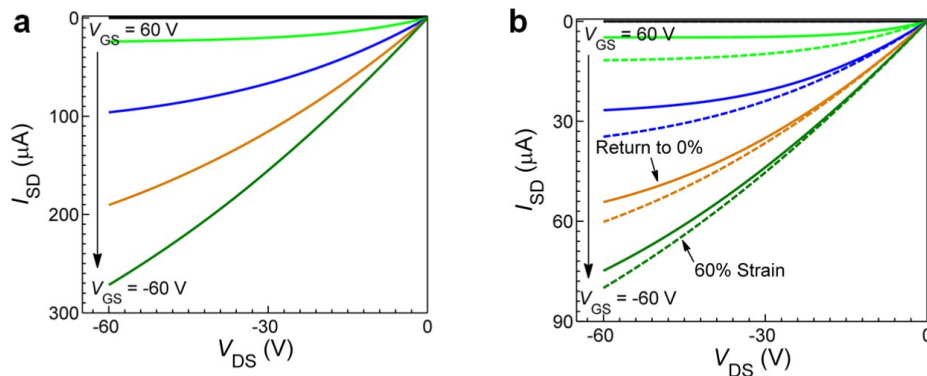


Figure 4.13 Output characteristics of a fully-printed stretchable CNT TFT at pristine state (0% strain) (a), after being stretched to 60% strain (dashed lines in panel b) and after returning to 0% strain (solid lines in panel b).

Figure 4.13 presents the output characteristics of another device being stretched along the channel length direction. By comparing Figure 4.13a and b, one can find that the current level drops to about 1/3 of the pristine value after the initial stretch to $\sim 60\%$ strain. After that, the current level settles and remains nearly unchanged after the tensile strain is released (Figure 4.13b). Regardless of the tensile strain, the device maintains very standard MOSFET

characteristics with clear saturation regions in the output curves.

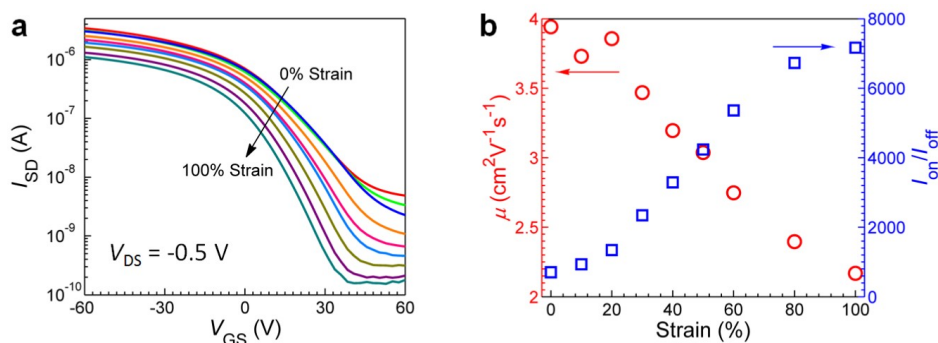


Figure 4.14 Electrical characteristics of a stretchable TFT when being stretched to 100% strain along the channel length direction. a, Evolution of the transfer characteristics at various tensile strain values up to 100%. b, Field-effect mobility and on/off current ratio as functions of tensile strain.

The maximum tensile strain our devices can withstand is primarily limited by the stretchability of the PDMS substrates. Certain devices remain working properly under strains that are significantly higher than 50% as long as the PDMS substrate does not rupture. Figure 4.14 presents the electrical characteristics of one of such devices when being stretched up to 100% strain along the channel length direction. As expected, the drain current (I_{DS}) does drop due to the geometric changes of the channel and the cracks induced in the sSWCNT network. Nevertheless, the off-state current shows a much more pronounced decrease than the on-state current does because of the low content of metallic carbon nanotubes (only 2%) in the channel and the enhanced gating strength caused by thinner gate dielectric under strain. As a result, the on/off current ratio increases to almost 10^4 at 100% strain. In the meantime, the field-effect mobility drops to roughly half of the pristine value, which is well acceptable considering the high tensile strain.

The stretchable CNT TFTs were then subjected to long-term cyclic stretching with a maximum strain of 50%. The transfer characteristics at 50% strain after different numbers of cycles are shown in Figure 4.12a (stretching along L direction) and Figure 4.12d (stretching along W direction). The device field-effect mobility (left axis) and on/off current ratio (right axis) at 50% strain are plotted as functions of stretching cycles in the lower panels of Figure

4.12c and f for stretching along the L and W directions, respectively. Upon repeated stretching, the on-state current, off-state current, and mobility drop further while the on/off current ratio continues to increase, which could be attributed to further expansion of the cracks and probable initiation of new cracks in the sSWCNT networks. All device performance metrics start to stabilize after hundreds of stretching cycles

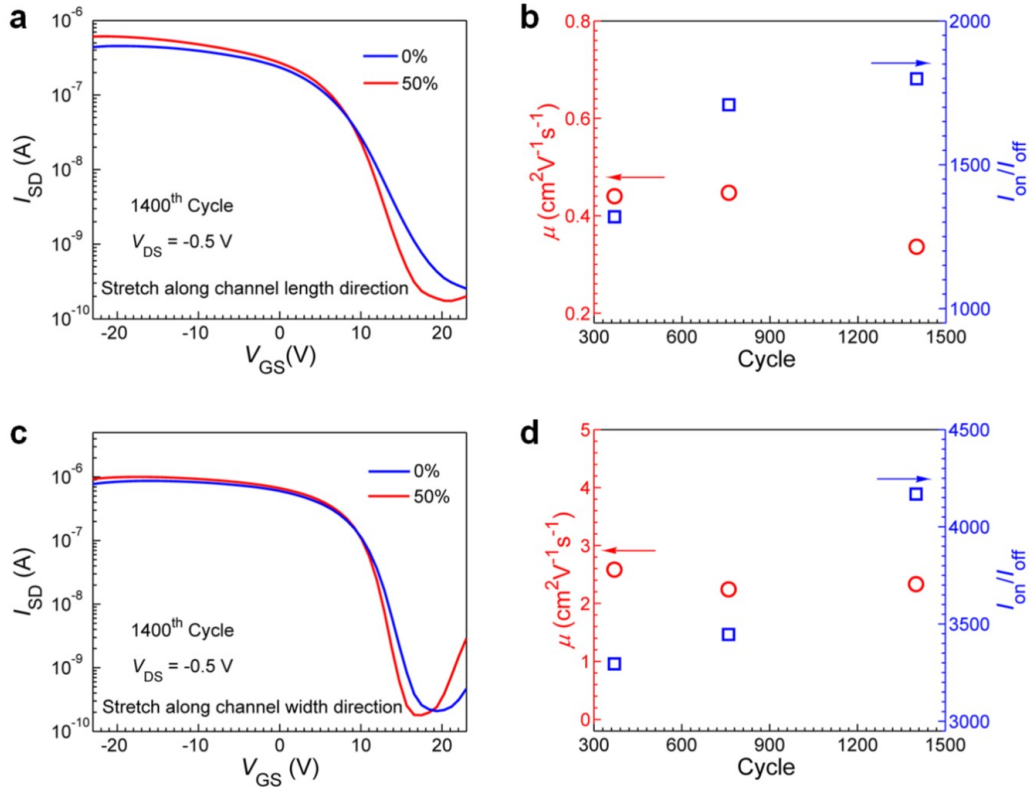


Figure 4.15 Extra data about the stretching tests conducted on the same devices presented in Figure 4.12 of the main paper. a,c, Transfer curves measured at V_{DS} of -0.5 V under 0% (blue) and 50% (red) strains during the 1400th stretching cycle when the device is stretched along channel length (a) and channel width (c) directions. b,d, Field-effect mobility (red circles) and on/off current ratio (blue squares) at 0% strain as a function of stretching cycle when the device is stretched along channel length (b) and channel width (d) directions.

Figure 4.15 presents more data about the stretching tests conducted on the same devices presented in Figure 4.12. Figure 4.15a and c show the transfer curves measured at $V_{DS} = -0.5$ V under 0% (blue) and 50% (red) strain during the 1400th stretching cycle when stretched along channel length (Figure 4.15a) and channel width (Figure 4.15c) directions, respectively.

Regardless of the stretching direction, the on-state (off-state) current at 50% strain is slightly higher (lower) than that at 0% strain, which can be explained by the enhancement of the gating strength under tensile strains. The difference between the transfer curves at 0% and 50% strains is overall very small for both cases, indicating the TFT electrical performance has almost stabilized after more than 1000 stretching cycles. Figure Figure 4.15b and d present the field-effect mobility (red circles) and on/off current ratio (blue squares) at 0% strain as functions of stretching cycles for the device stretched along channel length (Figure 4.15b) and channel width directions (Figure 4.15d), respectively. For both cases, the mobility shows slight decreasing trend and the on/off ratio keeps increasing steadily, which could be explained by the constant evolution of the sSWCNT network during the repeated stretching process.

Overall, the difference between the transfer curves at 0% and 50% strains is practically negligible for both devices, indicating the TFTs are stabilized and show almost strain-independent electrical performance after more than 1000 stretching cycles. The above results of stretching tests reveal that our printed CNT TFTs exhibit excellent mechanical robustness and can maintain very stable electrical performance under harsh conditions often encountered in real life wearable electronics applications.

We have also successfully demonstrated fully printed stretchable integrated logic circuits on PDMS, including inverter, NOR and NAND gates. Figure 4.16 shows the optical micrographs of a resistive load p-type inverter (left), a resistive load two-input NOR gate (middle) and a two-input NAND gate (right). We followed similar procedures as those reported in our previous work to fabricate the logic gates [164]. In brief, after fabricating the driving TFT, unsorted CNTs were printed in the load resistor layer by layer until an optimal performance was achieved. Systematic electrical and electromechanical characterizations were conducted on the stretchable logic circuits.

Figure 4.17a presents the inverter voltage-transfer characteristics (VTCs) with a V_{DD} of 10 V under various strains along the channel length direction of the driving TFT. The

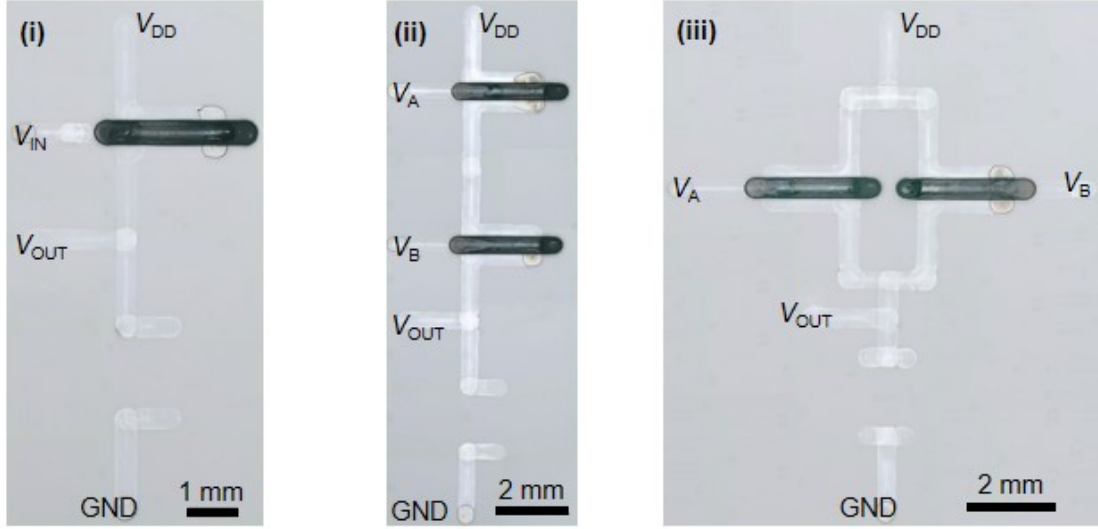


Figure 4.16 Optical micrographs of a printed resistive load inverter (i), a resistive load two-input NOR gate (ii), and a two-input NAND gate (iii).

inverter exhibits more pronounced rail-to-rail output voltage swing as the tensile strain is increased to 60%, owing to the improved on/off ratio of driving TFT. In addition, repeated stretching tests indicate that the stretchable inverter exhibits very stable performance, as shown in Figure 4.17b.

The output voltage of a resistive load inverter is determined by the voltage division between the channel resistance ($R_{channel}$) of the driving TFT and the load resistance (R_{load}) and can be expressed as

$$V_{OUT} = \frac{V_{DD}R_{load}}{R_{channel} + R_{load}} \quad (4.5)$$

When the TFT is turned on (low V_{IN} for a p-type TFT), R_{load} is significantly higher than $R_{channel}$; hence, V_{OUT} is approximately equal to V_{DD} ; similarly, V_{OUT} is close to 0 when the TFT is turned off (high V_{IN} for a p-type TFT) because $R_{channel}$ is much greater than R_{load} . From Equation 4.5 and considering the evolution of transfer characteristics of the driving TFT discussed in Figure 4.12, one can easily understand the dependence of inverter VTCs on tensile strains in Figure 4.17a.

Panel c and d of Figure 4.17 present the output characteristics of the two-input NOR gate and NAND gate measured with a V_{DD} of 10 V, while the circuits are at pristine state

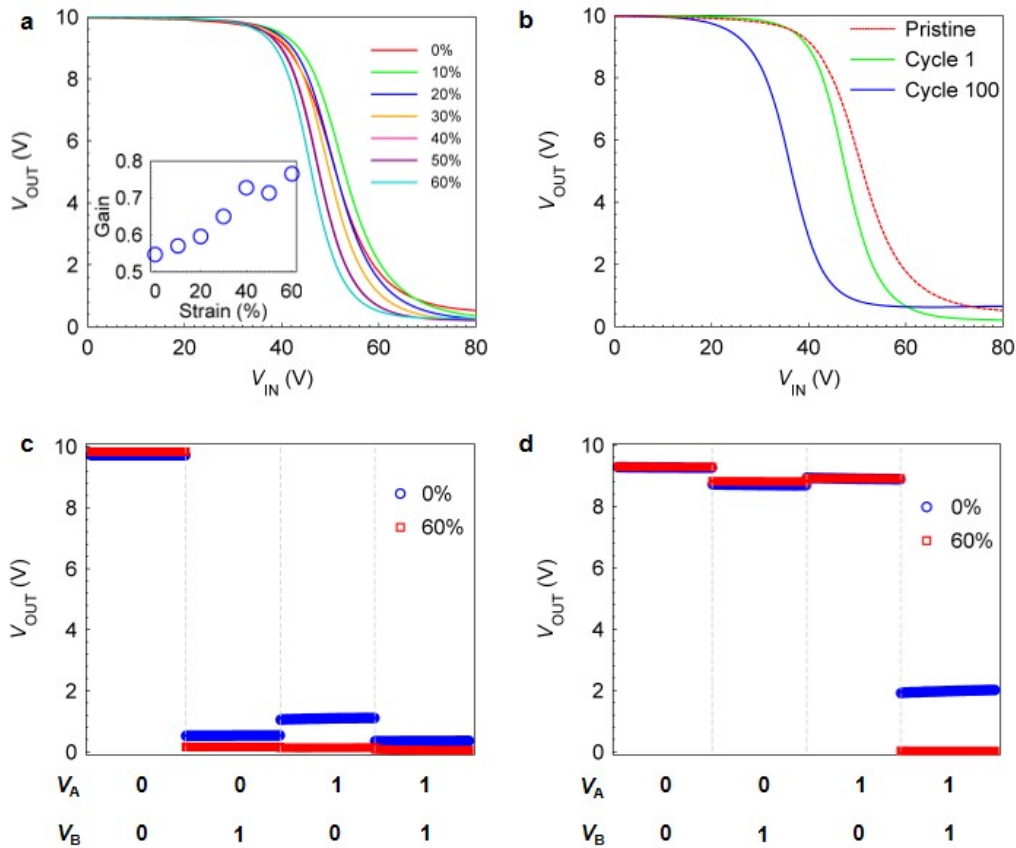


Figure 4.17 Fully printed stretchable integrated logic circuits on PDMS. (a) Inverter voltage transfer characteristics (VTCs) measured with a V_{DD} of 10 V, while the device is stretched to various strain levels along the channel length direction of the driving TFT. Inset shows the inverter gain as a function of tensile strain. (b) Inverter VTCs measured at a V_{DD} of 10 V while the device is at pristine state (0% strain, red) and at 0% strain after 70 (blue) and 100 (green) stretching cycles with a maximum strain of 50% along the channel length direction of the driving TFT. (c, d) Output characteristics of the NOR gate (c) and NAND gate (d) measured at a V_{DD} of 10 V while the device is at pristine state (0% strain, blue circles) and stretched to 60% strain (red squares) along the channel length direction of the driving TFTs. For both NOR gate and NAND gate, input voltages of 80 and 0 V are treated as logic 1 and 0, respectively.

(blue circles) and under 60% strain (red squares) along the channel length direction of the driving TFTs. As expected, the NOR and NAND gates both function properly by showing unambiguous output logic 1 and 0 states. Furthermore, the contrast between the two logic states becomes even more pronounced when the circuits are stretched to 60% strain due to the significantly improved on/off current ratio of the driving TFTs. Lastly, the NOR and NAND

gates both exhibit very stable electrical performance during repeated stretching tests. Figure 4.18 shows the output characteristics of a NOR gate measured during the 1870th stretching cycle (Figure 4.18a) and a NAND gate measured during the 10th stretching cycle (Figure 4.18b). As expected, both logic gates show negligible changes in electrical performance while being stretched to high tensile strain values. We have tested the NOR gate up to 2000 stretching cycles and the circuit exhibited with very stable performance. The NAND gate also exhibited very stable performance during the stretching tests. It accidentally failed after the 10th stretching cycle due to the breakage of the PDMS substrate instead of the electrical failure of the devices.

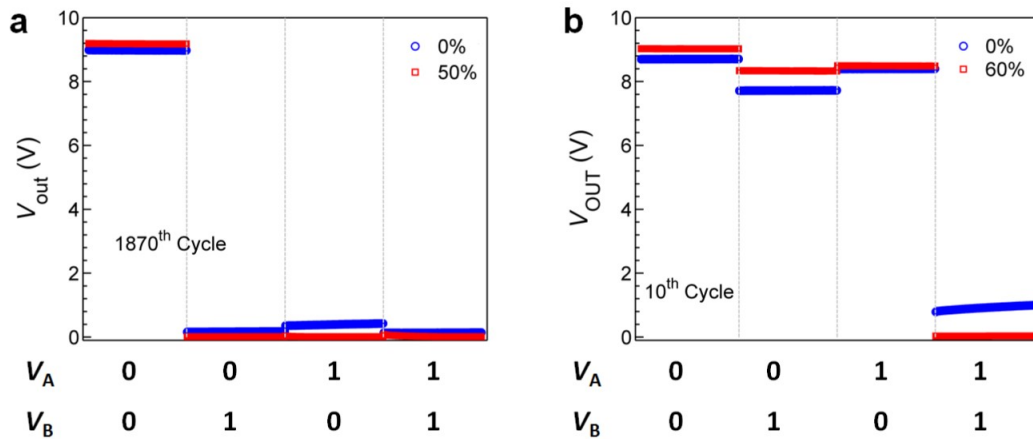


Figure 4.18 Output characteristics of (a) a NOR gate measured during the 1870th stretching cycle and (b) a NAND gate measured during the 10th stretching cycle.

4.4 Summary

In summary, by materials and ink formulation development, we have successfully demonstrated intrinsically stretchable thin-film transistors and integrated logic circuits on PDMS using an all-printing process. The devices and circuits can withstand thousands of stretching cycles with tensile strain exceeding 50% along any directions while maintaining respectable and stable electrical performance. This work is significant as it enables a promising approach to realize low-cost and large-area fabrication of stretchable electronics, which may find a wide

range of applications in wearable electronics or printed stretchable displays. There is still plenty of room for follow-up research along this direction in further improving the electrical performance, stretchability, and stability of the devices by optimizing the channel semiconductor, gate dielectric layer, and substrate. Although other semiconducting materials like P3HT [148], layered MoS₂ [152], and SnO₂ nanowires [171] have been exploited as the channel material for stretchable TFTs, carbon nanotubes are still the overall best choice. Using surfactant-free inks with longer nanotubes could potentially diminish the number of intertube junctions and reduce the tube-to-tube junction resistance, which could further improve the device mobility toward that of individual carbon nanotubes [143]. Using longer nanotubes are beneficial to the improvement of stretchability. As for the dielectric materials, higher permittivity is needed to further lower the operating voltage. According to a recent study, composite dielectric with carbon nanotube as fillers at a concentration near the percolating threshold shows gigantic permittivity [172], which is worth consideration in future studies. As for the substrate, although PDMS is widely used for stretchable electronics, its intrinsic hydrophobicity complicates the printing process and the brittle silica skin formed on its surface after O₂ plasma treatment is prone to form microscopic cracks. Additionally, PDMS also has high O₂ and H₂O permeability, which could compromise the stability of light-emitting devices under ambient conditions. Therefore, alternative elastomeric substrates with easy-handling surface and low gas permeability are needed to further simplify the fabrication process and to improve the device stability. Finally, more research effort should also be devoted to the development of stretchable light-emitting devices, sensors and actuators, as well as circuit design and integration of these elements into more sophisticated circuits and smart systems. There is no doubt that numerous research efforts are still needed to ultimately bring stretchable electronics from academic research to real life commercial products. The results reported in this paper represent an encouraging leap toward this goal.

CHAPTER 5

FULLY PRINTED FLEXIBLE PHOTODETECTOR BASED ON CARBON NANOTUBES

In this chapter, we have reported methods for fabricating SWNT-based thin-film transistors using a fully printed process and systematically studied their photoresponse. Bolometric effect was observed in such devices upon laser illumination, which leads to gate-voltage-dependent photoresponse characteristics. Additionally, the photodetectors exhibit good reliability under bending conditions owing to the ultrathin polyimide substrate used and the superior mechanical flexibility of the carbon nanotube network. Such photodetectors would be useful for the development of ubiquitous, low-cost and large area flexible electronic systems. Additionally, we have demonstrated the wavelength selective photodetectors utilizing the observed bolometric effect.

5.1 Introduction

Photodetectors play an important role in modern technology. Generally speaking, the operation of photodetectors can rely on photovoltaic, photo-thermoelectric, or bolometric effects [173]. In particular, bolometers, which are widely used in astronomy and particle physics, transduce the absorbed radiation into a rise in temperature, which in turn induces variations in resistance that can be read out as electrical signals [174]. Over the past two decades, the development in nanomaterials provides new platforms for bolometers with improved sensitivity, speed and flexibility. Semiconducting single-wall carbon nanotubes (sSWCNTs), featured with direct bandgaps and unique one-dimensional van Hove singularities and excitonic states, have been extensively studied for photodetecting applications [175]. An intriguing attribute of sSWCNTs is the structure-dependent bandgap, which enables the wavelength-selective detection of a wide spectrum of light ranging from visible to infrared region. Although a

photothermal signature was recently unveiled [176], the photocurrent of individual sSWCNTs is predominantly photovoltaic in nature, where the incident photons generate strongly bound excitons, which are subsequently separated into free electrons and holes under an electric field [175]. In macroscale assemblies of carbon nanotubes, however, contribution from direct photocurrent can be neglected due to the ultrafast relaxation of excitons and the lack of a sufficient electric field [177, 178]. Instead, the absorbed energy is effectively transferred to the crystal lattice through strong electron-phonon interaction, which results into a rise in temperature, i.e. the bolometric effect [179]. Bolometric response of various carbon nanotube samples, including thin films and polymeric composites, has been demonstrated to be a viable method for photodetection [179, 180, 181, 182, 183, 184, 185].

Several groups have reported bolometers or bolometric effect involved photodetector fabricated by carbon nanotubes [186, 187, 188, 189, 190, 191, 192, 193, 194]. However, most reported results used the traditional fabrication process including metal deposition, electron-beam lithography and etching. These processes either require high vacuum or are not suitable for large area flexible applications. Printing has been proposed as a viable solution to enable the application of flexible and large surface electronics [185, 195, 196, 197]. And compared with roll-to-roll and screen printing, the ink-jet printing is maskless and only applies the materials onto the active region, thus saving the materials, resulting in lower cost and operation flexibility.

Herein, we report the bolometric-effect-based photoresponse in thin-film transistors fabricated using printing process. The photoresponse (i.e. change in resistance) was found to be dependent on the gate voltage applied. For a negative gate voltage, when the device is fully turned on, the carrier mobility decreases due to increased phonon scatterings as the temperature rises upon laser illumination, leading to an increase in resistance. For a positive gate voltage, when the sSWCNT network is depleted, the contribution from increase in carrier concentration at elevated temperatures dominates, resulting in a decrease in resistance.

5.2 Results and Discussion

Figure 5.1a shows the schematic diagram of fully printed back-gated thin film transistor used in this work.

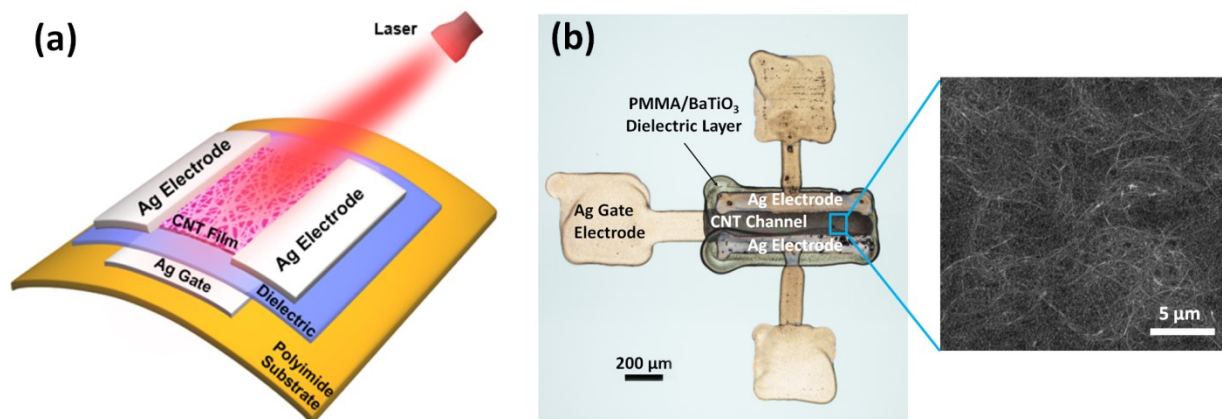


Figure 5.1 a. Schematic diagram of fully printed SWNTs based TFTs. b. Optical image of the transistor and SEM image of printed SWNTs on top of BTO layer.

To begin with, we spin-coated an ultrathin polyimide (HD MicroSystems, PI-2525) film with the thickness of ~ 10 micrometers on top of silicon wafer, serving as the substrate. The ultrathin substrate is essential to the flexibility of the devices and circuits. Next the back-gate electrode was printed using the silver nanoparticle ink (PG-007 AA, Paru Corporation, South Korea) by GIX Microplotter (Sonoplot Inc.), followed by annealing at $180\text{ }^{\circ}\text{C}$ for 10 min to improve the conductivity of the silver electrode. Subsequently, an ink composed of BaTiO_3 nanoparticles and PMMA (PD-100, Paru Corporation, South Korea) was printed as the hybrid dielectric layer. The whole wafer was placed on a hot plate at $60\text{ }^{\circ}\text{C}$ while printing to avoid the coffee ring effect. In case of possible gate leakage, we printed the dielectric layer two more times. And then poly-L-lysine solution (0.1% w/v in water; Sigma Aldrich) was printed on top of the dielectric layer followed by DI water rinsing and nitrogen blowing to functionalize the surface, serving as the amine-terminated adhesion layer. Thus, the commercially available 0.01 mg/mL semiconducting nanotube solution (NanoIntegris Inc.) could be printed onto the channel region uniformly. And in order to get an optimal

performance for the transistors, the nanotubes were printed for multiple times to increase the density of the channel. Finally, Source/Drain (S/D) electrodes were printed by the same method with printing the back-gate electrode using the same silver ink. Once the whole fabrication process was done, the polyimide substrate was peeled off from the silicon wafer, resulting in an extremely flexible thin film transistor. Figure 5.1b illustrates the optical image of the printed transistor, and it could be seen every region is well-defined, which ensures the good performance. In addition, the SEM image is given to show the uniformity of printed SWNTs network.

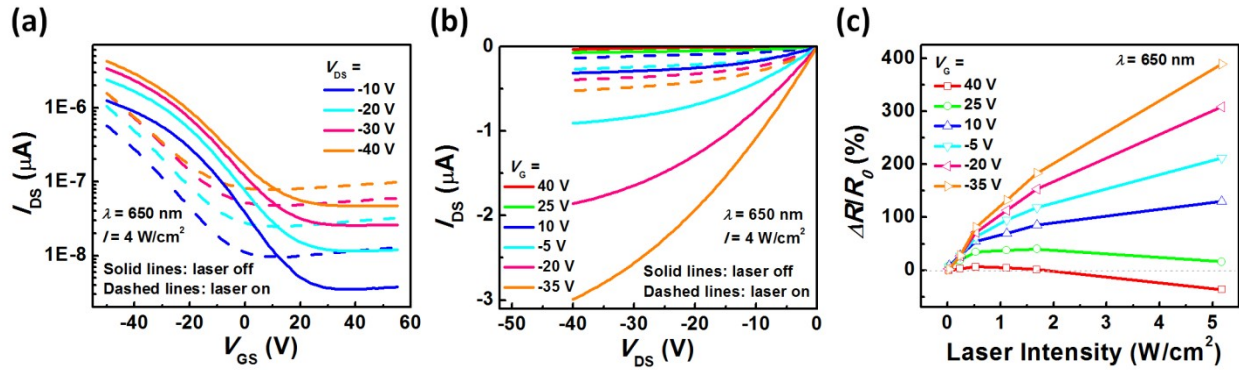


Figure 5.2 a. Transfer characteristics of fully printed TFTs based on SWNTs with and without the laser illuminating. b. Output characteristics of fully printed TFTs based on SWNTs with and without the laser illuminating. c. The relative change of resistance as a function of the laser intensity under different gate bias.

Figure 5.2a and b shows the representative transfer and output characteristics of a printed thin-film transistor with and without laser illumination, respectively. A red laser diode with a wavelength (λ) of 650 nm and an intensity of ~ 4 W/cm^2 was used. The devices exhibit conventional field-effect-transistor-like output characteristics with clear current saturation. With the laser turned on (dashed lines), the output current (I_{DS}) underwent drastic changes. It can be clearly seen that the changes of I_{DS} in response to laser illumination depend on the applied gate voltage (V_G). At V_G of 40 V and 25 V, when the channel is depleted, I_{DS} increases slightly upon laser illumination, whereas under more negative V_G , when the transistor is turned on, a significant decrease in I_{DS} can be observed.

As with the free standing films of SWCNTs [179], we attribute the photoresponse in our devices to bolometric effect, i.e. a rise in the temperature of SWCNT network upon light irradiation, rather than photovoltaic effect. The conjecture of bolometric effect is reasonable considering the following facts: i) carbon nanotubes possess an extremely high absorption coefficient (10^4 to 10^5 cm^{-1}) over a wide spectrum extending from ultraviolet to far-infrared region [179]; ii) carbon nanotubes exhibit strong thermal response to electromagnetic radiation as evidenced by the temperature rise up to 100 K merely due to the environmental black-body radiation [179] and ignition phenomenon upon exposure to conventional photographic flashlight [195]; and iii) the monolayer network of SWCNTs in our TFTs has extremely small heat capacity which can lead to a significant increase in temperature due to the absorption of a small amount of energy. In contrast, it is unlikely for the photovoltaic effect (the creation of electron-hole pairs upon light illumination) to be the predominant factor governing the photoresponse in our devices due to a number of reasons: i) With negative gate bias, the current in our device decreases drastically under light illumination, which is contradictory to what is expected from photovoltaic effect; ii) The channel of our device consists of random networks of short carbon nanotubes with numerous tube-to-tube junctions. It will be very difficult, if not impossible, for the photo-generated carriers to reach the electrodes.

In general, the increase in temperature of a semiconductor can result in an increase of carrier concentration due to more thermally excited free carriers as well as a drop in carrier mobility due to increased phonon scattering. Two factors compete with each other in affecting the conductivity of the material [198]. At a very positive V_G , the carrier concentration is rather low because the SWCNT network is fully depleted by the electrostatic coupling from the gate electrode. As a result, the increase in carrier concentration at elevated temperatures upon light illumination would have a stronger influence on the conductivity than the reduction in mobility, resulting in an increased output current. In contrast, as the device transitions into the inversion mode (very negative V_G), the carrier concentration is very high so that the conductivity is dominated by the effect from decrease in carrier mobility.

Figure 5.2c presents the relative change in channel resistance ($\Delta R/R_0$), extracted from the output characteristics and plotted as functions of laser intensity for various values of V_G . An unambiguous increasing trend in the magnitude of $\Delta R/R_0$ can be observed as the laser intensity increases, regardless of the applied V_G . The increase in photoresponse is due to larger temperature changes caused by larger amount of absorbed radiation at higher laser intensities. In addition, the evolution of photoresponse can be clearly identified as V_G was swept from 40 V to -35 V. A transition point ($\Delta R/R_0 = 0\%$) exists somewhere between $V_G = 10$ V and 25 V (the blue and red lines in Figure 5.2c), where the effects from increase in carrier concentration and the reduction in mobility contribute equally to the conductivity. As a result, the output current would ideally remain unchanged irrespective of the laser intensity.

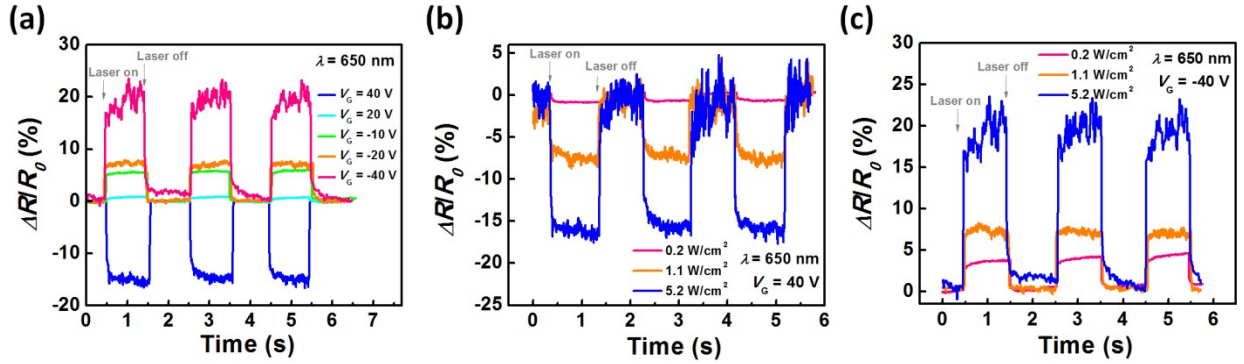


Figure 5.3 Time response of fully printed SWNTs based TFTs a. under various gate bias when fixing the laser intensity to 5.2 W/cm^2 . b. under illuminated laser with various laser intensity when fixing the gate bias to 40 V. c. under illuminated laser with various laser intensity when fixing the gate bias to -40 V.

Figure 5.3a compares the photo-switching characteristics measured at different gate voltages with a laser intensity of 5.2 mW/cm^2 . Again, opposite photoresponse is observed when the device is in on ($V_G = -40 \text{ V}$) and off ($V_G = 40 \text{ V}$) states. And the transitive gate bias is estimated as $\sim 20 \text{ V}$. The photo-switching behaviors measured using the same laser wavelength with different intensities at $V_G = 40 \text{ V}$ and $V_G = -40 \text{ V}$ are shown in Figure 5.3b,c, respectively. Higher laser intensities result in larger photoresponse, which is in agreement

with the results in Figure 5.3c. The rise/fall time is also extracted as 2 ms \sim 4 ms, which is comparable to the other reported results.

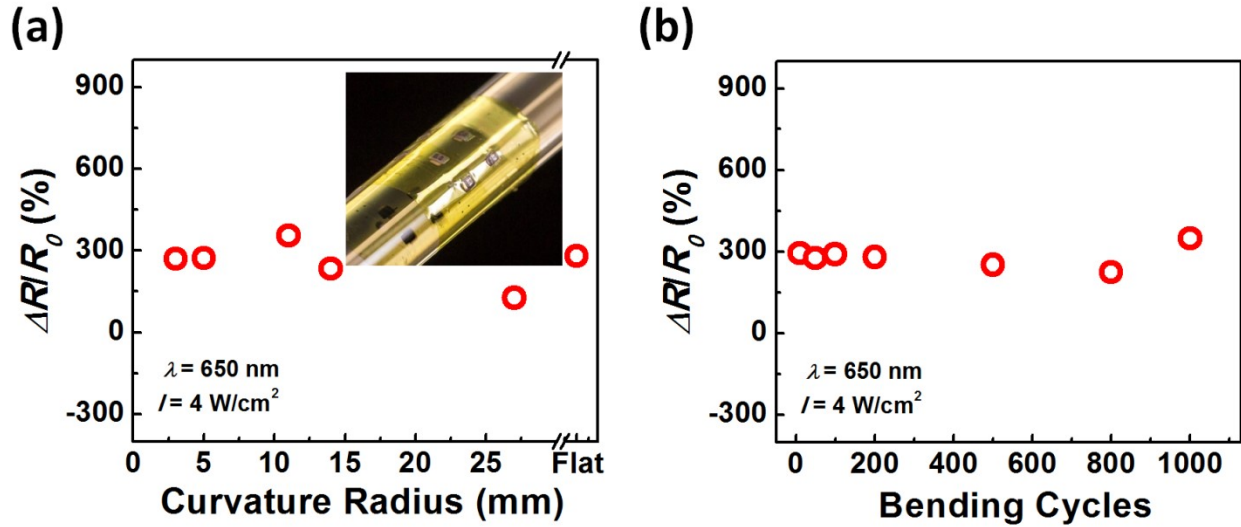


Figure 5.4 Bending tests on the fully printed SWNTs based TFTs under a. different curvature radius and b. different bending cycles.

Thanks to the ultrathin flexible polyimide substrate as well as the remarkable mechanical flexibility of the gate dielectric and SWNTs network, the systematic bending tests for the fully printed TFTs is illustrated in Figure 5.4. As shown in the insert figure of Figure 5.4b, we wrap the devices onto a glass tube for the bending test. And the response of the TFTs under laser illuminating exhibits only minimal variations even when the curvature radius goes down to 3 mm (Figure 5.4a) and almost remains constant throughout the process of up to 1000 bending cycles (Figure 5.4b) with a curvature radius of 5 mm. The stability and reliability of the devices under different curvature radius and bending cycles ensure its potential application in the flexible electronics field.

5.3 Potential Application - Wavelength Selective Photodetector

Based on the observed bolometric effect on the SWNTs based Thin Film Transistors, we have demonstrated the application of wavelength selective photodetectors by applying different

types of SWNTs for the TFTs. Specifically, Two TFTs are fabricated using the conventional cleanroom process with a global Si gate, SiO₂ dielectric and Ti/Au S/D electrodes. And the (9,8) single chirality nanotubes and the 99% semiconducting nanotubes are used as the channel materials, respectively. The photoluminescence (PL) spectroscopy maps of the (9,8) nanotube sample before and after the chirality-based sorting process are shown in Figure 5.5 a,b, respectively. From the data, one can easily see that the various semiconducting species in the starting material were effectively removed, leaving behind only (9,8) chirality as the main species, whose purity is estimated to be 73.8% among all semiconducting species.

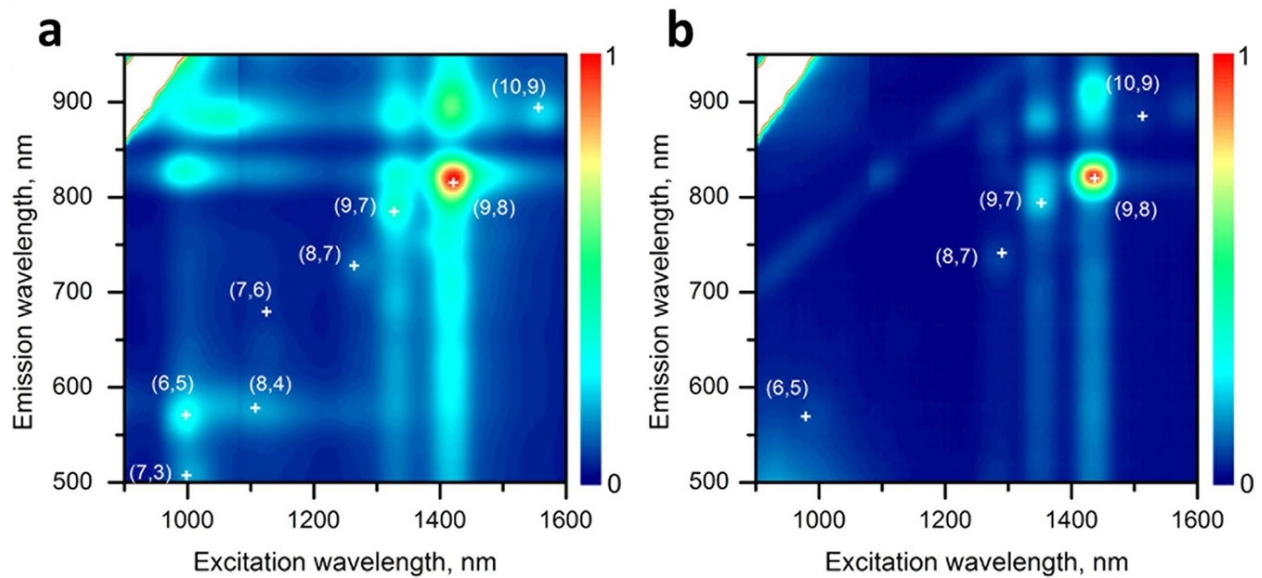


Figure 5.5 Photoluminescence excitation mapping for the (9,8) nanotube sample obtained (a) before and (b) after the chirality-based enrichment process.

The output characteristics of the two TFTs are measured when the devices are illuminated by the lasers with different wavelength of 520 nm, 650 nm, 807 nm, and 980 nm, as shown in Figure 5.6.

we compare the photoresponse of two devices. Figure 5.7a compares the absorption spectra of these two carbon nanotube samples. The single chirality (9,8) SWCNT sample exhibits several sharp absorption peaks at wavelengths around 555, 660 and 813 nm, whereas the 99% semiconducting nanotube sample from Nanointegris exhibits two broad peaks around 500

and 1024 nm. Both types of devices went through the same measurements performed in Figure 5.2 using four laser diodes with different wavelengths, namely, 520 nm, 650 nm, 807 nm, and 980 nm. The photoresponse ($\Delta R/R_0$) of both types of devices were extracted from the output characteristics (Figure 5.6) and summarized in Figure 5.7b.

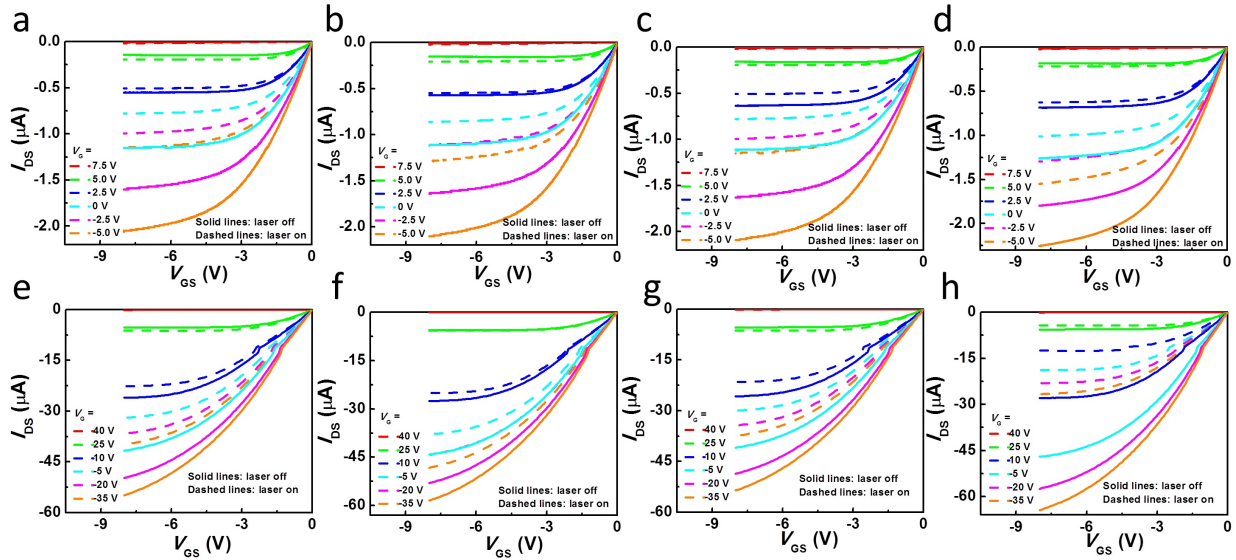


Figure 5.6 (a-d) Output characteristics (I_{DS} - V_{DS}) of a (9,8) nanotube thin-film transistor measured before and after laser illumination with (a) $\lambda = 520$ nm, (b) $\lambda = 650$ nm, (c) $\lambda = 807$ nm, and (d) $\lambda = 980$ nm. (e-h) Output characteristics of a 99% semiconducting nanotube thin-film transistor measured before and after laser illumination with (e) $\lambda = 520$ nm, (f) $\lambda = 650$ nm, (g) $\lambda = 807$ nm, and (h) $\lambda = 980$ nm.

It can be seen that the dependence of photoresponse on gate voltage applies to the semiconducting-enriched SWCNTs as well (i.e. positive $\Delta R/R_0$ for negative gate voltages and negative $\Delta R/R_0$ for positive gate voltages). More importantly, the trend in photoresponse for different wavelengths correlates well with the corresponding absorption spectra in Figure 5.7a. Specifically, the device with single chirality (9,8) nanotubes (orange color in Figure 5.7b) exhibit larger photoresponse than the device with 99% semiconducting nanotubes (red color) at wavelengths of 520, 650 and 807 nm, each of which situates closely to the absorption peaks of (9,8) nanotubes. In contrast, for the laser with a wavelength of 980 nm, the absorption of (9,8) nanotubes become much weaker compared with the 99%

semiconductor-enriched nanotube sample, who has a strong and broad absorption peak at around 1024 nm. Not surprisingly, the device with 99% semiconductor-enriched nanotubes exhibit much larger photoresponse at a wavelength of 980 nm compared with the device with single chirality (9,8) nanotubes.

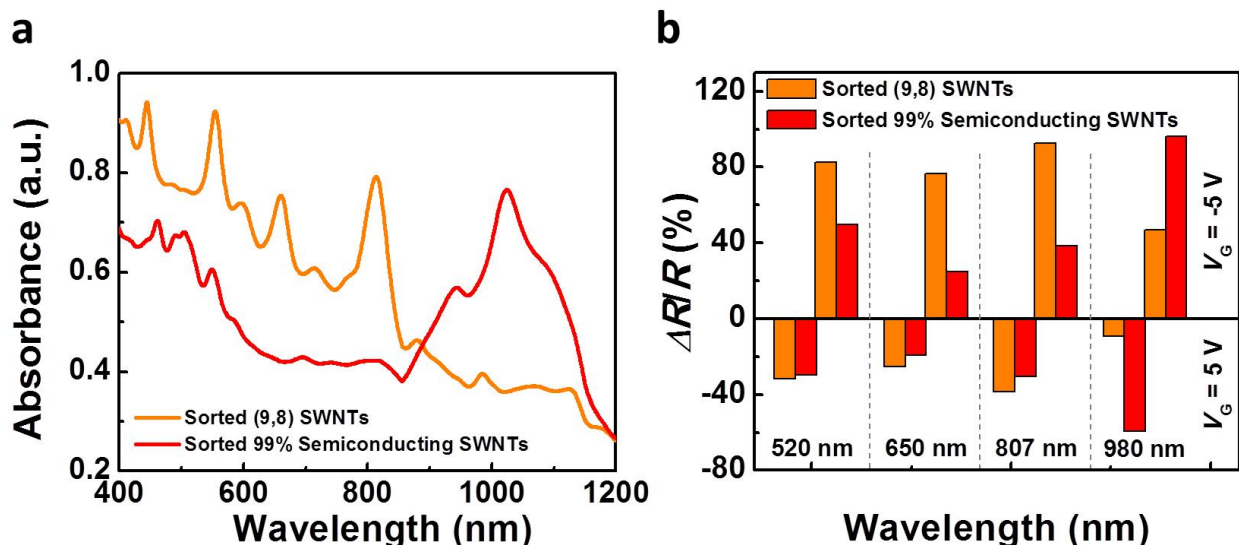


Figure 5.7 Wavelength-selectivity of the bolometric-effect-based photodetectors with different types of carbon nanotubes. (a) UV-Vis-NIR absorption spectra of two different types of SWCNTs, including single chirality (9,8) SWCNTs (orange) and 99% semiconductor-enriched SWCNTs from NanoIntegris, Inc. (red). (b) Photoresponse of devices made with the above two kinds of SWCNTs measured under different laser wavelengths of 520, 650, 807, and 980 nm. The histogram in the upper half of the graph corresponds to a $V_G = 5$ V and bottom half corresponds to a $V_G = -5$ V. Same as panel 4a, the orange columns and red columns correspond to (9,8) SWCNT sample and 99% semiconducting SWCNT sample, respectively.

5.4 Summary

To conclude, we successfully fabricate the fully printed thin film transistor based on SWNTs which exhibits good electrical characteristics. And the bolometric effects are observed for the transistors when shone by laser. Additionally, the transistors exhibit intriguing reliability under bending conditions owing to the ultrathin polyimide substrate as well as the superior mechanical flexibility of the gate dielectric and carbon nanotube network, which would

be beneficial for the development of ubiquitous, low-cost and large area flexible electronic systems.

Furthermore, we have demonstrated that by using two types of SWCNT samples with different optical absorption characteristics (a 99% semiconductor-enriched sample and a single chirality (9,8) carbon nanotube sample), the photoresponse exhibits a unique wavelength selectivity, as manifested by the good correlation between the responsive wavelengths of the devices with the absorption peaks of the corresponding carbon nanotubes.

CHAPTER 6

CONCLUSION AND FUTURE WORK

In this chapter, all the completed work would be concluded and several ideas for the potential future work would be proposed.

6.1 Summary of Thesis

Through this report, the author has demonstrated various flexible or stretchable sensors and displays including strain gauge, pressure sensors, stretchable electroluminescent displays, stretchable thin film transistors and photodetectors fabricated by the printing process.

By patterning the conventional non-stretchable materials Ag nanoparticles into serpentine structure, fully printed stretchable devices are achieved on the PUA substrate. And the performance of the devices is tunable by varying the radius of the serpentine pattern. The device with smaller radius had been demonstrated as a strain gauge to monitor the finger motion of human beings due to its high sensitivity to the strain while the device with larger radius had been demonstrated as a stretchable conductor to drive a conventional LED due to its higher stretchability.

By investigating the intrinsic stretchable materials AgNWs, we have developed the direct printing process to fabricate the stretchable conductors on various substrates including Si, glass, Polyimide, Polydimethylsiloxane (PDMS) and Very High Bond (VHB) tape. Systematic characterizations were performed to investigate the electrical and electromechanical properties of the printed features with different nanowire lengths. By printing the AgNWs on a bi-axially pre-stretched PDMS substrate, we have realized a stretchable conductor which can drive an LED under an area strain of up to 156% (256% of the original area). Additionally, using the printed parallel AgNW lines as electrodes and the elastic material Ecoflex as

the dielectric, we have demonstrated an ultrasensitive capacitive pressure sensor array, with which the pressure as low as 100 Pa is able to be detected. And with the pressure sensor array, we have also demonstrated the mapping results of 3D printed letter "M", "S", "U" and even a metal weight. More interestingly, by replacing the Ecoflex dielectric layer with a composite composed of PDMS and electroluminescent (EL) phosphors, we have demonstrated a printed stretchable EL display. Light with different color could be achieved by changing the type and concentration of dopants, and the display with "MSU" could withstand tensile strains up to 20% for more than 1000 cycles, albeit with noticeable degradation in luminance. Furthermore, the same strategy may be adapted to other material platforms like semiconducting nanowires, which may offer a cost-effective entry to various nanowire-based mechanically compliant sensory and optoelectronic systems.

Additionally, the intrinsically stretchable thin-film transistors (TFTs) and integrated logic circuits are reported by directly printing on elastomeric polydimethylsiloxane (PDMS) substrates. The printed devices utilize semiconductive type carbon nanotubes as the channel materials, metallic type carbon nanotubes as the electrode and a type of hybrid gate dielectric comprising PDMS and barium titanate (BaTiO_3) nanoparticles as the dielectric layer, all the components are intrinsically stretchable. As one of the key innovation, the BaTiO_3 /PDMS composite simultaneously provides high dielectric constant, superior stretchability, low leakage, as well as good printability and compatibility with the elastomeric substrate. And both the printed TFTs and logic circuits can be stretched beyond 50% strain along either channel length or channel width directions for thousands of cycles while showing no significant degradation in electrical performance. As the first reported fully printed intrinsically stretchable thin film transistors and logic circuits, this work may have broad prospects in stretchable electronics and offer an entry to more sophisticated stretchable electronic systems.

Finally, by applying the SWNTs as the channel layer of the thin film transistor, we successfully fabricate the fully printed flexible photodetector which exhibits good electrical characteristics. Additionally, the transistors exhibit intriguing reliability under bending con-

ditions owing to the ultrathin polyimide substrate as well as the superior mechanical flexibility of the gate dielectric and carbon nanotube network. Furthermore, we have demonstrated that by using two types of SWCNT samples with different optical absorption characteristics, the photoresponse exhibits unique wavelength selectivity, as manifested by the good correlation between the responsive wavelengths of the devices with the absorption peaks of the corresponding carbon nanotubes.

6.2 Future work

Based on the results achieved so far, several potential projects may be carried out for the next step. And they are listed as follows:

6.2.1 Human Motion Controlled Robotic System

Similarly to the strain sensor presented in Chapter 2, many different sensors have been developed to detect the human motion. For instance, Takeo Yamada [199] et al have demonstrated a strain sensor fabricated with carbon nanotube to detect the breathing, phonation, finger motion and knee bending. Jungjin Park [200] et al have adopted graphene strain sensors to detect the human motions including joint movement, phonation, swallowing, and breathing. And Shu Gong [201] et al have taken one step further by controlling the movement of a robotic arm with the strain sensors fabricated with the composite of Gold nanowires and polymer. As shown in Figure 6.1, the strain sensors are mounted in the finger joint location a smart glove which has been integrated with pre-programmed Graphical User Interface and a bluetooth radio on a chip. And after collecting the data from the strain sensor, the chip would transmit the data to a computer wirelessly to actuate the correspond motors in the robotic arm based on a thresholding algorithm. There are two motors (gripper motor and elbow motor) corresponding to four actions (gripper open/close, elbow up/down) that can be individually controlled by four different finger motions (the thumb finger:gripper close,

the index finger:gripper open, the middle finger:elbow down, the little finger:elbow up).

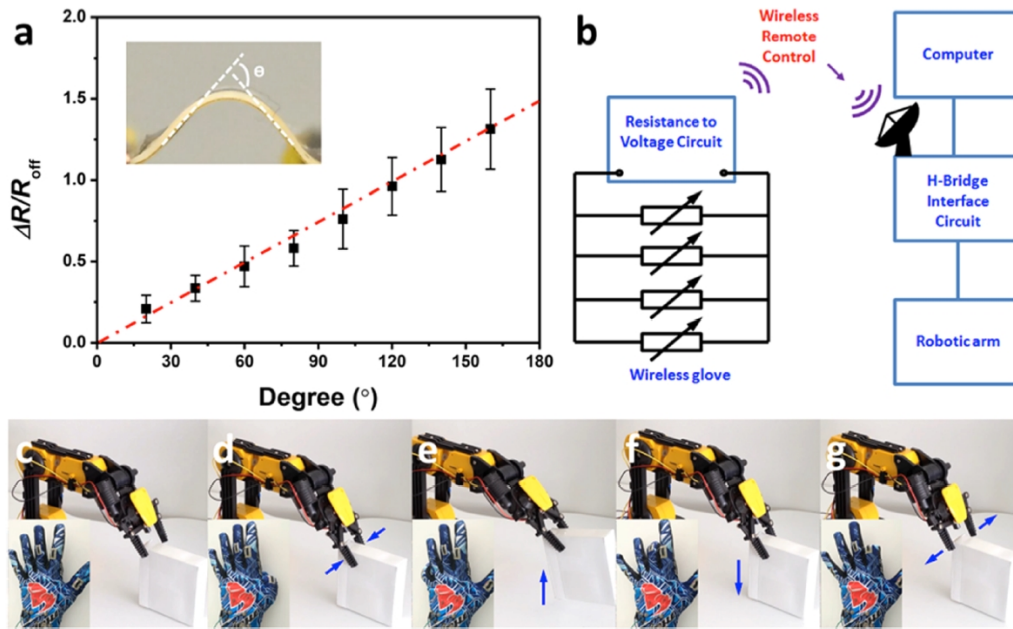


Figure 6.1 Reprint from ref [201], (a) Plot of resistance response as a function of bending degree for the flexion sensors. (b) Schematic diagram of the remote controlling configuration. (c-g) The whole process of the remote controlling performance of four flexion sensors sewed on a textile glove. Relaxed state (c) → clamping object (d) → lifting object up (e) → putting object down (f) → releasing object (g)

However, the gauge factor of the strain sensors in Shu Gong [201]’s work is below 15, while that of our strain sensor reported in Chapter 2 is as high as 10^6 , so for next step, we may investigate a smart glove by integrating our strain sensor and the microcontroller onto a glove. And instead of controlling the movement of the robotic arm with the pre-stored motion, we can control the robot to move synchronously with finger motion. And we may even be able to send the feedback signal to a smartphone and have a better control with a developed mobile app.

6.2.2 Real-time Monitoring of the Blood Pressure

It is important to monitor the perfusion of the circulation in a human body. Nowadays, We can easily monitor the blood perfusion in large vessels using a pulse rate monitor. Recently

Photoplethysmography (PPG) technology has been used to develop small, wearable, pulse rate sensors, which is consisting of infrared light-emitting diodes (LEDs) and photodetectors, offering a simple, reliable, low-cost means of monitoring the pulse rate noninvasively [202]. The principle behind PPG sensors is optical detection of blood volume changes in the microvascular bed of the tissue. The sensor system consists of a light source and a detector, with red and infrared (IR) light-emitting diodes (LEDs) commonly used as the light source. The PPG sensor monitors changes in the light intensity via reflection from or transmission through the tissue. The changes in light intensity are associated with small variations in blood perfusion of the tissue and provide information on the cardiovascular system, in particular, the pulse rate [203, 204, 205].

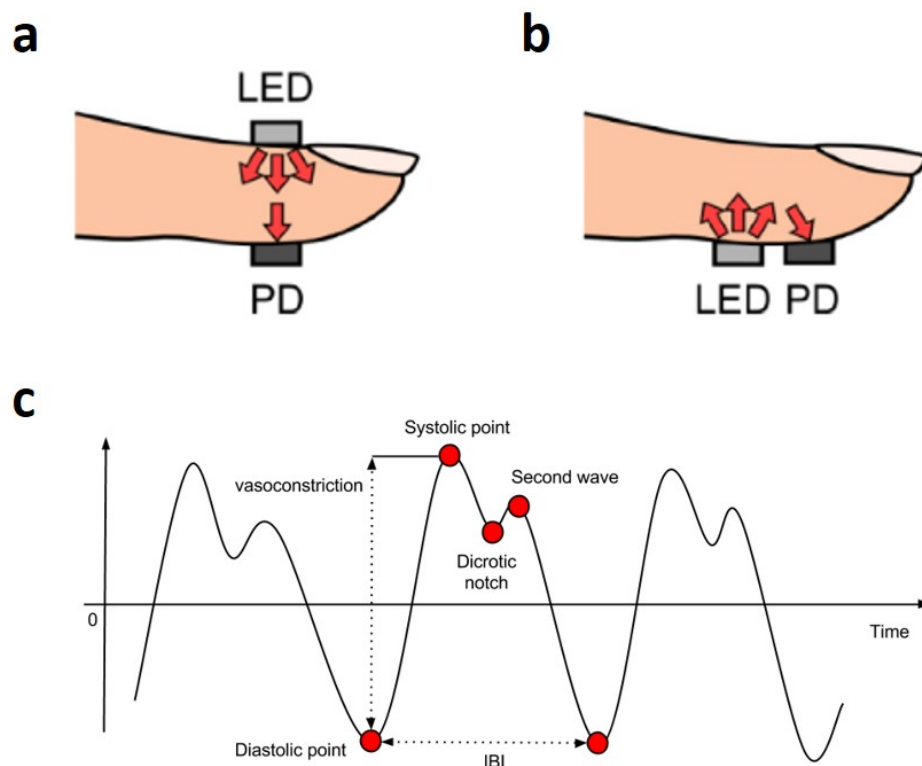


Figure 6.2 ref [202], (a) schematic of transmission mode PPG, (b) schematic of reflection mode PPG, (c) a representative PPG waveform

The wearable PPG has two modes—transmission and reflectance—as shown in Figure 6.2a and b, respectively. In transmission mode, the light transmitted through the medium is

detected by a PD opposite the LED source, while in reflectance mode, the PD detects light that is back-scattered or reflected from tissue, bone and/or blood vessels [202]. Figure 6.2c offers a representative PPG waveform.

Even though the real time monitoring of the pulse is achievable, the most important cardiopulmonary parameter is blood pressure, which is very sophisticated to monitor. L.Y. Chen et al [206] have presented a wireless, real-time pressure monitoring system with passive, flexible, millimeter-scale sensors to continuously monitor the blood pressure of an individual.

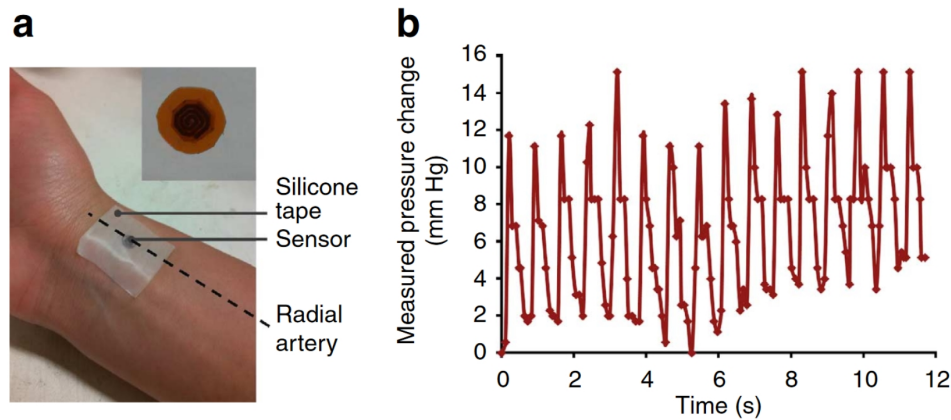


Figure 6.3 ref [206], (a) Placement of a modified $2.5 \times 2.5 \text{ mm}^2$ round sensor shown in inset on the radial artery of a human subject. (b) Measured pulse pressure waveform of a human subject with a heart rate of 82 b.p.m. over 12s period with a time resolution of 90 ms.

As shown in Figure 6.3a, a round $2.5 \times 2.5 \text{ mm}^2$ sensor device was placed on the radial artery of a healthy adult male subject and secured by the silicone tape. The pressure waveform was measured and wirelessly transformed with the readout antenna placed directly above the surface sensor in real time. As shown in Figure 6.3b, the measured waveform clearly indicates a steady pulse of about 82 b.p.m, and the characteristic pulse waveform shape can be obtained the peak systolic wave followed by the dicrotic notch, the latter related to the aortic valve closure [207].

For next step, we may achieve the low cost blood pressure monitoring sensor with the pressure sensor developed in Chapter 3. And we can also develop the mobile app and integrate it together with the sensor to form a more complete, low-cost and easy-fabricated

real-time blood pressure monitoring system.

6.2.3 Stretchable System Integrated by Sensors and Displays

Future electronics will be highly deformable and will adapt their shapes by stretching, shrinking, and wrinkling as desired. Imagine if smart watches were substituted by stretchable membranes which can be wrapped around the wrist, detecting and offering a constant stream of activity and healthy data that would undoubtedly be more accurate than the bulky sensors, or if mobile phones and tablets were able to be stretched up to the desired size without losing resolution, or if the internal medical devices grew and moved along with their hosts. That would be huge. Report released by Research and Markets recently forecasts that stretchable electronics will be worth more than \$900 million by 2023, which would be opportunities as well as challenges. And by then, the stretchable electronics would not be limited as single components such as electrodes, simple conductors and dielectrics or devices such as thin film transistors, diodes and solar cells. Instead, the stretchable electronics would bring in an integration of devices, interconnects and functional sections to form a stretchable interactive system.

C. Wang et al [208] have developed a flexible electronic system, which have the flexible transistors, OLED display and pressure sensors integrated. As shown in Figure 6.4a and b, an array of the display pixel are fabricated on a super-thin and flexible Polyimide substrate, resulting in a flexible display. And by evaporating OLED materials with different type of emissive layers, a green color display (Figure 6.4c) and a full color display (Figure 6.4d) have been achieved. And Figure 6.4e shows the full-colour display being fully turned on in bent states, with a pixel yield of $\sim 85\%$, confirming that the OLED and metal thin film in the display array are durable on bending. And by laminating the PSR layer on top of the whole array, a 16×16 pixel arrays of display integrated with the pressure sensor are demonstrated, the circuit schematic has been illustrated in Figure 6.4f. The PSR is connected to each pixel through the LiF/Al cathode of the underlying AMOLED. The top surface of the PSR is

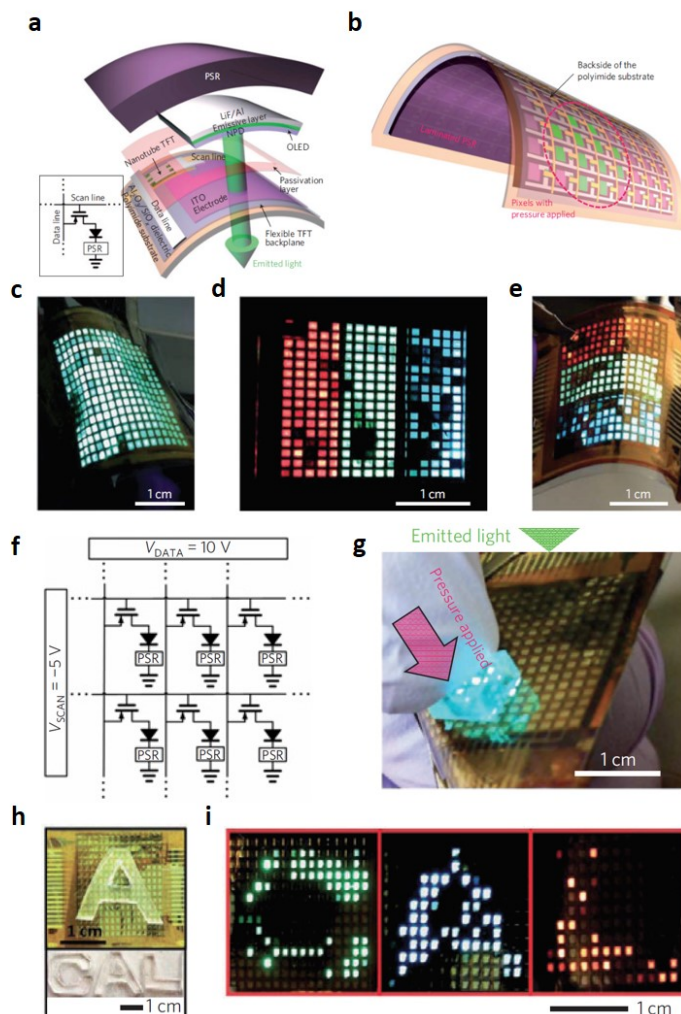


Figure 6.4 Reprint from ref [208], (a)Schematic layout of a single pixel, consisting of a nanotube TFT, an OLED and a pressure sensor (PSR) integrated vertically on a polyimide substrate. (b)Schematic diagram of an array of pixels (16×16) functioning as an interactive e-skin, capable of spatially mapping and visually displaying an applied pressure profile. (c)Photo of a single-colour (green) AMOLED being fully turned on and bent. Voltages of -5 and 10 V are applied to all of the scan and data lines, respectively. The pixel yield, as defined by the percentage of OLEDs in the matrix that emit light, is higher than 97%. (d)Photograph of a full-colour (red, green, blue) AMOLED display with all pixels being turned on. (e)Photo of the same full-colour display shown in d being bent. (f)Circuit schematic of the e-skin matrix. (g)Photograph of a fabricated device, showing that light is locally emitted where the surface is touched. Only the pixels being pressed are turned on. (h)PDMS slabs with C, A, and L shapes are prepared and used to apply pressure onto the sensor array. (i)Green, blue and red colour interactive e-skins are used to spatially map and display the pressure applied with C- (left), A- (centre) and L- (right) shaped PDMS slabs, respectively

coated with conductive silver ink as the ground electrode. Upon pressure, the PSR would transit from insulating to conducting, resulting in the current flow through the OLED and having the light emitting. And in Figure 6.4i, e-skin devices with green, blue and red color OLEDs are used to map and display the C-, A- and L-shaped PDMS slabs, respectively. Applying pressure through the letter-shaped PDMS slabs produces recognizable letters with good spatial resolution [208].

Similarly to C.Wang' work [208], Figure 6.5 demonstrates a concept stretchable systems consist of printed OLED and various sensors, their driving TFTs and the functional stretchable photovoltaics (PV) on a stretchable substrate, rather than flexible substrate. Here, the sensors could be used to detect pressure, temperature, strain or photons, while OLED could also be replaced with other display components, as long as they are stretchable. Such stretchable systems integrated by displays, sensors and power devices have many potential applications. For instance, it could be used as a self-powered monitor system for peoples health with all the sensors detecting the vital signal of the patient and supplying real-time and intuitive results displayed on the screen.

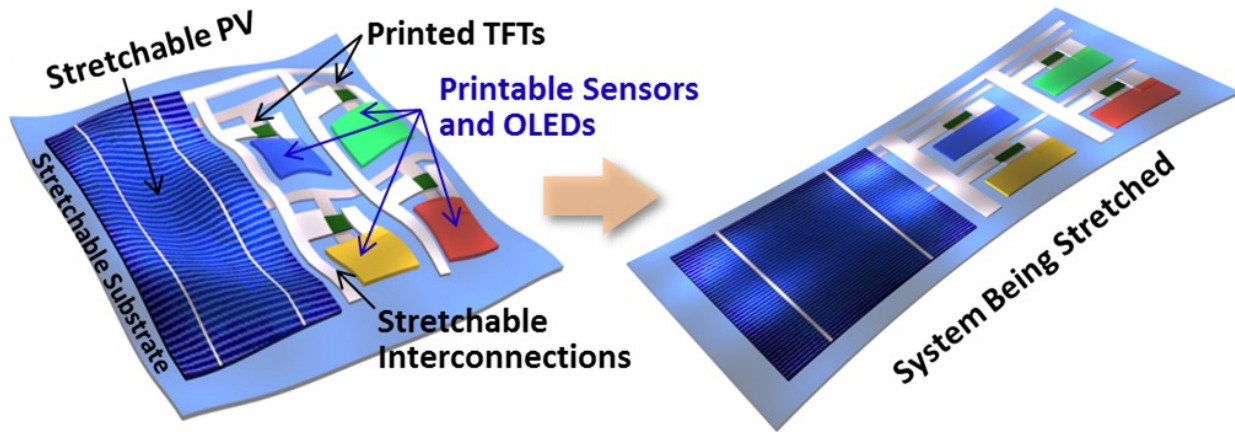


Figure 6.5 Schematic for a conceptual stretchable electronics system.

Stretchable electronics, which might be the next revolutionary technology, is going to change the way how we live.

BIBLIOGRAPHY

BIBLIOGRAPHY

- [1] T. Someya, *Stretchable electronics*. John Wiley & Sons, 2012.
- [2] D. Shavit, “The developments of leds and smd electronics on transparent conductive polyester film,” *Vacuum International*, 2007.
- [3] D. Kuang, J. Brilliet, P. Chen, M. Takata, S. Uchida, H. Miura, K. Sumioka, S. M. Zakeeruddin, and M. Gratzel, “Application of highly ordered tio2 nanotube arrays in flexible dye-sensitized solar cells,” *ACS nano*, vol. 2, no. 6, pp. 1113–1116, 2008.
- [4] A. Sugimoto, H. Ochi, S. Fujimura, A. Yoshida, T. Miyadera, and M. Tsuchida, “Flexible oled displays using plastic substrates,” *IEEE Journal of selected topics in quantum electronics*, vol. 10, no. 1, pp. 107–114, 2004.
- [5] L. E. Tannas, *Flat-panel displays and CRTs*. Springer Science & Business Media, 2012.
- [6] H. Hasegawa, I. M. Rahman, Y. Umehara, H. Sawai, T. Maki, Y. Furusho, and S. Mizutani, “Selective recovery of indium from the etching waste solution of the flat-panel display fabrication process,” *Microchemical Journal*, vol. 110, pp. 133–139, 2013.
- [7] T. N. Jackson, Y.-Y. Lin, D. J. Gundlach, and H. Klauk, “Organic thin-film transistors for organic light-emitting flat-panel display backplanes,” *IEEE Journal of selected topics in quantum electronics*, vol. 4, no. 1, pp. 100–104, 1998.
- [8] V. Bhateja, H. Patel, A. Krishn, A. Sahu, and A. Lay-Ekuakille, “Multimodal medical image sensor fusion framework using cascade of wavelet and contourlet transform domains,” *IEEE Sensors Journal*, vol. 15, no. 12, pp. 6783–6790, 2015.
- [9] A. P. James and B. V. Dasarathy, “Medical image fusion: A survey of the state of the art,” *Information Fusion*, vol. 19, pp. 4–19, 2014.
- [10] P.-C. Chang, S.-Y. Chou, and K.-K. Shieh, “Reading performance and visual fatigue when using electronic paper displays in long-duration reading tasks under various lighting conditions,” *Displays*, vol. 34, no. 3, pp. 208–214, 2013.
- [11] X. Wang, L. Wang, J. Sun, A. K. Srivastava, V. G. Chigrinov, and H. S. Kwok, “Autostereoscopic 3d pictures on optically rewritable electronic paper,” *Journal of the Society for Information Display*, vol. 21, no. 2, pp. 103–107, 2013.
- [12] BGR, “Is samsung going to launch the bendable galaxy x phone soon?,” 2017. [Online; accessed 25-September-2017].
- [13] K. Jost, D. Stenger, C. R. Perez, J. K. McDonough, K. Lian, Y. Gogotsi, and G. Dion, “Knitted and screen printed carbon-fiber supercapacitors for applications in wearable electronics,” *Energy & Environmental Science*, vol. 6, no. 9, pp. 2698–2705, 2013.

- [14] L. Kou, T. Huang, B. Zheng, Y. Han, X. Zhao, K. Gopalsamy, H. Sun, and C. Gao, “Coaxial wet-spun yarn supercapacitors for high-energy density and safe wearable electronics,” *Nature communications*, vol. 5, 2014.
- [15] M. Stoppa and A. Chiolerio, “Wearable electronics and smart textiles: a critical review,” *Sensors*, vol. 14, no. 7, pp. 11957–11992, 2014.
- [16] W. Zeng, L. Shu, Q. Li, S. Chen, F. Wang, and X.-M. Tao, “Fiber-based wearable electronics: a review of materials, fabrication, devices, and applications,” *Advanced Materials*, vol. 26, no. 31, pp. 5310–5336, 2014.
- [17] J. Kim, M. Lee, H. J. Shim, R. Ghaffari, H. R. Cho, D. Son, Y. H. Jung, M. Soh, C. Choi, S. Jung, *et al.*, “Stretchable silicon nanoribbon electronics for skin prosthesis,” *Nature communications*, vol. 5, p. 5747, 2014.
- [18] W.-H. Yeo, Y.-S. Kim, J. Lee, A. Ameen, L. Shi, M. Li, S. Wang, R. Ma, S. H. Jin, Z. Kang, *et al.*, “Multifunctional epidermal electronics printed directly onto the skin,” *Advanced Materials*, vol. 25, no. 20, pp. 2773–2778, 2013.
- [19] S. Bauer and M. Kaltenbrunner, “Materials science: Semiconductors that stretch and heal,” *Nature*, vol. 539, no. 7629, pp. 365–367, 2016.
- [20] D. Son, J. Lee, S. Qiao, R. Ghaffari, J. Kim, J. E. Lee, C. Song, S. J. Kim, D. J. Lee, S. W. Jun, *et al.*, “Multifunctional wearable devices for diagnosis and therapy of movement disorders,” *Nature nanotechnology*, vol. 9, no. 5, pp. 397–404, 2014.
- [21] A. Chortos, J. Liu, and Z. Bao, “Pursuing prosthetic electronic skin,” *Nature materials*, 2016.
- [22] J. Kim, M. Lee, H. J. Shim, R. Ghaffari, H. R. Cho, D. Son, Y. H. Jung, M. Soh, C. Choi, S. Jung, *et al.*, “Stretchable silicon nanoribbon electronics for skin prosthesis,” *Nature communications*, vol. 5, p. 5747, 2014.
- [23] H. Ohmae, Y. Tomita, M. Kasahara, J. Schram, E. Smits, J. Van den Brand, F. Bossuyt, J. Vanfleteren, and J. De Baets, “9.4: Stretchable 45× 80 rgb led display using meander wiring technology,” in *SID Symposium Digest of Technical Papers*, vol. 46, pp. 102–105, Wiley Online Library, 2015.
- [24] J. Ge, L. Sun, F.-R. Zhang, Y. Zhang, L.-A. Shi, H.-Y. Zhao, H.-W. Zhu, H.-L. Jiang, and S.-H. Yu, “A stretchable electronic fabric artificial skin with pressure-, lateral strain-, and flexion-sensitive properties,” *Advanced Materials*, vol. 28, no. 4, pp. 722–728, 2016.
- [25] C. Hua, Y. Shang, X. Li, X. Hu, Y. Wang, X. Wang, Y. Zhang, X. Li, H. Duan, and A. Cao, “Helical graphene oxide fibers as a stretchable sensor and an electrocapillary sucker,” *Nanoscale*, vol. 8, no. 20, pp. 10659–10668, 2016.
- [26] C. Hu and L. Dai, “Carbon-based metal-free catalysts for electrocatalysis beyond the orr,” *Angewandte Chemie International Edition*, 2016.

- [27] T. Someya, Y. Kato, T. Sekitani, S. Iba, Y. Noguchi, Y. Murase, H. Kawaguchi, and T. Sakurai, “Conformable, flexible, large-area networks of pressure and thermal sensors with organic transistor active matrixes,” *Proceedings of the National Academy of Sciences of the United States of America*, vol. 102, no. 35, pp. 12321–12325, 2005.
- [28] D.-Y. Khang, H. Jiang, Y. Huang, and J. A. Rogers, “A stretchable form of single-crystal silicon for high-performance electronics on rubber substrates,” *Science*, vol. 311, no. 5758, pp. 208–212, 2006.
- [29] S. Y. Ryu, J. Xiao, W. I. Park, K. S. Son, Y. Y. Huang, U. Paik, and J. A. Rogers, “Lateral buckling mechanics in silicon nanowires on elastomeric substrates,” *Nano letters*, vol. 9, no. 9, pp. 3214–3219, 2009.
- [30] D.-Y. Khang, J. Xiao, C. Kocabas, S. MacLaren, T. Banks, H. Jiang, Y. Y. Huang, and J. A. Rogers, “Molecular scale buckling mechanics in individual aligned single-wall carbon nanotubes on elastomeric substrates,” *Nano letters*, vol. 8, no. 1, pp. 124–130, 2008.
- [31] M. Gonzalez, F. Axisa, M. V. Bulcke, D. Brosteaux, B. Vandeveldel, and J. Vanfleteren, “Design of metal interconnects for stretchable electronic circuits,” *Microelectronics Reliability*, vol. 48, no. 6, pp. 825–832, 2008.
- [32] R. J. Jackman, S. T. Brittain, A. Adams, M. G. Prentiss, and G. M. Whitesides, “Design and fabrication of topologically complex, three-dimensional microstructures,” *Science*, vol. 280, no. 5372, pp. 2089–2091, 1998.
- [33] Y.-C. Chen, R. J. Young, J. V. Macpherson, and N. R. Wilson, “Single-walled carbon nanotube networks decorated with silver nanoparticles: a novel graded sers substrate,” *The Journal of Physical Chemistry C*, vol. 111, no. 44, pp. 16167–16173, 2007.
- [34] J. Lin, C. He, Y. Zhao, and S. Zhang, “One-step synthesis of silver nanoparticles/carbon nanotubes/chitosan film and its application in glucose biosensor,” *Sensors and Actuators B: Chemical*, vol. 137, no. 2, pp. 768–773, 2009.
- [35] J. Hwang, J. Jang, K. Hong, K. N. Kim, J. H. Han, K. Shin, and C. E. Park, “Poly (3-hexylthiophene) wrapped carbon nanotube/poly (dimethylsiloxane) composites for use in finger-sensing piezoresistive pressure sensors,” *Carbon*, vol. 49, no. 1, pp. 106–110, 2011.
- [36] J. Lu, M. Lu, A. Bermak, and Y.-K. Lee, “Study of piezoresistance effect of carbon nanotube-pdms composite materials for nanosensors,” in *Nanotechnology, 2007. IEEE-NANO 2007. 7th IEEE Conference on*, pp. 1240–1243, IEEE, 2007.
- [37] W.-Y. Wu, Z.-P. Bian, W. Wang, and J.-J. Zhu, “Pdms gold nanoparticle composite film-based silver enhanced colorimetric detection of cardiac troponin i,” *Sensors and Actuators B: Chemical*, vol. 147, no. 1, pp. 298–303, 2010.

- [38] Q. Zhang, J.-J. Xu, Y. Liu, and H.-Y. Chen, “In-situ synthesis of poly (dimethylsiloxane)–gold nanoparticles composite films and its application in microfluidic systems,” *Lab on a Chip*, vol. 8, no. 2, pp. 352–357, 2008.
- [39] M. Amjadi, A. Pichitpajongkit, S. Lee, S. Ryu, and I. Park, “Highly stretchable and sensitive strain sensor based on silver nanowire–elastomer nanocomposite,” *ACS nano*, vol. 8, no. 5, pp. 5154–5163, 2014.
- [40] T. Sekitani, Y. Noguchi, K. Hata, T. Fukushima, T. Aida, and T. Someya, “A rubberlike stretchable active matrix using elastic conductors,” *Science*, vol. 321, no. 5895, pp. 1468–1472, 2008.
- [41] K.-Y. Chun, Y. Oh, J. Rho, J.-H. Ahn, Y.-J. Kim, H. R. Choi, and S. Baik, “Highly conductive, printable and stretchable composite films of carbon nanotubes and silver,” *Nature nanotechnology*, vol. 5, no. 12, pp. 853–857, 2010.
- [42] A. Blayo and B. Pineaux, “Printing processes and their potential for rfid printing,” in *Proceedings of the 2005 joint conference on Smart objects and ambient intelligence: innovative context-aware services: usages and technologies*, pp. 27–30, ACM, 2005.
- [43] J. R. Sheats, “Manufacturing and commercialization issues in organic electronics,” *Journal of Materials Research*, vol. 19, no. 7, pp. 1974–1989, 2004.
- [44] I. Label-Aid Systems, “Flexographic label printing,” 2016-2018. [Online;].
- [45] H. Kipphan, *Handbook of print media: technologies and production methods*. Springer Science & Business Media, 2001.
- [46] E. GmbH, “Gravure printing,” 2013. [Online;].
- [47] A. Reddy, B. B. Narakathu, M. Atashbar, M. Rebros, E. Hrehorova, and M. Joyce, “Printed electrochemical based biosensors on flexible substrates,” in *Sensors, 2010 IEEE*, pp. 1596–1600, IEEE, 2010.
- [48] H. Kipphan, *Handbook of print media: technologies and production methods*. Springer Science & Business Media, 2001.
- [49] H. A. of German Research Centres, “Inkjet printing process for kesterite solar cells,” 2015. [Online;].
- [50] N. J. Nielsen, “History of thinkjet printhead development,” *Hewlett-Packard Journal*, vol. 36, no. 5, pp. 4–10, 1985.
- [51] D.-H. Kim, R. Ghaffari, N. Lu, and J. A. Rogers, “Flexible and stretchable electronics for biointegrated devices,” *Annual review of biomedical engineering*, vol. 14, pp. 113–128, 2012.

- [52] R. Okumura, S. Takamatsu, E. Iwase, K. Matsumoto, and I. Shimoyama, “Solution electrochemiluminescent microfluidic cell for flexible and stretchable display,” in *Micro Electro Mechanical Systems, 2009. MEMS 2009. IEEE 22nd International Conference on*, pp. 947–950, IEEE, 2009.
- [53] S. Yao and Y. Zhu, “Wearable multifunctional sensors using printed stretchable conductors made of silver nanowires,” *Nanoscale*, vol. 6, no. 4, pp. 2345–2352, 2014.
- [54] T. Sekitani, H. Nakajima, H. Maeda, T. Fukushima, T. Aida, K. Hata, and T. Someya, “Stretchable active-matrix organic light-emitting diode display using printable elastic conductors,” *Nature materials*, vol. 8, no. 6, pp. 494–499, 2009.
- [55] J. Liang, L. Li, K. Tong, Z. Ren, W. Hu, X. Niu, Y. Chen, and Q. Pei, “Silver nanowire percolation network soldered with graphene oxide at room temperature and its application for fully stretchable polymer light-emitting diodes,” *ACS nano*, vol. 8, no. 2, pp. 1590–1600, 2014.
- [56] J. Liang, K. Tong, and Q. Pei, “A water-based silver-nanowire screen-print ink for the fabrication of stretchable conductors and wearable thin-film transistors,” *Advanced Materials*, vol. 28, no. 28, pp. 5986–5996, 2016.
- [57] S. Shang, W. Zeng, and X.-m. Tao, “High stretchable mwnts/polyurethane conductive nanocomposites,” *Journal of Materials Chemistry*, vol. 21, no. 20, pp. 7274–7280, 2011.
- [58] P. Lee, J. Lee, H. Lee, J. Yeo, S. Hong, K. H. Nam, D. Lee, S. S. Lee, and S. H. Ko, “Highly stretchable and highly conductive metal electrode by very long metal nanowire percolation network,” *Advanced materials*, vol. 24, no. 25, pp. 3326–3332, 2012.
- [59] L. Cai and C. Wang, “Carbon nanotube flexible and stretchable electronics,” *Nanoscale research letters*, vol. 10, no. 1, p. 320, 2015.
- [60] A. Nathan, A. Ahnood, M. T. Cole, S. Lee, Y. Suzuki, P. Hiralal, F. Bonaccorso, T. Hasan, L. Garcia-Gancedo, A. Dyadyusha, *et al.*, “Flexible electronics: the next ubiquitous platform,” *Proceedings of the IEEE*, vol. 100, no. Special Centennial Issue, pp. 1486–1517, 2012.
- [61] M. Amjadi, K.-U. Kyung, I. Park, and M. Sitti, “Stretchable, skin-mountable, and wearable strain sensors and their potential applications: A review,” *Advanced Functional Materials*, vol. 26, no. 11, pp. 1678–1698, 2016.
- [62] M. Amjadi, Y. J. Yoon, and I. Park, “Ultra-stretchable and skin-mountable strain sensors using carbon nanotubes–ecoflex nanocomposites,” *Nanotechnology*, vol. 26, no. 37, p. 375501, 2015.
- [63] N. Matsuhisa, M. Kaltenbrunner, T. Yokota, H. Jinno, K. Kuribara, T. Sekitani, and T. Someya, “Printable elastic conductors with a high conductivity for electronic textile applications,” *Nature communications*, vol. 6, 2015.

- [64] J. J. Park, W. J. Hyun, S. C. Mun, Y. T. Park, and O. O. Park, “Highly stretchable and wearable graphene strain sensors with controllable sensitivity for human motion monitoring,” *ACS applied materials & interfaces*, vol. 7, no. 11, pp. 6317–6324, 2015.
- [65] S. Ryu, P. Lee, J. B. Chou, R. Xu, R. Zhao, A. J. Hart, and S.-G. Kim, “Extremely elastic wearable carbon nanotube fiber strain sensor for monitoring of human motion,” *ACS nano*, vol. 9, no. 6, pp. 5929–5936, 2015.
- [66] T. Q. Trung and N.-E. Lee, “Flexible and stretchable physical sensor integrated platforms for wearable human-activity monitoring and personal healthcare,” *Advanced materials*, vol. 28, no. 22, pp. 4338–4372, 2016.
- [67] T. Yamada, Y. Hayamizu, Y. Yamamoto, Y. Yomogida, A. Izadi-Najafabadi, D. N. Futaba, and K. Hata, “A stretchable carbon nanotube strain sensor for human-motion detection,” *Nature nanotechnology*, vol. 6, no. 5, pp. 296–301, 2011.
- [68] C. Keplinger, J.-Y. Sun, C. C. Foo, P. Rothemund, G. M. Whitesides, and Z. Suo, “Stretchable, transparent, ionic conductors,” *Science*, vol. 341, no. 6149, pp. 984–987, 2013.
- [69] K. Xie and B. Wei, “Materials and structures for stretchable energy storage and conversion devices,” *Advanced Materials*, vol. 26, no. 22, pp. 3592–3617, 2014.
- [70] C. Yan and P. S. Lee, “Stretchable energy storage and conversion devices,” *Small*, vol. 10, no. 17, pp. 3443–3460, 2014.
- [71] M. Kaltenbrunner, T. Sekitani, J. Reeder, T. Yokota, K. Kuribara, T. Tokuhara, M. Drack, R. Schwödiauer, I. Graz, S. Bauer-Gogonea, *et al.*, “An ultra-lightweight design for imperceptible plastic electronics,” *Nature*, vol. 499, no. 7459, pp. 458–463, 2013.
- [72] S. Rosset and H. R. Shea, “Flexible and stretchable electrodes for dielectric elastomer actuators,” *Applied Physics A*, vol. 110, no. 2, pp. 281–307, 2013.
- [73] Y. Kim, J. Zhu, B. Yeom, M. Di Prima, X. Su, J.-G. Kim, S. J. Yoo, C. Uher, and N. A. Kotov, “Stretchable nanoparticle conductors with self-organized conductive pathways,” *Nature*, vol. 500, no. 7460, pp. 59–63, 2013.
- [74] M. Zu, Q. Li, G. Wang, J.-H. Byun, and T.-W. Chou, “Carbon nanotube fiber based stretchable conductor,” *Advanced Functional Materials*, vol. 23, no. 7, pp. 789–793, 2013.
- [75] D. J. Lipomi, B. C.-K. Tee, M. Vosgueritchian, and Z. Bao, “Stretchable organic solar cells,” *Advanced Materials*, vol. 23, no. 15, pp. 1771–1775, 2011.
- [76] D. J. Lipomi, J. A. Lee, M. Vosgueritchian, B. C.-K. Tee, J. A. Bolander, and Z. Bao, “Electronic properties of transparent conductive films of PEDOT:PSS on stretchable substrates,” *Chemistry of Materials*, vol. 24, no. 2, pp. 373–382, 2012.

- [77] M. Vosgueritchian, D. J. Lipomi, and Z. Bao, “Highly conductive and transparent pedot: Pss films with a fluorosurfactant for stretchable and flexible transparent electrodes,” *Advanced functional materials*, vol. 22, no. 2, pp. 421–428, 2012.
- [78] T. S. Hansen, K. West, O. Hassager, and N. B. Larsen, “Highly stretchable and conductive polymer material made from poly (3, 4-ethylenedioxythiophene) and polyurethane elastomers,” *Advanced functional materials*, vol. 17, no. 16, pp. 3069–3073, 2007.
- [79] K. Takei, Z. Yu, M. Zheng, H. Ota, T. Takahashi, and A. Javey, “Highly sensitive electronic whiskers based on patterned carbon nanotube and silver nanoparticle composite films,” *Proceedings of the National Academy of Sciences*, vol. 111, no. 5, pp. 1703–1707, 2014.
- [80] C. Yu, C. Masarapu, J. Rong, B. Wei, and H. Jiang, “Stretchable supercapacitors based on buckled single-walled carbon-nanotube macrofilms,” *Advanced Materials*, vol. 21, no. 47, pp. 4793–4797, 2009.
- [81] T. Kim, H. Song, J. Ha, S. Kim, D. Kim, S. Chung, J. Lee, and Y. Hong, “Inkjet-printed stretchable single-walled carbon nanotube electrodes with excellent mechanical properties,” *Applied Physics Letters*, vol. 104, no. 11, p. 113103, 2014.
- [82] U.-H. Shin, D.-W. Jeong, S.-H. Kim, H. W. Lee, and J.-M. Kim, “Elastomer-infiltrated vertically aligned carbon nanotube film-based wavy-configured stretchable conductors,” *ACS applied materials & interfaces*, vol. 6, no. 15, pp. 12909–12914, 2014.
- [83] S. Chung, J. Lee, H. Song, S. Kim, J. Jeong, and Y. Hong, “Inkjet-printed stretchable silver electrode on wave structured elastomeric substrate,” *Applied Physics Letters*, vol. 98, no. 15, p. 153110, 2011.
- [84] F. Xu and Y. Zhu, “Highly conductive and stretchable silver nanowire conductors,” *Advanced materials*, vol. 24, no. 37, pp. 5117–5122, 2012.
- [85] J. Ge, H.-B. Yao, X. Wang, Y.-D. Ye, J.-L. Wang, Z.-Y. Wu, J.-W. Liu, F.-J. Fan, H.-L. Gao, C.-L. Zhang, *et al.*, “Stretchable conductors based on silver nanowires: improved performance through a binary network design,” *Angewandte Chemie*, vol. 125, no. 6, pp. 1698–1703, 2013.
- [86] H.-L. Gao, L. Xu, F. Long, Z. Pan, Y.-X. Du, Y. Lu, J. Ge, and S.-H. Yu, “Macroscopic free-standing hierarchical 3d architectures assembled from silver nanowires by ice templating,” *Angewandte Chemie International Edition*, vol. 53, no. 18, pp. 4561–4566, 2014.
- [87] C. Yan, J. Wang, X. Wang, W. Kang, M. Cui, C. Y. Foo, and P. S. Lee, “An intrinsically stretchable nanowire photodetector with a fully embedded structure,” *Advanced Materials*, vol. 26, no. 6, pp. 943–950, 2014.
- [88] D.-H. Kim, Z. Liu, Y.-S. Kim, J. Wu, J. Song, H.-S. Kim, Y. Huang, K.-c. Hwang, Y. Zhang, and J. A. Rogers, “Optimized structural designs for stretchable silicon integrated circuits,” *Small*, vol. 5, no. 24, pp. 2841–2847, 2009.

- [89] M. Su, F. Li, S. Chen, Z. Huang, M. Qin, W. Li, X. Zhang, and Y. Song, “Nanoparticle based curve arrays for multirecognition flexible electronics,” *Advanced Materials*, vol. 28, no. 7, pp. 1369–1374, 2016.
- [90] S. Lee, S. Kim, T.-T. Kim, Y. Kim, M. Choi, S. H. Lee, J.-Y. Kim, and B. Min, “Reversibly stretchable and tunable terahertz metamaterials with wrinkled layouts,” *Advanced Materials*, vol. 24, no. 26, pp. 3491–3497, 2012.
- [91] F. Xu, J. W. Durham III, B. J. Wiley, and Y. Zhu, “Strain-release assembly of nanowires on stretchable substrates,” *ACS nano*, vol. 5, no. 2, pp. 1556–1563, 2011.
- [92] M. Kaltenbrunner, M. S. White, E. D. Głowacki, T. Sekitani, T. Someya, N. S. Sariciftci, and S. Bauer, “Ultrathin and lightweight organic solar cells with high flexibility,” *Nature communications*, vol. 3, p. 770, 2012.
- [93] S. Xu, Y. Zhang, J. Cho, J. Lee, X. Huang, L. Jia, J. A. Fan, Y. Su, J. Su, H. Zhang, *et al.*, “Stretchable batteries with self-similar serpentine interconnects and integrated wireless recharging systems,” *Nature communications*, vol. 4, p. 1543, 2013.
- [94] S. Yang, E. Ng, and N. Lu, “Indium tin oxide (ito) serpentine ribbons on soft substrates stretched beyond 100%,” *Extreme Mechanics Letters*, vol. 2, pp. 37–45, 2015.
- [95] S. R. Forrest, “The path to ubiquitous and low-cost organic electronic appliances on plastic,” *Nature*, vol. 428, no. 6986, pp. 911–918, 2004.
- [96] H. Sirringhaus, T. Kawase, R. Friend, T. Shimoda, M. Inbasekaran, W. Wu, and E. Woo, “High-resolution inkjet printing of all-polymer transistor circuits,” *Science*, vol. 290, no. 5499, pp. 2123–2126, 2000.
- [97] M. Singh, H. M. Haverinen, P. Dhagat, and G. E. Jabbour, “Inkjet printing process and its applications,” *Advanced materials*, vol. 22, no. 6, pp. 673–685, 2010.
- [98] S. Baruah, C. Thanachayanont, and J. Dutta, “Growth of zno nanowires on nonwoven polyethylene fibers,” *Science and Technology of Advanced Materials*, vol. 9, no. 2, p. 025009, 2008.
- [99] J. A. Rogers, T. Someya, and Y. Huang, “Materials and mechanics for stretchable electronics,” *Science*, vol. 327, no. 5973, pp. 1603–1607, 2010.
- [100] K.-Y. Chun, Y. Oh, J. Rho, J.-H. Ahn, Y.-J. Kim, H. R. Choi, and S. Baik, “Highly conductive, printable and stretchable composite films of carbon nanotubes and silver,” *Nature nanotechnology*, vol. 5, no. 12, pp. 853–857, 2010.
- [101] T. Sekitani, Y. Noguchi, K. Hata, T. Fukushima, T. Aida, and T. Someya, “A rubberlike stretchable active matrix using elastic conductors,” *Science*, vol. 321, no. 5895, pp. 1468–1472, 2008.

- [102] S. Bae, H. Kim, Y. Lee, X. Xu, J.-S. Park, Y. Zheng, J. Balakrishnan, T. Lei, H. R. Kim, Y. I. Song, *et al.*, “Roll-to-roll production of 30-inch graphene films for transparent electrodes,” *Nature nanotechnology*, vol. 5, no. 8, pp. 574–578, 2010.
- [103] P. Lee, J. Lee, H. Lee, J. Yeo, S. Hong, K. H. Nam, D. Lee, S. S. Lee, and S. H. Ko, “Highly stretchable and highly conductive metal electrode by very long metal nanowire percolation network,” *Advanced materials*, vol. 24, no. 25, pp. 3326–3332, 2012.
- [104] F. Xu and Y. Zhu, “Highly conductive and stretchable silver nanowire conductors,” *Advanced materials*, vol. 24, no. 37, pp. 5117–5122, 2012.
- [105] D. J. Lipomi, J. A. Lee, M. Vosgueritchian, B. C.-K. Tee, J. A. Bolander, and Z. Bao, “Electronic properties of transparent conductive films of PEDOT:PSS on stretchable substrates,” *Chemistry of Materials*, vol. 24, no. 2, pp. 373–382, 2012.
- [106] Y. Kim, J. Zhu, B. Yeom, M. Di Prima, X. Su, J.-G. Kim, S. J. Yoo, C. Uher, and N. A. Kotov, “Stretchable nanoparticle conductors with self-organized conductive pathways,” *Nature*, vol. 500, no. 7460, pp. 59–63, 2013.
- [107] S. Yao and Y. Zhu, “Nanomaterial-enabled stretchable conductors: strategies, materials and devices,” *Advanced Materials*, vol. 27, no. 9, pp. 1480–1511, 2015.
- [108] J. Liang, L. Li, X. Niu, Z. Yu, and Q. Pei, “Elastomeric polymer light-emitting devices and displays,” *Nature Photonics*, vol. 7, no. 10, pp. 817–824, 2013.
- [109] Z. Yu, Q. Zhang, L. Li, Q. Chen, X. Niu, J. Liu, and Q. Pei, “Highly flexible silver nanowire electrodes for shape-memory polymer light-emitting diodes,” *Advanced Materials*, vol. 23, no. 5, pp. 664–668, 2011.
- [110] S. Kang, T. Kim, S. Cho, Y. Lee, A. Choe, B. Walker, S.-J. Ko, J. Y. Kim, and H. Ko, “Capillary printing of highly aligned silver nanowire transparent electrodes for high-performance optoelectronic devices,” *Nano Letters*, vol. 15, no. 12, pp. 7933–7942, 2015.
- [111] S. Yao and Y. Zhu, “Wearable multifunctional sensors using printed stretchable conductors made of silver nanowires,” *Nanoscale*, vol. 6, no. 4, pp. 2345–2352, 2014.
- [112] M. Singh, H. M. Haverinen, P. Dhagat, and G. E. Jabbour, “Inkjet printing process and its applications,” *Advanced materials*, vol. 22, no. 6, pp. 673–685, 2010.
- [113] B.-R. Yang, W. Cao, G.-S. Liu, H.-J. Chen, Y.-Y. Noh, T. Minari, H.-C. Hsiao, C.-Y. Lee, H.-P. D. Shieh, and C. Liu, “Microchannel wetting for controllable patterning and alignment of silver nanowire with high resolution,” *ACS applied materials & interfaces*, vol. 7, no. 38, pp. 21433–21441, 2015.
- [114] J. Liang, L. Li, D. Chen, T. Hajagos, Z. Ren, S.-Y. Chou, W. Hu, and Q. Pei, “Intrinsically stretchable and transparent thin-film transistors based on printable silver nanowires, carbon nanotubes and an elastomeric dielectric,” *Nature communications*, vol. 6, 2015.

- [115] H. Taha, A. Lewis, and C. Sukenik, “Controlled deposition of gold nanowires on semi-conducting and nonconducting surfaces,” *Nano letters*, vol. 7, no. 7, pp. 1883–1887, 2007.
- [116] D. J. Finn, M. Lotya, and J. N. Coleman, “Inkjet printing of silver nanowire networks,” *ACS applied materials & interfaces*, vol. 7, no. 17, pp. 9254–9261, 2015.
- [117] S.-P. Chen, J. R. D. Retamal, D.-H. Lien, J.-H. He, and Y.-C. Liao, “Inkjet-printed transparent nanowire thin film features for uv photodetectors,” *RSC Advances*, vol. 5, no. 87, pp. 70707–70712, 2015.
- [118] H. Lee, B. Seong, J. Kim, Y. Jang, and D. Byun, “Direct alignment and patterning of silver nanowires by electrohydrodynamic jet printing,” *Small*, vol. 10, no. 19, pp. 3918–3922, 2014.
- [119] M. L. Hammock, A. Chortos, B. C.-K. Tee, J. B.-H. Tok, and Z. Bao, “25th anniversary article: the evolution of electronic skin (e-skin): a brief history, design considerations, and recent progress,” *Advanced Materials*, vol. 25, no. 42, pp. 5997–6038, 2013.
- [120] J. C. Yeo, C. T. Lim, *et al.*, “Emerging flexible and wearable physical sensing platforms for healthcare and biomedical applications,” *Microsystems & Nanoengineering*, vol. 2, 2016.
- [121] S. C. Mannsfeld, B. C. Tee, R. M. Stoltenberg, C. V. H. Chen, S. Barman, B. V. Muir, A. N. Sokolov, C. Reese, and Z. Bao, “Highly sensitive flexible pressure sensors with microstructured rubber dielectric layers,” *Nature materials*, vol. 9, no. 10, pp. 859–864, 2010.
- [122] K. A. Erk, K. J. Henderson, and K. R. Shull, “Strain stiffening in synthetic and biopolymer networks,” *Biomacromolecules*, vol. 11, no. 5, pp. 1358–1363, 2010.
- [123] D. Vij, “Series on optics and optoelectronics, handbook of electroluminescent materials,” 2004.
- [124] R. P. Ortiz, A. Facchetti, and T. J. Marks, “High-k organic, inorganic, and hybrid dielectrics for low-voltage organic field-effect transistors,” *Chemical reviews*, vol. 110, no. 1, pp. 205–239, 2009.
- [125] L. Cai, S. Zhang, J. Miao, Z. Yu, and C. Wang, “Fully printed stretchable thin-film transistors and integrated logic circuits,” *ACS nano*, vol. 10, no. 12, pp. 11459–11468, 2016.
- [126] S. G. R. Bade, X. Shan, P. T. Hoang, J. Li, T. Geske, L. Cai, Q. Pei, C. Wang, and Z. Yu, “Stretchable light-emitting diodes with organometal-halide-perovskite-polymer composite emitters,” *Advanced Materials*, vol. 29, no. 23, 2017.
- [127] C. Larson, B. Peele, S. Li, S. Robinson, M. Totaro, L. Beccai, B. Mazzolai, and R. Shepherd, “Highly stretchable electroluminescent skin for optical signaling and tactile sensing,” *Science*, vol. 351, no. 6277, pp. 1071–1074, 2016.

- [128] J. Wang, C. Yan, K. J. Chee, and P. S. Lee, “Highly stretchable and self-deformable alternating current electroluminescent devices,” *Advanced Materials*, vol. 27, no. 18, pp. 2876–2882, 2015.
- [129] C. H. Yang, B. Chen, J. Zhou, Y. M. Chen, and Z. Suo, “Electroluminescence of giant stretchability,” *Advanced Materials*, vol. 28, no. 22, pp. 4480–4484, 2016.
- [130] D.-H. Kim, N. Lu, R. Ma, Y.-S. Kim, R.-H. Kim, S. Wang, J. Wu, S. M. Won, H. Tao, A. Islam, *et al.*, “Epidermal electronics,” *science*, vol. 333, no. 6044, pp. 838–843, 2011.
- [131] S.-K. Kang, R. K. Murphy, S.-W. Hwang, S. M. Lee, D. V. Harburg, N. A. Krueger, J. Shin, P. Gamble, H. Cheng, S. Yu, *et al.*, “Bioresorbable silicon electronic sensors for the brain,” *Nature*, vol. 530, no. 7588, pp. 71–76, 2016.
- [132] T. Yamada, Y. Hayamizu, Y. Yamamoto, Y. Yomogida, A. Izadi-Najafabadi, D. N. Futaba, and K. Hata, “A stretchable carbon nanotube strain sensor for human-motion detection,” *Nature nanotechnology*, vol. 6, no. 5, pp. 296–301, 2011.
- [133] T. Someya, Y. Kato, T. Sekitani, S. Iba, Y. Noguchi, Y. Murase, H. Kawaguchi, and T. Sakurai, “Conformable, flexible, large-area networks of pressure and thermal sensors with organic transistor active matrixes,” *Proceedings of the National Academy of Sciences of the United States of America*, vol. 102, no. 35, pp. 12321–12325, 2005.
- [134] D. J. Lipomi, M. Vosgueritchian, B. C. Tee, S. L. Hellstrom, J. A. Lee, C. H. Fox, and Z. Bao, “Skin-like pressure and strain sensors based on transparent elastic films of carbon nanotubes,” *Nature nanotechnology*, vol. 6, no. 12, pp. 788–792, 2011.
- [135] T. Sekitani, H. Nakajima, H. Maeda, T. Fukushima, T. Aida, K. Hata, and T. Someya, “Stretchable active-matrix organic light-emitting diode display using printable elastic conductors,” *Nature materials*, vol. 8, no. 6, pp. 494–499, 2009.
- [136] J. Liang, L. Li, X. Niu, Z. Yu, and Q. Pei, “Elastomeric polymer light-emitting devices and displays,” *Nature Photonics*, vol. 7, no. 10, pp. 817–824, 2013.
- [137] J. A. Rogers, T. Someya, and Y. Huang, “Materials and mechanics for stretchable electronics,” *Science*, vol. 327, no. 5973, pp. 1603–1607, 2010.
- [138] D.-H. Kim, J. Xiao, J. Song, Y. Huang, and J. A. Rogers, “Stretchable, curvilinear electronics based on inorganic materials,” *Advanced Materials*, vol. 22, no. 19, pp. 2108–2124, 2010.
- [139] R.-H. Kim, D.-H. Kim, J. Xiao, B. H. Kim, S.-I. Park, B. Panilaitis, R. Ghaffari, J. Yao, M. Li, Z. Liu, *et al.*, “Waterproof alingap optoelectronics on stretchable substrates with applications in biomedicine and robotics,” *Nature materials*, vol. 9, no. 11, pp. 929–937, 2010.
- [140] T. Sekitani and T. Someya, “Stretchable, large-area organic electronics,” *Advanced Materials*, vol. 22, no. 20, pp. 2228–2246, 2010.

- [141] S. Yao and Y. Zhu, “Nanomaterial-enabled stretchable conductors: strategies, materials and devices,” *Advanced Materials*, vol. 27, no. 9, pp. 1480–1511, 2015.
- [142] F. Xu and Y. Zhu, “Highly conductive and stretchable silver nanowire conductors,” *Advanced materials*, vol. 24, no. 37, pp. 5117–5122, 2012.
- [143] L. Cai and C. Wang, “Carbon nanotube flexible and stretchable electronics,” *Nanoscale research letters*, vol. 10, no. 1, p. 320, 2015.
- [144] K.-Y. Chun, Y. Oh, J. Rho, J.-H. Ahn, Y.-J. Kim, H. R. Choi, and S. Baik, “Highly conductive, printable and stretchable composite films of carbon nanotubes and silver,” *Nature nanotechnology*, vol. 5, no. 12, pp. 853–857, 2010.
- [145] J. Foroughi, G. M. Spinks, S. Aziz, A. Mirabedini, A. Jeiranikhameneh, G. G. Wallace, M. E. Kozlov, and R. H. Baughman, “Knitted carbon-nanotube-sheath/spandex-core elastomeric yarns for artificial muscles and strain sensing,” *ACS nano*, vol. 10, no. 10, pp. 9129–9135, 2016.
- [146] H. Jang, Y. J. Park, X. Chen, T. Das, M.-S. Kim, and J.-H. Ahn, “Graphene-based flexible and stretchable electronics,” *Advanced Materials*, vol. 28, no. 22, pp. 4184–4202, 2016.
- [147] D. J. Lipomi, J. A. Lee, M. Vosgueritchian, B. C.-K. Tee, J. A. Bolander, and Z. Bao, “Electronic properties of transparent conductive films of pedot: Pss on stretchable substrates,” *Chemistry of Materials*, vol. 24, no. 2, pp. 373–382, 2012.
- [148] M. Shin, J. Y. Oh, K.-E. Byun, Y.-J. Lee, B. Kim, H.-K. Baik, J.-J. Park, and U. Jeong, “Polythiophene nanofibril bundles surface-embedded in elastomer: A route to a highly stretchable active channel layer,” *Advanced Materials*, vol. 27, no. 7, pp. 1255–1261, 2015.
- [149] S. H. Chae, W. J. Yu, J. J. Bae, D. L. Duong, D. Perello, H. Y. Jeong, Q. H. Ta, T. H. Ly, Q. A. Vu, M. Yun, *et al.*, “Transferred wrinkled al₂o₃ for highly stretchable and transparent graphene-carbon nanotube transistors,” *Nature materials*, vol. 12, no. 5, pp. 403–409, 2013.
- [150] S.-K. Lee, B. J. Kim, H. Jang, S. C. Yoon, C. Lee, B. H. Hong, J. A. Rogers, J. H. Cho, and J.-H. Ahn, “Stretchable graphene transistors with printed dielectrics and gate electrodes,” *Nano letters*, vol. 11, no. 11, pp. 4642–4646, 2011.
- [151] J. Liang, L. Li, D. Chen, T. Hajagos, Z. Ren, S.-Y. Chou, W. Hu, and Q. Pei, “Intrinsically stretchable and transparent thin-film transistors based on printable silver nanowires, carbon nanotubes and an elastomeric dielectric,” *Nature communications*, vol. 6, 2015.
- [152] J. Pu, Y. Zhang, Y. Wada, J. Tse-Wei Wang, L.-J. Li, Y. Iwasa, and T. Takenobu, “Fabrication of stretchable mos₂ thin-film transistors using elastic ion-gel gate dielectrics,” *Applied Physics Letters*, vol. 103, no. 2, p. 023505, 2013.

- [153] A. Sekiguchi, F. Tanaka, T. Saito, Y. Kuwahara, S. Sakurai, D. N. Futaba, T. Yamada, and K. Hata, “Robust and soft elastomeric electronics tolerant to our daily lives,” *Nano letters*, vol. 15, no. 9, pp. 5716–5723, 2015.
- [154] F. Xu, M.-Y. Wu, N. S. Safron, S. S. Roy, R. M. Jacobberger, D. J. Bindl, J.-H. Seo, T.-H. Chang, Z. Ma, and M. S. Arnold, “Highly stretchable carbon nanotube transistors with ion gel gate dielectrics,” *Nano letters*, vol. 14, no. 2, pp. 682–686, 2014.
- [155] A. Chortos, G. I. Koleilat, R. Pfattner, D. Kong, P. Lin, R. Nur, T. Lei, H. Wang, N. Liu, Y.-C. Lai, *et al.*, “Mechanically durable and highly stretchable transistors employing carbon nanotube semiconductor and electrodes,” *Advanced Materials*, vol. 28, no. 22, pp. 4441–4448, 2016.
- [156] C. Cao, J. B. Andrews, A. Kumar, and A. D. Franklin, “Improving contact interfaces in fully printed carbon nanotube thin-film transistors,” *ACS nano*, vol. 10, no. 5, pp. 5221–5229, 2016.
- [157] M. Itkis, D. Perea, S. Niyogi, S. Rickard, M. Hamon, H. Hu, B. Zhao, and R. Haddon, “Purity evaluation of as-prepared single-walled carbon nanotube soot by use of solution-phase near-ir spectroscopy,” *Nano Letters*, vol. 3, no. 3, pp. 309–314, 2003.
- [158] D. Bodas and C. Khan-Malek, “Formation of more stable hydrophilic surfaces of pdms by plasma and chemical treatments,” *Microelectronic engineering*, vol. 83, no. 4, pp. 1277–1279, 2006.
- [159] Y. J. Moon, H. Kang, S. H. Lee, K. Kang, Y. J. Cho, J. Y. Hwang, and S. J. Moon, “Effect of contact angle and drop spacing on the bulging frequency of inkjet-printed silver lines on fc-coated glass,” *Journal of Mechanical Science and Technology*, vol. 28, no. 4, pp. 1441–1448, 2014.
- [160] H. Wang, W. Zhou, D. L. Ho, K. I. Winey, J. E. Fischer, C. J. Glinka, and E. K. Hobbie, “Dispersing single-walled carbon nanotubes with surfactants: a small angle neutron scattering study,” *Nano Letters*, vol. 4, no. 9, pp. 1789–1793, 2004.
- [161] L. Cai, L. Song, P. Luan, Q. Zhang, N. Zhang, Q. Gao, D. Zhao, X. Zhang, M. Tu, F. Yang, *et al.*, “Super-stretchable, transparent carbon nanotube-based capacitive strain sensors for human motion detection,” *Scientific reports*, vol. 3, p. 3048, 2013.
- [162] R. P. Ortiz, A. Facchetti, and T. J. Marks, “High-k organic, inorganic, and hybrid dielectrics for low-voltage organic field-effect transistors,” *Chemical reviews*, vol. 110, no. 1, pp. 205–239, 2009.
- [163] S. H. Kim, K. Hong, W. Xie, K. H. Lee, S. Zhang, T. P. Lodge, and C. D. Frisbie, “Electrolyte-gated transistors for organic and printed electronics,” *Advanced Materials*, vol. 25, no. 13, pp. 1822–1846, 2013.
- [164] L. Cai, S. Zhang, J. Miao, Z. Yu, and C. Wang, “Fully printed foldable integrated logic gates with tunable performance using semiconducting carbon nanotubes,” *Advanced Functional Materials*, vol. 25, no. 35, pp. 5698–5705, 2015.

- [165] X. Cao, H. Chen, X. Gu, B. Liu, W. Wang, Y. Cao, F. Wu, and C. Zhou, “Screen printing as a scalable and low-cost approach for rigid and flexible thin-film transistors using separated carbon nanotubes,” *ACS nano*, vol. 8, no. 12, pp. 12769–12776, 2014.
- [166] P. H. Lau, K. Takei, C. Wang, Y. Ju, J. Kim, Z. Yu, T. Takahashi, G. Cho, and A. Javey, “Fully printed, high performance carbon nanotube thin-film transistors on flexible substrates,” *Nano letters*, vol. 13, no. 8, pp. 3864–3869, 2013.
- [167] S. C. Mannsfeld, B. C. Tee, R. M. Stoltenberg, C. V. H. Chen, S. Barman, B. V. Muir, A. N. Sokolov, C. Reese, and Z. Bao, “Highly sensitive flexible pressure sensors with microstructured rubber dielectric layers,” *Nature materials*, vol. 9, no. 10, pp. 859–864, 2010.
- [168] N. Matsuhisa, M. Kaltenbrunner, T. Yokota, H. Jinno, K. Kuribara, T. Sekitani, and T. Someya, “Printable elastic conductors with a high conductivity for electronic textile applications,” *Nature communications*, vol. 6, 2015.
- [169] A. Goncharenko, V. Lozovski, and E. Venger, “Lichtenecker’s equation: applicability and limitations,” *Optics Communications*, vol. 174, no. 1, pp. 19–32, 2000.
- [170] Y. Kim, J. Zhu, B. Yeom, M. Di Prima, X. Su, J.-G. Kim, S. J. Yoo, C. Uher, and N. A. Kotov, “Stretchable nanoparticle conductors with self-organized conductive pathways,” *Nature*, vol. 500, no. 7460, pp. 59–63, 2013.
- [171] G. Shin, C. H. Yoon, M. Y. Bae, Y. C. Kim, S. K. Hong, J. A. Rogers, and J. S. Ha, “Stretchable field-effect-transistor array of suspended SnO_2 nanowires,” *Small*, vol. 7, no. 9, pp. 1181–1185, 2011.
- [172] J.-K. Yuan, S.-H. Yao, Z.-M. Dang, A. Sylvestre, M. Genestoux, and J. Bai, “Giant dielectric permittivity nanocomposites: realizing true potential of pristine carbon nanotubes in polyvinylidene fluoride matrix through an enhanced interfacial interaction,” *The Journal of Physical Chemistry C*, vol. 115, no. 13, pp. 5515–5521, 2011.
- [173] F. Koppens, T. Mueller, P. Avouris, A. Ferrari, M. Vitiello, and M. Polini, “Photodetectors based on graphene, other two-dimensional materials and hybrid systems,” *Nature nanotechnology*, vol. 9, no. 10, pp. 780–793, 2014.
- [174] P. Richards, “Bolometers for infrared and millimeter waves,” *Journal of Applied Physics*, vol. 76, no. 1, pp. 1–24, 1994.
- [175] D. Jariwala, V. K. Sangwan, L. J. Lauhon, T. J. Marks, and M. C. Hersam, “Carbon nanomaterials for electronics, optoelectronics, photovoltaics, and sensing,” *Chemical Society Reviews*, vol. 42, no. 7, pp. 2824–2860, 2013.
- [176] G. Buchs, S. Bagiante, and G. Steele, “Corrigendum: Identifying signatures of photothermal current in a double-gated semiconducting nanotube,” *Nature communications*, vol. 6, p. 5463, 2015.

- [177] C.-X. Sheng, Z. V. Vardeny, A. Dalton, and R. Baughman, “Exciton dynamics in single-walled nanotubes: Transient photoinduced dichroism and polarized emission,” *Physical Review B*, vol. 71, no. 12, p. 125427, 2005.
- [178] F. Wang, G. Dukovic, L. E. Brus, and T. F. Heinz, “Time-resolved fluorescence of carbon nanotubes and its implication for radiative lifetimes,” *Physical review letters*, vol. 92, no. 17, p. 177401, 2004.
- [179] M. E. Itkis, F. Borondics, A. Yu, and R. C. Haddon, “Bolometric infrared photoreponse of suspended single-walled carbon nanotube films,” *Science*, vol. 312, no. 5772, pp. 413–416, 2006.
- [180] J. D. Chudow, D. F. Santavicca, C. B. McKitterick, D. E. Prober, and P. Kim, “Terahertz detection mechanism and contact capacitance of individual metallic single-walled carbon nanotubes,” *Applied Physics Letters*, vol. 100, no. 16, p. 163503, 2012.
- [181] A. Y. Glamazda, V. Karachevtsev, W. B. Euler, I. A. Levitsky, *et al.*, “Achieving high mid-ir bolometric responsivity for anisotropic composite materials from carbon nanotubes and polymers,” *Advanced Functional Materials*, vol. 22, no. 10, pp. 2177–2186, 2012.
- [182] R. Lu, R. Kamal, and J. Z. Wu, “A comparative study of 1/f noise and temperature coefficient of resistance in multiwall and single-wall carbon nanotube bolometers,” *Nanotechnology*, vol. 22, no. 26, p. 265503, 2011.
- [183] R. Lu, Z. Li, G. Xu, and J. Z. Wu, “Suspending single-wall carbon nanotube thin film infrared bolometers on microchannels,” *Applied Physics Letters*, vol. 94, no. 16, p. 163110, 2009.
- [184] R. Lu, J. J. Shi, F. J. Baca, and J. Z. Wu, “High performance multiwall carbon nanotube bolometers,” *Journal of Applied Physics*, vol. 108, no. 8, p. 084305, 2010.
- [185] M. Tarasov, J. Svensson, L. Kuzmin, and E. E. Campbell, “Carbon nanotube bolometers,” *Applied Physics Letters*, vol. 90, no. 16, p. 163503, 2007.
- [186] M. S. Arnold, A. A. Green, J. F. Hulvat, S. I. Stupp, and M. C. Hersam, “Sorting carbon nanotubes by electronic structure using density differentiation,” *Nature nanotechnology*, vol. 1, no. 1, pp. 60–65, 2006.
- [187] F. Chen, B. Wang, Y. Chen, and L.-J. Li, “Toward the extraction of single species of single-walled carbon nanotubes using fluorene-based polymers,” *Nano letters*, vol. 7, no. 10, pp. 3013–3017, 2007.
- [188] H. Liu, D. Nishide, T. Tanaka, and H. Kataura, “Large-scale single-chirality separation of single-wall carbon nanotubes by simple gel chromatography,” *Nature communications*, vol. 2, p. 309, 2011.

- [189] X. Tu, S. Manohar, A. Jagota, and M. Zheng, “Dna sequence motifs for structure-specific recognition and separation of carbon nanotubes,” *Nature*, vol. 460, no. 7252, pp. 250–253, 2009.
- [190] X. Zhang, Z. Yu, C. Wang, D. Zarrouk, J.-W. T. Seo, J. C. Cheng, A. D. Buchan, K. Takei, Y. Zhao, J. W. Ager, *et al.*, “Photoactuators and motors based on carbon nanotubes with selective chirality distributions,” *Nature communications*, vol. 5, 2014.
- [191] T. M. Barnes, J. L. Blackburn, J. van de Lagemaat, T. J. Coutts, and M. J. Heben, “Reversibility, dopant desorption, and tunneling in the temperature-dependent conductivity of type-separated, conductive carbon nanotube networks,” 2008.
- [192] J. L. Blackburn, T. M. Barnes, M. C. Beard, Y.-H. Kim, R. C. Tenent, T. J. McDonald, B. To, T. J. Coutts, and M. J. Heben, “Transparent conductive single-walled carbon nanotube networks with precisely tunable ratios of semiconducting and metallic nanotubes,” *Acs Nano*, vol. 2, no. 6, pp. 1266–1274, 2008.
- [193] C. Wang, J.-C. Chien, K. Takei, T. Takahashi, J. Nah, A. M. Niknejad, and A. Javey, “Extremely bendable, high-performance integrated circuits using semiconducting carbon nanotube networks for digital, analog, and radio-frequency applications,” *Nano letters*, vol. 12, no. 3, pp. 1527–1533, 2012.
- [194] C. Wang, K. Takei, T. Takahashi, and A. Javey, “Carbon nanotube electronics—moving forward,” *Chemical Society Reviews*, vol. 42, no. 7, pp. 2592–2609, 2013.
- [195] P. Ajayan, M. Terrones, A. De la Guardia, V. Huc, N. Grobert, B. Wei, H. Lezec, G. Ramanath, and T. Ebbesen, “Nanotubes in a flash—ignition and reconstruction,” *Science*, vol. 296, no. 5568, pp. 705–705, 2002.
- [196] Z.-P. Yang, L. Ci, J. A. Bur, S.-Y. Lin, and P. M. Ajayan, “Experimental observation of an extremely dark material made by a low-density nanotube array,” *Nano letters*, vol. 8, no. 2, pp. 446–451, 2008.
- [197] C. Wang, J. Zhang, K. Ryu, A. Badmaev, L. G. De Arco, and C. Zhou, “Wafer-scale fabrication of separated carbon nanotube thin-film transistors for display applications,” *Nano Letters*, vol. 9, no. 12, pp. 4285–4291, 2009.
- [198] S. Zhang, L. Cai, T. Wang, R. Shi, J. Miao, L. Wei, Y. Chen, N. Sepúlveda, and C. Wang, “Bolometric-effect-based wavelength-selective photodetectors using sorted single chirality carbon nanotubes,” *Scientific reports*, vol. 5, 2015.
- [199] T. Yamada, Y. Hayamizu, Y. Yamamoto, Y. Yomogida, A. Izadi-Najafabadi, D. N. Futaba, and K. Hata, “A stretchable carbon nanotube strain sensor for human-motion detection,” *Nature nanotechnology*, vol. 6, no. 5, pp. 296–301, 2011.
- [200] J. J. Park, W. J. Hyun, S. C. Mun, Y. T. Park, and O. O. Park, “Highly stretchable and wearable graphene strain sensors with controllable sensitivity for human motion monitoring,” *ACS applied materials & interfaces*, vol. 7, no. 11, pp. 6317–6324, 2015.

- [201] S. Gong, D. T. Lai, Y. Wang, L. W. Yap, K. J. Si, Q. Shi, N. N. Jason, T. Sridhar, H. Uddin, and W. Cheng, "Tattoo-like polyaniline microparticle-doped gold nanowire patches as highly durable wearable sensors," *ACS applied materials & interfaces*, vol. 7, no. 35, pp. 19700–19708, 2015.
- [202] T. Tamura, Y. Maeda, M. Sekine, and M. Yoshida, "Wearable photoplethysmographic sensors past and present," *Electronics*, vol. 3, no. 2, pp. 282–302, 2014.
- [203] A. Challoner, "Photoelectric plethysmography for estimating cutaneous blood flow," *Non-invasive physiological measurements*, vol. 1, pp. 125–151, 1979.
- [204] A. Kamal, J. Harness, G. Irving, and A. Mearns, "Skin photoplethysmography: a review," *Computer methods and programs in biomedicine*, vol. 28, no. 4, pp. 257–269, 1989.
- [205] J. Allen, "Photoplethysmography and its application in clinical physiological measurement," *Physiological measurement*, vol. 28, no. 3, p. R1, 2007.
- [206] L. Y. Chen, B. C.-K. Tee, A. L. Chortos, G. Schwartz, V. Tse, D. J. Lipomi, H.-S. P. Wong, M. V. McConnell, and Z. Bao, "Continuous wireless pressure monitoring and mapping with ultra-small passive sensors for health monitoring and critical care," *Nature communications*, vol. 5, p. 5028, 2014.
- [207] W. W. Nichols, "Clinical measurement of arterial stiffness obtained from noninvasive pressure waveforms," *American journal of hypertension*, vol. 18, no. S1, pp. 3S–10S, 2005.
- [208] C. Wang, D. Hwang, Z. Yu, K. Takei, J. Park, T. Chen, B. Ma, and A. Javey, "User-interactive electronic skin for instantaneous pressure visualization," *Nature materials*, vol. 12, no. 10, pp. 899–904, 2013.